The Pennsylvania State University

The Graduate School

College of Earth and Mineral Sciences

MINERALOGICAL AND TEXTURAL CONTROLS ON SHEAR STRENGTH, SLIP STABILITY AND PERMEABILITY OF FAULTS

A Dissertation in

Energy and Mineral Engineering

by

Chaoyi Wang

Submitted in Partial Fulfillment
of the Requirements
for the Degree of

Doctor of Philosophy

May 2019

The dissertation of Chaoyi Wang was reviewed and approved* by the following:

Derek Elsworth
Professor of Energy and Mineral Engineering and Professor of Geosciences
Dissertation Advisor
Chair of Committee

Chris Marone
Professor of Geosciences

Tong Qiu
Associate Professor of Civil and Environmental Engineering

Shimin Liu
Associate Professor of Energy and Mineral Engineering

Luis F. Ayala
Professor of Petroleum and Natural Gas Engineering
Associated Department Head for Graduate Education

*Signatures are on file in the Graduate School.

ABSTRACT

Induced seismicity resulting from fluid injection into the subsurface related to water and CO_2 disposal, hydraulic fracturing and the stimulation of geothermal reservoirs present an important societal concern. These human activities involve the injection of large volumes of pressurized fluid into the subsurface, potentially at high rates, raising local pore pressures and disturbing the pristine local stress regime by lowering effective normal stress on pre-existing faults and fractures. The reduction of effective normal stress may trigger fault/fracture reactivation and in some cases result in hazardous seismic ruptures. Effective management and engineering of anthropogenic seismic events requires substantial understanding in the mechanisms, especially for the controlling factors on coupled rheological and transport response, including fault shear strength, slip stability, and permeability evolution during such events. In this study, we explore the coupled rheological and transport response of faults and fractures during reactivation as controlled by two fundamental controlling properties, viz., mineralogy and textural features. We approach this problem through shear experiments on analog faults and fractures *via* laboratory and numerical experiments. Specifically, we investigate: (1) the influence of frictionally weak minerals (talc) in mixtures of mineral analogs featuring contrasting frictional properties, (2) the influence of iron oxide grain coatings on quartz aggregates, and (3) the influence of fracture roughness in mated fractures on the ensemble shear strength, slip stability, and permeability evolution during reactivation events. We address the following questions in this study: (1) how much and what distribution of frictionally weak minerals is required to induce significant weakening in faults consisting of a matrix

of frictionally strong minerals, (2) how does a pre-imposed weak mineral layer influence the rheological and transport behavior of faults, (3) what is the influence of a trace amount of grain coating materials introduce on the coupled behavior of faults, and finally (4) how do asperity height and wave length control the ensemble behavior of faults. These questions are explicitly answered in the following.

Chapter 1 explores the impact of phyllosilicate (weak but velocity-strengthening) in a majority tectosilicate (strong but velocity-weakening) matrix in bulk shear strength and slip stability of faults. Numerical simple-shear experiments using a Distinct Element Model (DEM) are conducted on both uniform mixtures of quartz and talc analogs and on textured mixtures consisting of a talc layer embedded in a quartz matrix. The mechanical response of particles is represented by a linear-elastic contact model with a slip weakening constitutive relation representing the essence of rate-state friction. The weight percentage of the talc in the uniform mixtures and the relative thickness of the talc layer in the textured mixtures are varied to investigate the transitional behavior of shear strength and slip stability. Specifically, for uniform mixtures, ~50% reduction on bulk shear strength is observed with 25% talc present, and a dominant influence of talc occurs at 50%; for textured mixtures, a noticeable weakening effect is shown at a relative layer thickness of 1-particle, ~50% shear strength reduction is observed with 3-particles, and a dominant influence occurs at 5-particles. In terms of slip stability, a transition from velocity-weakening to velocity-strengthening is observed with 10% to 25% talc present in the uniform mixtures or with 3-particles to 5-particles in the textured mixtures. In addition, further analysis suggest that quartz has a high tendency towards dilation, potentially

promoting permeability; while talc dilates with increased slip rate, but compacts rapidly when slip rate is reduced, potentially destroying permeability. The simulation results match well with previous laboratory observations.

Chapter 2 elaborates numerical shear reactivation experiments on analog mixtures of quartz and talc gouge using a three-dimensional (3D) distinct element model (DEM). We follow the evolution of shear strength, slip stability, and permeability of the gouge mixture during dynamic shear and explore the mesoscopic mechanisms. A modified slip-weakening constitutive law is applied at contacts. We perform velocity-stepping experiments on both uniform, and layered mixtures of quartz and talc analogs. We separately vary the proportion of talc in the uniform mixtures and talc layer thickness in the layered mixtures. Shear displacements are cycled through shear velocities of 1 and 10μm/s. Simulation results show that talc has a strong weakening effect on shear strength - a thin shear-parallel layer of talc (~8.1 wt%) can induce significant weakening. However, the model offsets laboratory derived strong weakening effects of talc observed in uniform mixtures, implying the governing mechanisms may be the strong shear localization effect of talc, which is enhanced by its natural platy shape. Ensemble stability $(a - b)$ can be enhanced by increasing talc content in uniform talc-quartz mixtures. No apparent influence of increasing talc layer thickness on $(a - b)$ is observed in layered mixtures. Talc enhances compaction at velocity down-steps, potentially reducing fault permeability. Additionally, we show that dimensionality significantly impacts the resolution of dynamic responses. 3D simulations are more representative of laboratory observed behavior. Numerical noise is shown to be of the order of ~0.1 of previous 2D counterparts. Evolution trends of stability

parameters regarding the composition and structure of the fault gouge can be straightforwardly obtained from the 3D simulation. Our study elaborates a DEM approach to mechanistically investigate the mechanical and rheological response of faults during shearing and enhances the understanding of fault weakening mechanism.

Chapter 3 involves investigating the influence of CO_2-transformed iron oxide coatings on the coupled behavior of faults. Fugitive emissions of CO_2 along faults may significantly influence their rheology and permeability by altering cementation and transforming gouge components. We conduct laboratory double direct shear experiments on pristine hematite-, and CO_2-transformed goethite-coated quartz gouge to investigate the evolution of shear strength, slip stability and permeability. The gouge samples are synthesized in the laboratory and are characterized by particle size distribution and through SEM imaging both before and after shear-permeability experiments. Shear strength (at 3 MPa), a-b stability values, frictional healing and creep rates and (fault parallel) permeability are measured in velocity-stepping and slide-hold-slide loading modes. Hematite-coated quartz exhibit the highest peak shear strength, followed by goethite- then un-coated quartz. Coated and un-coated gouge samples exhibit similar residual shear strength. Hematite-coated quartz may undergo potential seismic slip, suggesting by negative (a-b) values. Goethite-coated quartz shows velocity-strengthening behavior by featuring positive (a-b) values but higher frictional healing rate and creep rate. All samples show an initial increase in permeability followed by a decline. However, goethite-coated samples show much less reduction in permeability than others. Characterization suggests that the liberation, transport and clogging of coating particles and shear-produced wear

products can be the main mechanism for permeability evolution. These observations suggest CO_2-transformed goethite-coated quartz-rich faults feature reduced risk of seismic reactivation, while greater loss of inventory in the long-term containment of CO_2 may be expected.

Chapter 4 investigates the influences of roughness on the ensemble mechanical and rheological behavior of mated fractures during reactivation. Subsurface fluid injections can disturb the effective stress regime by elevating pore pressure and potentially reactivate faults and fractures. Laboratory studies indicate that fracture rheology and permeability s in such reactivation events are linked to the roughness of the fracture surfaces. We construct discrete element method (DEM) models to explore the influence of fracture surface roughness on the shear strength, slip stability, and permeability evolution during such slip events. For each simulation, a pair of analog rock coupons (3D bonded quartz-particle analogs) representing a mated fracture are sheared under a velocity-stepping scheme. The roughness of the fracture is defined in terms of asperity height and asperity wavelength. Results show that (1) samples with larger asperity heights (rougher), when sheared, exhibit a higher peak strength which quickly devolves to a residual strength after a threshold shear displacement; (2) these rougher samples also exhibit greater slip stability due to a high degree of asperity wear and resultant production of wear products; (3) long-term suppression of permeability is observed with rougher fractures, which is plausibly due to the removal of asperities and redistribution of wear products, which locally reduces porosity in the dilating fracture. This study provides insights into the understanding of the

mechanisms of frictional and rheological evolution of rough fractures anticipated during reactivation events.

The chapters of this dissertation correspond with four papers either published or in-submittal. These papers are listed below by the order of each chapter:

Wang, C., Elsworth, D., and Fang, Y. (2017). Influence of weakening minerals on ensemble strength and slip stability of faults. *Journal of Geophysical Research: Solid Earth*, 122(9), 7090–7110. https://doi.org/10.1002/2016JB013687

Wang, C., Elsworth, D., and Fang, Y. (2019). Ensemble Shear Strength, Stability, and Permeability of Mixed Mineralogy Fault Gouge Recovered from 3D Granular Models. *Journal of Geophysical Research: Solid Earth*, 124(1), 425-441. https://doi.org/10.1029/2018JB016066

Wang, C., and Elsworth, D. (2018). The Influence of CO2-transformed Iron Oxide Grain Coatings on the Rheological and Transport Behaviors of Faults. *Scientific Reports, submitted*

Wang, C., Elsworth, D., Fang, Y., and Zhang, F. (2018). Influence of Fracture Roughness on Shear Strength, Slip Stability and Permeability: A Micro Mechanistic Analysis by 3D Digital Rock Physics. *Journal of Rock Mechanics and Geotechnical Engineering, Submitted*

TABLE OF CONTENTS

LIST OF FIGURES

LIST OF TABLES

ACKNOWLEDGEMENTS

My deepest gratitude goes to Prof. Derek Elsworth for giving me the invaluable opportunity to work with him as a Ph.D. student. His optimistic personality and his curiosity, thoroughness for scientific research have shaped me to become an independent, challenge-driven person and researcher. This dissertation cannot be accomplished without his guidance and support.

I want to give my sincere gratitude to my Ph.D. committee, Prof. Chris Marone, Prof. Tong Qiu, and Prof. Shimin Liu. Especially for the inspiring discussions with Prof. Chris Marone. Advices and suggestions by Prof. Tong Qiu and Prof. Shimin Liu helped me tremendously in perfecting my Ph.D. research. Last but not the least, I also want to thank Prof. Peter Heaney for his advices and generous allowance for me to use his geochemistry lab during the production of the third chapter of this dissertation.

I could not achieve such progress in academia without the selfless support from my parents - Mr. Wang, Jun and Mrs. Li, Ling, we are always, one strong family together.

Finally, I would like to express my thanks to my colleagues Ziyan Li, Yi Fang, Kyungjae Im, Sheng Zhi, Jiehao Wang, Fengshou Zhang, Athena (Si) Chen, John Leeman, Ben Madara, etc… who have graciously contributed to the completion of my research work. The financial support from US DOE Grant DE-FE0023354 is also gratefully appreciated.

Sincerely,

Chaoyi Wang

Chapter 1

Influence of Weakening Minerals on Ensemble Strength and Slip Stability of Faults

Abstract

We explore the impact of phyllosilicate (weak but velocity-strengthening) in a majority tectosilicate (strong but velocity-weakening) matrix in bulk shear strength and slip stability of faults. Numerical simple-shear experiments using a Distinct Element Model (DEM) are conducted on both uniform mixtures of quartz and talc analogs and on textured mixtures consisting of a talc layer embedded in a quartz matrix. The mechanical response of particles is represented by a linear-elastic contact model with a slip weakening constitutive relation representing the essence of rate-state friction. The weight percentage of the talc in the uniform mixtures and the relative thickness of the talc layer in the textured mixtures are varied to investigate the transitional behavior of shear strength and slip stability. Specifically, for uniform mixtures, ~50% reduction on bulk shear strength is observed with 25% talc present, and a dominant influence of talc occurs at 50%; for textured mixtures, a noticeable weakening effect is shown at a relative layer thickness of 1-particle, ~50% shear strength reduction is observed with 3-particles, and a dominant influence occurs at 5-particles. In terms of slip stability, a transition from velocity-weakening to velocity-strengthening is observed with 10% to 25% talc present in the uniform mixtures or with 3-particles to 5-particles in the textured mixtures. In addition,

further analysis suggest that quartz has a high tendency towards dilation, potentially promoting permeability; while talc dilates with increased slip rate, but compacts rapidly when slip rate is reduced, potentially destroying permeability. The simulation results match well with previous laboratory observations.

1 Introduction

In nature, tectonic faults tend to slip at much lower resolved shear stress than the stresses inferred from rock mechanics experiments [*Engelder et al.*, 1975; *Dieterich*, 1979a; *Marone et al.*, 1990]. Explanations for this difference between laboratory observations and natural phenomena include the prevalence of low effective stresses, elevated pore pressures [*Rice*, 1992; *Faulkner and Rutter*, 2001] and dynamic weakening in which friction decreases above a threshold slip rate [*Melosh*, 1996; *Di Toro et al.*, 2006; *Ampuero and Ben-zion*, 2008]. Recent field observations of the San Andreas fault [*Moore and Rymer*, 2007] and an exhumed low angle normal fault in Italy [*Collettini et al.*, 2009] showed that the weakness of natural faults can be explained by the presence of talc; a frictionally weak mineral. Earlier experiments using synthetic mixtures of salts and muscovite/kaolinite [*Bos and Spiers*, 2002; *Niemeijer and Spiers*, 2006] showed that weakening in shear strength can occur with as little as 10% of frictionally weak minerals. In addition, the shear strength and associated stability of a fault greatly depends on its mineralogical composition [*Ikari et al.*, 2011]. Phyllosilicates like talc generally show low frictional strength but are stable during slip events - to the contrary, tectosilicates usually exhibit high frictional strength but slip unstably. Shear experiments using mixtures of talc

and quartz sand [*Carpenter et al.*, 2009] suggests that in order to adequately weaken the fault, 30%-50% of frictionally weak minerals are needed. However, there is only ~2-3% of talc present in some weak tectosilicate faults suggesting that both the structure and texture of the talc is important.

This strong weakening effect of a frictionally weak mineral in a matrix where the majority of minerals are frictionally strong elicits the question of how much of the frictionally weak mineral is needed and in what structure? Also, importantly, what is the impact of this proportion and structure on the stability regime? Experiments conducted on synthetic gouge consisting of quartz as a frictionally strong phase and a through-going talc layer as a frictionally weak phase [*Niemeijer et al.*, 2010; *Moore and Lockner*, 2011] suggest that the frictional strength of the sample gouge decreases systematically with an increase in thickness of the talc layer. Two critical values are noted for both the onset of weakening and for full weakening of the sample relative to pure talc. In addition to the decrease in frictional strength, the sample gouge also showed a transition from mildly unstable to mostly stable during slip events. Additional observations suggest that the permeability evolution of fractures is likely linked to such mineralogical effects on frictional stability [*Fang et al.*, 2017]. The slip characteristics of mature faults are governed by gouge, comprising granular and clay-sized particles, separating fault planes. Distinct Element Methods [DEM; *Cundall and Strack*, 1979] have been successfully applied to represent the mechanical response of assemblages of circular shaped particles that are characteristic of fault gouges. Numerical models of direct shear experiments on granular materials have been developed using DEM, [*Morgan and Boettcher*, 1999], to investigate

the effect of particle size distribution and the effect of inter-particle friction coefficient on the deformation mechanisms in granular fault zones.

The full seismic cycle during fault slip is well described by rate-state friction laws [*Dieterich*, 1979b; *Ruina*, 1983; *Scholz*, 1998]. Rate-state friction laws have been incorporated into grain-grain contact models in DEM [*Abe et al.*, 2002; *Morgan*, 2004], and show good agreement with experimental observations with the configuration of flat fault surface. However, with synthetic fault gouges, the frictional response is shown to be highly dependent on the gouge structure and on particle rotation [*Morgan*, 1999, 2004]. Also, the full implementation of rate-state constitutive laws at a grain-grain scale is computationally inefficient. Despite available DEM models in simulating shear strength evolution of fault gouge, few DEM models are developed to simulate the strength and stability evolution of fault gouge consisting of two mineral phases, i.e. a frictionally strong phase and a frictionally weak phase. Our model simulates the shear strength and slip stability evolution of fault gouge consisting of uniform and textured mixtures of a frictionally strong phase and a frictionally weak phase. We especially focus on how much frictionally weak mineral is needed to weaken the fault. The results of this study provide a numerical approach which could be potentially beneficial for predicting the transitional behavior in stability and transport properties (especially permeability) of mineral mixtures with drastically different material properties during dynamic shearing. This study implements a DEM model with a slip weakening law at the grain-grain boundary. In addition, sample layer thickness, porosity, and coordination number are monitored during

numerical simulations. These simulations are used to define the transitional behavior in slip stability and poromechanical evolution of transport properties of the gouge.

2 Numerical Method and Materials

The distinct element method iteratively solves Newton's second law of motion for an assembly of particles with a pre-defined constitutive model applied at the grain-grain contacts. Calibration of the contact model is essential in DEM modeling. A model is established to simulate direct shear experiments on synthetic fault gouge comprising a two-phase mixture distributed both uniformly and as a through-going layer.

2.1 Distinct element method and contact model

The current DEM model has been developed using the Particle Flow Code 2D [Itasca Crop.], with the principles of DEM described previously in a large body of literature [*Antonellini and Pollard*, 1995; *Burbidge and Braun*, 2002; *Morgan and McGovern*, 2005; *Abe et al.*, 2011]. DEM models are capable of simulating the mechanical response of granular materials, for example, fault gouge [*Morgan and Boettcher*, 1999; *Guo and Morgan*, 2004; *Abe and Mair*, 2009; *Rathbun et al.*, 2013; *Sun et al.*, 2016]. Such simulations are usually carried out using a two-dimensional (2-D) configuration with circular-shaped disks as particles. This maximizes computational efficiency but neglects the role of angularity and out-of-plane rotations in representing the real physical response of granular materials. In general, compared to a three-dimensional model, a two-

dimensional representation is an adequate simplification which retains the advantage of significantly less computational cost while still obtaining a representative mechanical response.

A linear elastic contact model is implemented as the grain-grain contact model (**Figure 1-1**). Linear components act in normal and shear directions and reproduce linear elastic (no tension) and frictional behavior. All components act on a vanishingly small area, with only force transmitted. The contact force (F_c) is resolved into normal (F_n) and shear (F_s) components:

$$F_c = F_n + F_s \tag{1}$$

The linear and shear components are updated in the absence of slip and with active contact as:

$$F_n = (F_n)_0 + k_n \Delta\delta_n \tag{2}$$

$$F_s = (F_s)_0 + k_s \Delta\delta_s \tag{3}$$

$$F_s^{\mu} = -\mu F_n \tag{4}$$

where k_n and k_s are the stiffness of normal and shear elastic components, $\Delta\delta_n$ and $\Delta\delta_s$ are the relative normal and shear displacement between the contacting grains within one time-step. The calculated shear force is compared to the shear strength of the current contact state (F_s^{μ}) and determines whether slip is initiated.

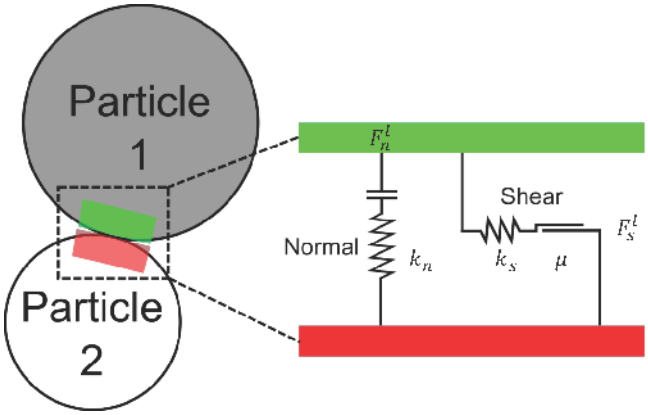

Figure 1-1. The components of linear elastic contact model.

If slip occurs, unlike Coulomb friction with a constant coefficient of friction (μ), a rate-state friction law [*Dieterich*, 1978; *Ruina*, 1983] is utilized to describe the evolution of friction coefficient during the slip event. The original rate-state constitutive relation is described by the empirical state-variable-based friction evolution (equation (5)) with elastic coupling (equation (6)):

$$\mu(V,\theta) = \mu_0 + aln\left(\frac{V}{V_0}\right) + bln\left(\frac{V_0\theta}{D_c}\right) \tag{5}$$

$$\frac{d\mu}{dt} = k\left(V_{lp} - V\right) \tag{6}$$

where a and b are the empirical stability parameters of the material, usually determined by experiments and depend on mineralogy; D_c is the critical slip distance which indicates how much distance the contacting surface slips until reaching the next steady state. The second term on the right-hand-side in equation (5) describes the evolution of friction coefficient upon a stepped velocity change (the direct effect), and the third term describes the evolution of friction coefficient over the critical slip distance D_c (evolution effect). V, V_0, and V_{lp} are the relative current, reference, and load point velocities of the

two contact surfaces respectively; θ is the state variable; k is the geometric stiffness of the loading system. When k is smaller than a critical value, unstable sliding will occur if the system is velocity-weakening, the critical stiffness is governed by confining stress, critical slip distance, and stability parameters a and b. There are two evolution laws for the state variable, Dieterich Law and Ruina Law, which are shown as equations (7) and (8) below respectively:

$$\frac{d\theta}{dt} = 1 - \frac{V\theta}{D_c} \quad (Dieterich\ law) \tag{11}$$

$$\frac{d\theta}{dt} = \frac{V\theta}{D_c} ln\left(\frac{V\theta}{D_c}\right) \quad (Ruina\ law) \tag{12}$$

Experimental observations show that rate-state friction adequately describes both seismic behavior and friction healing of fault slip events [*Marone*, 1998a]. However, the complexity of solving the full nonlinear constitutive relations makes the full implementation in DEM at the grain-grain scale computationally expensive [*Abe et al.*, 2002]. To reduce this computational cost, and assuming the stiffness of the system is much larger than the critical stiffness, the rate-state evolution may be simplified as a form of slip weakening law:

$$\mu_p = \mu_{ref} + aln\left(\frac{V_{lp}}{V_{ref}}\right) \tag{13}$$

$$\mu_{ss} = \mu_{ref} + (a-b)ln\left(\frac{V_{lp}}{V_{ref}}\right) \tag{14}$$

$$\mu = \begin{cases} \mu_p & D_{acc} = 0 \\ \mu_p - \left(\frac{\mu_p - \mu_{ss}}{D_c}\right) D_{acc} & 0 < D_{acc} < D_c \\ \mu_{ss} & D_{acc} \geq D_c \end{cases} \tag{15}$$

Table 1-1. Model parameters including calibrated Young's Modulus for quartz [*Hieher*, 1996] and talc [*Guan*, 2012]

	Quartz Analog	Talc Analog	Unit
Density	2650	2800	kg/m^3
Radius	50-100	20-25	μm
Inter-particle Friction	0.3	0.05	N/A
Effective Modulus	1.30E+10	1.00E+09	N/m^2
Normal-to-shear Stiffness Ratio	1	1.5	N/A
Calibrated Young's Modulus	8.35	0.79	GPa
Inter-particle a Value	0.025	0.025	N/A
Inter-particle b Value	0.050	0.005	N/A
Inter-particle D_c	50	25	μm

where μ_p is the peak friction due to the direct effect of velocity change, μ_{ss} is the steady state friction after frictional evolution has completed, μ_{ref} is the reference friction coefficient depending on different mineral analogs, and D_{acc} is the relative local shear displacement that has accumulated since that previous velocity change on each contact. This value varies through every contact in the model depending on local contact state. V_{lp} and V_{ref} are the absolute values of the current and previous shear velocity of the shear platens respectively. D_c is the characteristic slip distance - a mineral related property that is assigned to each and every local contact.

Figure 1-2 shows the implementation of this slip weakening model. The contact model is implemented onto each contact of the assembly. V_{lp} and V_{ref} are stored for each contact, thus each contact "knows" the current global shear velocity as well as the velocity history of the previous velocity step. D_{acc} is the accumulated relative local shear

displacement. D_{acc} remains zero if no local slip has occurred (shown in **Figure 1-2** as the green path) - as a result, the friction coefficient will remain at a value of μ_{ss}. If (i) a slip event occurs at a contact, and (ii) there is a difference between stored V_{lp} and V_{ref}, the contact will slip weaken (following the red path in **Figure 1-2**, as described by equation (9) to (11)). If the local slip distance threshold D_c is reached, the contact friction will remain as μ_{ss} (orange path) as long as the contact is still active. If slip terminates in the middle of the evolution path (but the contact is still active) then the friction coefficient on the contact will remain as-is (illustrated by the blue dot on the red path in **Figure 1-2**) until slip reinitiates. At re-initiation, the contact friction continues to follow the red evolutionary path. There are cases when active contacts undergoing slip weakening evolution turn inactive due to particle rearrangement. In these cases, the slip weakening evolution will cease once the contact becomes inactive. Newly formed contacts will begin evolving from the end of the green path (**Figure 1-2**) once condition (i) and (ii) above are both met for the contact. Otherwise, the friction coefficient will remain constant as μ_{ref}. If a contact transits a full evolution path (D_c), the friction coefficient will remain as μ_{ss} no matter the slip state and as long as the contact is still active. The contact will not evolve again until the next global velocity step. In particular, once a new contact is formed, the accumulated relative local shear displacement (D_{acc}) is reset to zero so that the slip history of the contact, either slipping or non-slipping, is re-initialized to enable renewed evolution.

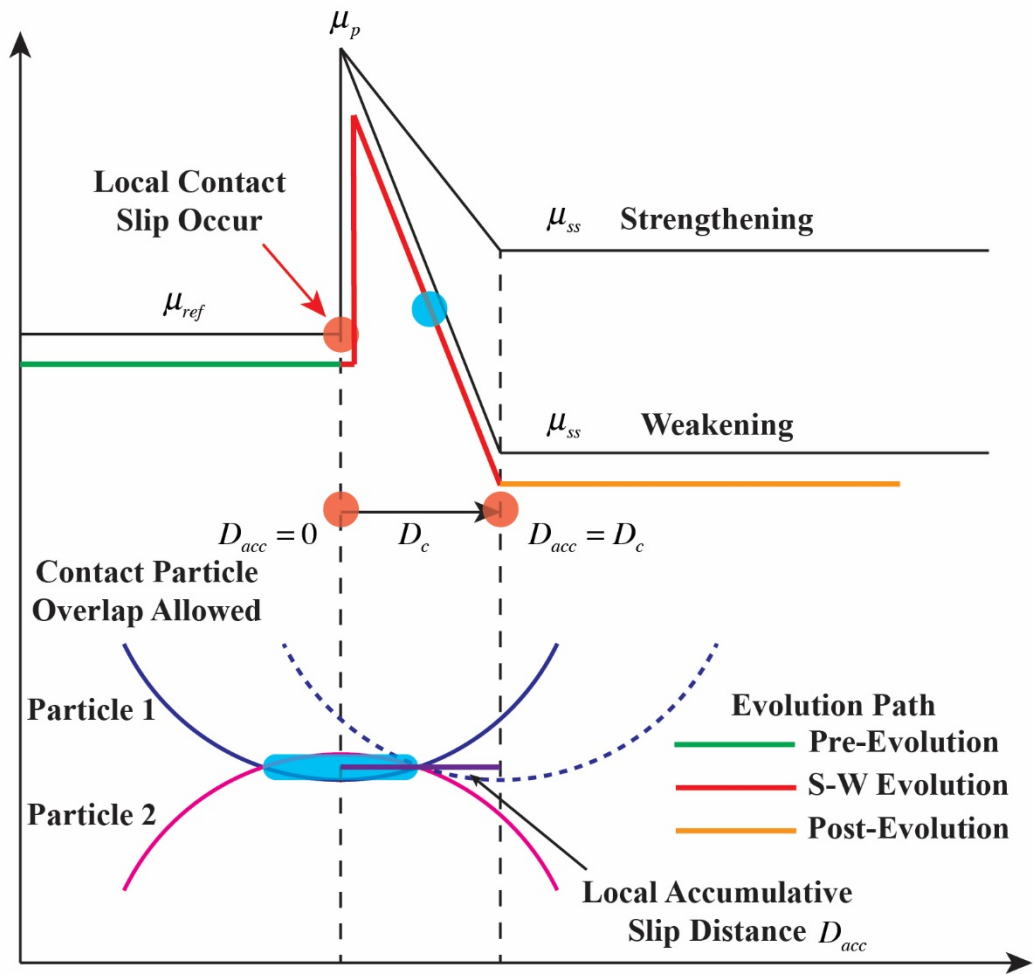

Figure 1-2. Schematic of the slip weakening law: the friction coefficient of a local contact starts to evolve upon a slip event together with a difference between global load point velocity and stored global reference velocity friction will reach a peak (μ_p) and continue to evolve to its steady state (μ_{ss}) if local slip persists according to either velocity-strengthening or velocity-weakening; if slip halted before reaching steady state, the friction coefficient will state as-is; friction evolution of newly formed contact will be reset and evolve from the beginning (left to right).

2.2 Mineral analogs

Observations in nature suggest that the presence of talc may greatly reduce the shear strength of mostly tectosilicate faults and may be a cause of fault creep [*Moore and Rymer*,

2007]. Measurements of the shear strength and stability of granular quartz reveal that quartz is a typical tectosilicate which exhibits high frictional strength and velocity-weakening properties. Conversely, talc is usually frictionally weak but velocity-strengthening [*Ikari et al.*, 2011; *Moore and Lockner*, 2011]. Because quartz and talc have these key contrasting frictional and stability properties, they represent the most suitable candidate analogs for this study. The density, particle size, and rate-state parameters used in this study for quartz and talc analogs are listed in **Table 1-1**.

The elastic modulus of granular materials is dependent on mean stress and is usually much smaller than that of the intact crystals [*Hieher*, 1996; *Guan et al.*, 2012]. In DEM modeling, the elastic behavior of the granular assembly is represented by effective modulus and normal-to-shear stiffness ratio. The effective modulus and normal to shear stiffness ratio are assigned at each contact, and the relationship between them and contact stiffness is listed below (equation (12) and (13)) as,

$$k_n = \frac{AE^*}{L} \tag{12}$$

$$k_s = \frac{k_n}{\kappa^*} \tag{13}$$

where k_n is the normal contact stiffness, k_s is the shear stiffness, A is the virtual contact area of the two entities, typically the product of the smaller diameter of the two contacting entities and unit thickness and κ^* is the normal to shear stiffness ratio.

Notably, the effective modulus is not a macroscopic elastic modulus but is related to it, and the normal-to-shear stiffness ratio is related to Poisson's ratio. Specifically, the normal-to-shear stiffness ratio is defined as the ratio of the normal stiffness (k_n) and shear stiffness (k_s) of the elastic components shown in **Figure 1-1**. These are contact parameters

that are assigned directly to the contacts. They are derived by performing numerical biaxial compression experiments on packs of quartz and talc analogs, respectively. In the trial-and-error calibration procedure, initial estimates of effective modulus and normal to shear stiffness ratio are made as trial parameters. Then a face-centered-cubic assembly of pure mineral analog is generated with the trial parameters. The loose assembly is compacted, equilibrated, then a biaxial compression test is conducted under a normal stress of 10 MPa. The macroscopic elastic modulus of the cubic sample is then calculated by the slope of the axial stress-strain evolution curve (loading direction) at 0.05% of the axial strain. This macroscopic elastic modulus is then compared with laboratory measured macroscopic elastic modulus in the literature. We generally accept values of calibrated modulus which lie within 3% of the suggested values of laboratory experiments [*Hieher*, 1996; *Guan et al.*, 2012], otherwise we adjust the initial estimates and repeat the calibration process. The estimates of effective modulus, normal-to-shear ratio, and resultant modulus used in this study are shown in **Table 1-1**. In addition, the effective modulus of the wall element-particle contact is set to the same magnitude as the quartz-quartz contact analog to minimize stress concentrations effects.

In the case where a talc and quartz analog particle are in contact, the stiffness and rate-and-state parameters (a and b) of this contact is expressed by the geometric average from both contacting entities. The friction coefficient (μ) and characteristic slip distance (D_c) is determined by the smaller value of either entity.

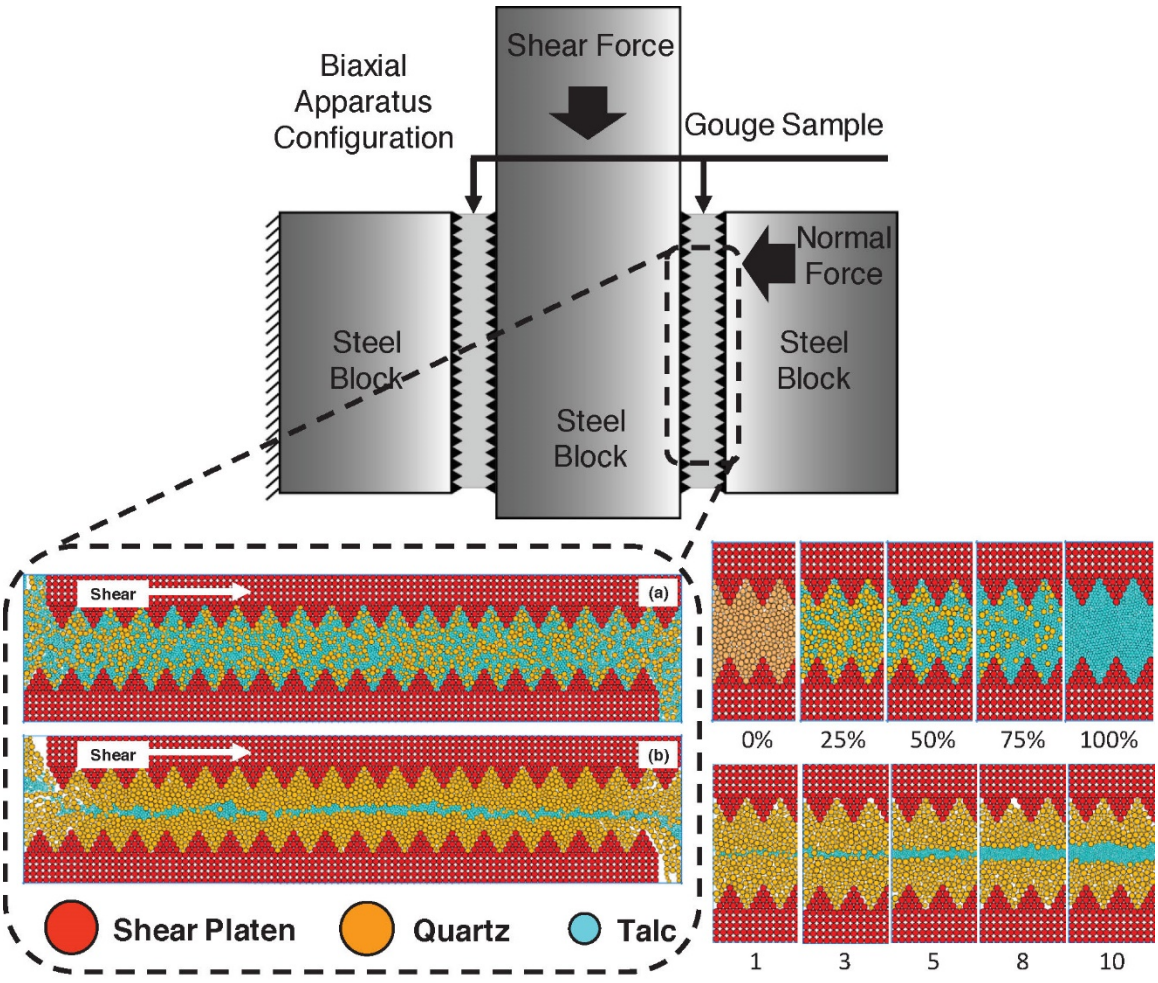

Figure 1-3. DEM model configuration as a symmetric simplification of a double direct shear apparatus: (a) uniform mixtures; (b) textured (layered) mixtures; inset on the right-hand-side shows the variation of quartz (orange) to talc (blue) content/relative layer thickness in uniform/layered mixtures.

3 Experiment Design

The model configuration is in double direct shear configuration [*Mair and Marone*, 1999], which consists of a pair of saw-tooth shaped platens and a synthetic fault gouge sample sandwiched between them (**Figure 1-3**). Unlike the full experimental setup, the numerical model represents one symmetric limb of the apparatus with the modeled platens

retained parallel. Before the shear experiment, the model is 20 mm in length (horizontal), and approximately 5 mm in height (vertical). The shear platens in the numerical model consist of arrays of tightly bounded particle clusters (clumps) with a triangular tip. Wall elements are specified outside the platens to serve as boundaries. These wall elements are facets which do not obey Newton's second law of motion due to lack of mass, however, a servo mechanism constantly adjusts the velocity of the wall elements to maintain static normal stress. Specifically, total unbalanced normal force on a specific wall is monitored by superposing contact normal forces of contacting particles. The velocity vector of the wall element is then adjusted by a scaled value of the difference between total unbalanced stress and target normal stress. A constant confining/normal stress of 10 MPa is applied in all numerical runs. The velocities of the top and bottom wall boundaries are adjusted simultaneously and consistently during shear experiments in order to maintain the normal stress during the shear experiment. A typical numerical shear experiment is conducted as follows: (1) generate shear platens and adjacent wall elements; (2) generate loosely distributed analog particles between two shear platens; (3) apply controlled normal velocity (vertical) on wall elements to drive both shear platens to compact loose particles until reaching the desired confining stress. The velocity applied to wall elements is adjusted to maintain the desired confining stress until average ratio is sufficiently low (0.001). The average ratio is defined as the average of the ratio of unbalanced forces to the sum of body force, applied force, and contact forces on one particle in all degrees of freedom. This quantity is used to identify whether the system is close to equilibrium. The average ratio of 0.001 is typically used in this study to judge whether the system is sufficiently close to

equilibrium; (4) actuate the upper shear plate with a prescribed velocity scheme while holding the lower platen static in order to exert internal shear of the gouge particles; (5) record experimental parameters until shear displacement reaches the desired shear displacement or completion of desired velocity steps.

Table 1-2. Model parameters of numerical experiments; quartz/talc content is varied from 0% to 100% in uniform mixtures; relative talc layer thickness is varied from 1-particle to 10-particles in layered mixtures; initial sample thickness and shear velocity regime during the tests are listed.

Name	Quartz Analog (wt%)	Talc Analog (wt%)	Talc Layer Thickness[a]	Sample Thickness[b] (μm)	Shear Velocity (μm/s)
cqt100-00	100%	0%	N/A	5283.78	1
cqt90-10	90%	10%	N/A	5205.57	1
cqt80-20	80%	20%	N/A	5163.03	1
cqt75-25	75%	25%	N/A	5133.04	1
cqt60-40	60%	40%	N/A	5117.93	1
cqt50-50	50%	50%	N/A	5107.28	1
cqt25-75	25%	75%	N/A	5123.29	1
cqt00-100	0%	100%	N/A	5146.91	1
sqt100-00	100%	0%	N/A	5175.16	1/10/1/10/1
sqt90-10	90%	10%	N/A	5109.28	1/10/1/10/1
sqt80-20	80%	20%	N/A	5051.87	1/10/1/10/1
sqt75-25	75%	25%	N/A	5041.20	1/10/1/10/1
sqt50-50	50%	50%	N/A	5006.85	1/10/1/10/1
sqt25-75	25%	75%	N/A	5021.85	1/10/1/10/1
sqt00-100	0%	100%	N/A	5045.55	1/10/1/10/1
cqt001	98%	2%	1	5168.64	1
cqt003	97%	3%	3	5163.03	1
cqt005	94%	4%	5	5139.05	1
cqt008	90%	10%	8	5152.66	1
cqt010	87%	13%	10	5144.23	1
sqt001	98%	2%	1	5168.64	1/10/1/10/1
sqt003	97%	3%	3	5163.03	1/10/1/10/1
sqt005	94%	4%	5	5139.05	1/10/1/10/1
sqt008	90%	10%	8	5152.66	1/10/1/10/1
sqt010	87%	13%	10	5144.23	1/10/1/10/1

[a] The relative thickness of talc analog layer is determined by the most approximate number of particles vertically aligned in the actual talc analog layer.

[b] The sample thickness is measured at the beginning of each numerical run.

4 Results

Numerical simulations of biaxial direct shear experiments are conducted for mineral mixtures of quartz and talc. Two mixture patterns are considered - uniform and layered. Shear strength evolution and the transition of stability parameters are shown in the results with a variation of mineral compositions and mixture patterns.

4.1 Frictional evolution of mineral mixtures

Constant velocity shear experiments are conducted on uniform mixtures with a shear velocity of 1 μm/s. The evolution of shear strength of uniform mixtures is shown in **Figure 1-4** (a). It is apparent that the bulk shear strength (friction coefficient) decreases as the weight percentage of talc in the mixture increases. To be specific, the residual friction coefficient remains at ~0.70 with no talc in the mixture, while it reduces from ~0.70 to ~0.35 with ~25% talc, showing a strong weakening effect of talc on bulk shear strength of the sample. However, the fast reduction in shear strength slows down when there is more than 25% talc present in the mixture (i.e. 30%, 40%, etc.), when the weight percentage of talc analog exceeds 75%, the residual coefficient of friction exhibits a similar magnitude to pure talc, showing a talc dominating effect. This transition in steady-state friction is

plotted in **Figure 1-4** (b). This trend is revealed in previous experimental observations [*Carpenter et al.*, 2009; *Moore and Lockner*, 2011].

Similarly, constant-velocity shear experiments with the same velocity scheme are conducted on textured (layered) mixtures. Specifically, the sample consists of a quartz matrix and a sandwiched layer of talc. The relative thickness of the talc analog layer is varied in each numerical run to investigate its effect on shear strength of the mixture. The evolution of friction is shown in **Figure 1-4** (c). **Figure 1-4** (d) clearly shows that the steady-state friction coefficient decreases as the relative thickness of the talc analog layer increases. In particular, the steady-state friction coefficient drops from ~0.70 to ~0.35 with layer thickness of the talc increasing from 0-particle to 3-particles. With a relative layer thickness of 5-particles, the residual friction coefficient is reduced to ~0.25, which is approximately the steady-state friction of pure talc (~0.20). With a relative layer thickness larger than 5-particles, the residual friction coefficient drops incrementally and approaches the steady-state friction for pure talc. These observations suggest that a relative thickness of 5-particles is sufficient for the talc analog to establish a dominant effect. Similar effects are also observed with relative thicknesses of 8-particles and 10-particles. This trend is consistent with previous experimental observations [*Niemeijer et al.*, 2010].

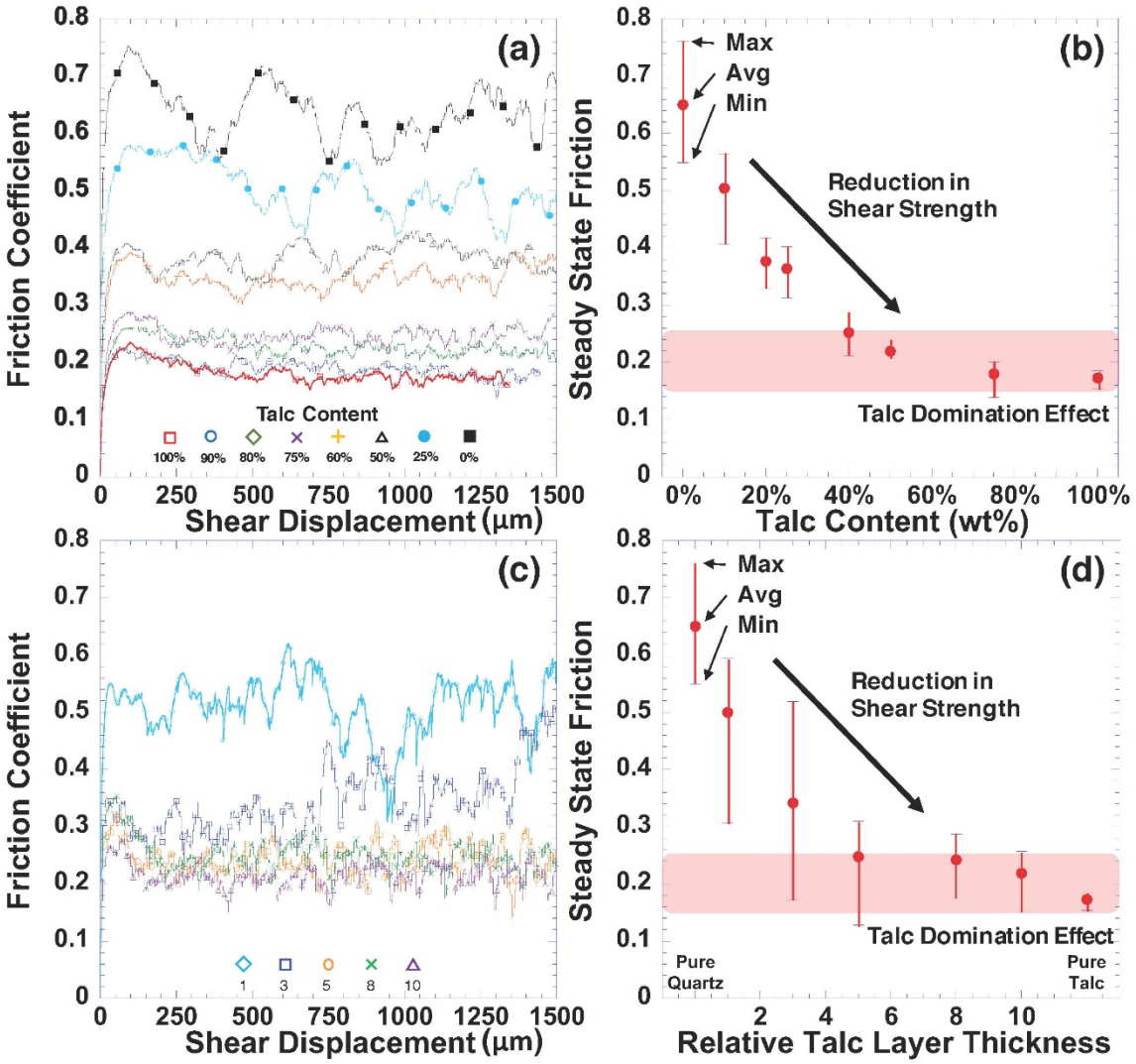

Figure 1-4. (a) Friction evolution of uniform mixtures, (note: symbols in the figure represent keys); (b) residual friction decreases as the talc content increases, with a noticeable weakening at ~25% and a dominant weakening at ~40%; (c) friction evolution of textured mixtures; (d) residual friction decreases as the thickness of the talc layer increases, with a noticeable weakening at 3-particles and a dominant weakening at 5-particles. (note: the maximum, average and minimum values shown in the error bar are calculated from each friction evolution data set after shear displacement of 750 microns).

4.2 Slip stability evolution of mineral mixtures

Observations from the constant-velocity numerical experiments suggest that talc has a significant weakening effect on the shear strength of a quartz-rich fault. In addition, it is suggested from experiments [*Moore and Lockner*, 2011] that talc also influences slip stability of faults consisting of a small amount of talc in a frictionally strong matrix, *i.e.* slip stability can transit from velocity-weakening (quartz-dominant) to velocity-strengthening (talc-dominant) with increasing talc content.

Virtual velocity-stepping experiments, with shear-velocity steps of 1 μm/s and 10 μm/s, were performed on both uniform and layered mixtures of talc and quartz analogs. Specifically, weight percentage of talc in uniform mixtures and relative layer thickness of talc are varied to explore the transition from velocity-weakening to velocity-strengthening. **Figure 1-5** (a) shows the friction evolution of two end-member uniform mixtures of pure quartz and pure talc as an example. The $(a-b)$ values are analyzed by zooming into each of the velocity steps, and the velocity steps are fitted to rate-state friction constitutive relations. We fit the rate-and-state parameters using a forward Levenberg-Marquardt algorithm [*Press et al.*, 1987]. We make an initial estimate of the a, b,and D_c values and progressively fit to rate-and-state constitutive relations (5) through (8). The constitutive relation is solved with shear displacement using a 4th order Runge-Kutta algorithm [*Press et al.*, 1987]. The Levenberg-Marquardt algorithm searches in the range from 1/10 of the initial estimate to 10 times the initial estimate. We conclude when either the difference of parameter or the Chi-square value of the data from current estimate and last estimate meet

the tolerances of 0.0001 or 0.01, respectively. The insets in **Figure 1-5** (a) show the stability analysis of two velocity steps, for example.

In terms of the transition of slip stability parameters, i.e. $(a-b)$values , **Figure 1-5** (b) shows the $(a-b)$ values obtained by previous laboratory shear experiments on mixtures of quartz and talc [*Moore and Lockner*, 2011]. The transition is clearly observable at ~20% talc. In our simulation, the transition in stability parameter of uniform mixtures is shown in **Figure 1-5** (c), the $(a-b)$ values are negative (velocity-weakening) when no talc is introduced; however, the $(a-b)$ values transit to positive rapidly when there is ~10% to ~25% talc present in the mixture. With more than 25% talc analog introduced, the $(a-b)$ values of the bulk sample remain positive, indicating the dominating effect of talc (velocity-strengthening) on bulk slip stability of the mixture.

Transition in slip stability is also expected in layered mixtures of quartz and talc. Results from velocity-stepping experiments on uniform mixtures show a similar trend of increasing $(a-b)$ values when increasing the relative talc layer thickness. With a through-going talc layer, the $(a-b)$ values of the gouge transit to positive with a trace amount of talc (1 ~ 3-particle, **Figure 1-5** (d)). The sample exhibits velocity-strengthening similar to the pure talc with relative talc layer thickness of 5-particles. Additionally, the $(a-b)$ values become larger compared to those for uniform mixtures when the relative thickness of the talc layer is increased. This behavior indicates that the spatial distribution of talc in the gouge has significant influences on the slip stability of the mixture. With a layered structure, even a minimal amount of talc can alter the bulk stability behavior of the fault.

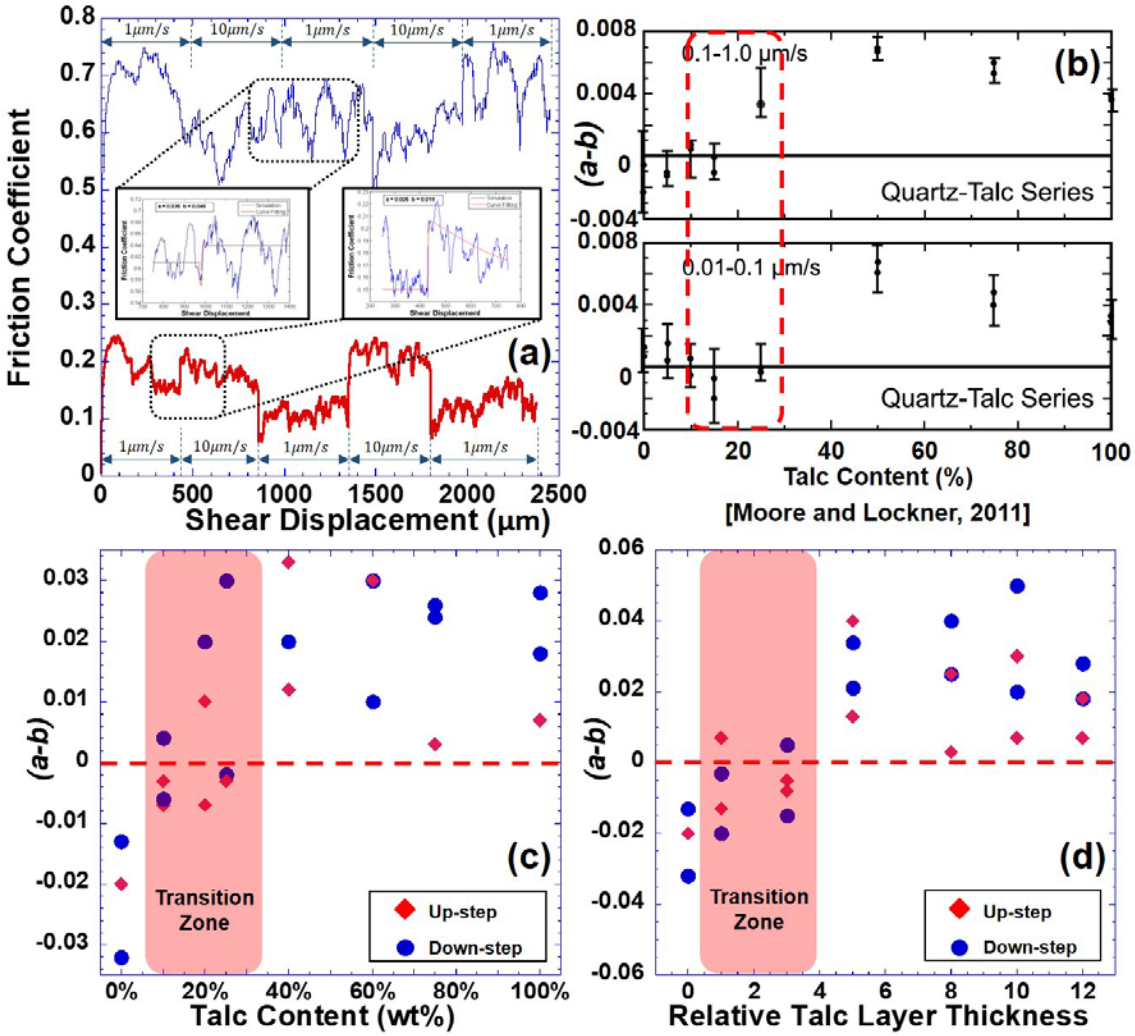

Figure 1-5. Slip stability evolution of uniform mixtures: (a) end-member friction evolution with velocity-stepping shear tests (inset shows an example of curve fitting to recover stability parameters); (b) laboratory data [Moore and Lockner, 2011] of $(a-b)$ obtained using quartz and talc mixtures. The red dashed rectangular is the transition zone from velocity weakening to velocity strengthening; (c) evolution of stability parameter$(a-b)$, $(a-b)$values are negative with no talc present but shifts to positive after more than 10% of talc is introduced, and will keep being positive when more than 25% talc is introduced; (d) evolution of stability $(a-b)$, $(a-b)$values are negative with no talc present but shift to positive after introducing a thin layer (1-particle and 3-particles) of talc, and will remain positive when relative talc layer thickness is larger than 5-particles; Upper right insets: examples showing $(a-b)$ analysis.

4.3 Dilation, coordination number, and permeability

Slip events are usually accompanied by fault dilation or compaction depending on the mineralogical composition and corresponding mechanical properties. The distinctive difference between dilation and compaction defines a possible link between the mineralogy and the permeability evolution of the fault. In other words, dilation indicates potential increase in fault permeability and vice versa. Usually dilation or compaction can be directly measured in laboratory experiments through monitoring the evolution of sample layer thickness. However, it is difficult to directly observe the evolution of porosity and average coordination number in laboratory experiments. Coordination number is the average number of contacts around a particle. The evolution of porosity and coordination number give a clearer picture of dilation or compaction at grain-grain scale. Specifically, when the bulk gouge is compacted, the coordination number is expected to increase while porosity decreases, and conversely for dilation.

Figures 1-6 (a) (b) (c) show the evolution of sample layer thickness, average coordination number, and porosity evolution for pure quartz and pure talc during velocity-stepping experiments, respectively. Overall layer thickness decrease is observed during our numerical tests, which causes a reduction in shear zone thickness. This decrease in sample layer thickness over shear displacement is induced by mineral analog particles filling the two empty pockets at the ends of the upper and lower shear platens during dynamic shearing. This effect occurs in every numerical test; therefore, we consider it as a background compaction effect that will not significantly affect the comparison of dilation effects between numerical tests. Distinct differences are noted for end-member behaviors.

Quartz and talc samples begin with similar initial layer thicknesses (**Figure 1-6** (a)), despite background compaction effects, quartz shows an increase in layer thickness and a sharp decrease in coordination number during the first ~500 microns in shear displacement. Conversely, talc samples show the opposite trend in layer thickness evolution. In addition, the evolution of the coordination number at a velocity up-step, as highlighted for talc in **Figure 1-6** (b), shows a slow decease (i.e. from 1 μm/s to 10 μm/s) but a sharp increase with a velocity down-step (i.e. from 10 μm/s to 1 μm/s). This indicates a slow decrease in number of contacts (dilation) during velocity up-steps but a fast increase in the number of contacts (compaction) upon velocity down-steps. The same behavior is not clearly observed for quartz or for other quartz-rich samples. This is further discussed in discussion section 5.5.

Moreover, we can directly monitor the porosity in the assembly by calculating the ratio of void volume and total volume. An increase in porosity is observed **Figure 1-6** (c) for quartz samples throughout the loading, while relatively steady porosity evolution is observed for the talc sample. The quartz sample evolves to a higher layer thickness, porosity, and lower coordination number than the talc sample, indicating a stronger dilation effect. Evolutions of these three parameters for uniform mixtures and textured mixtures lie between the two end-member evolution responses.

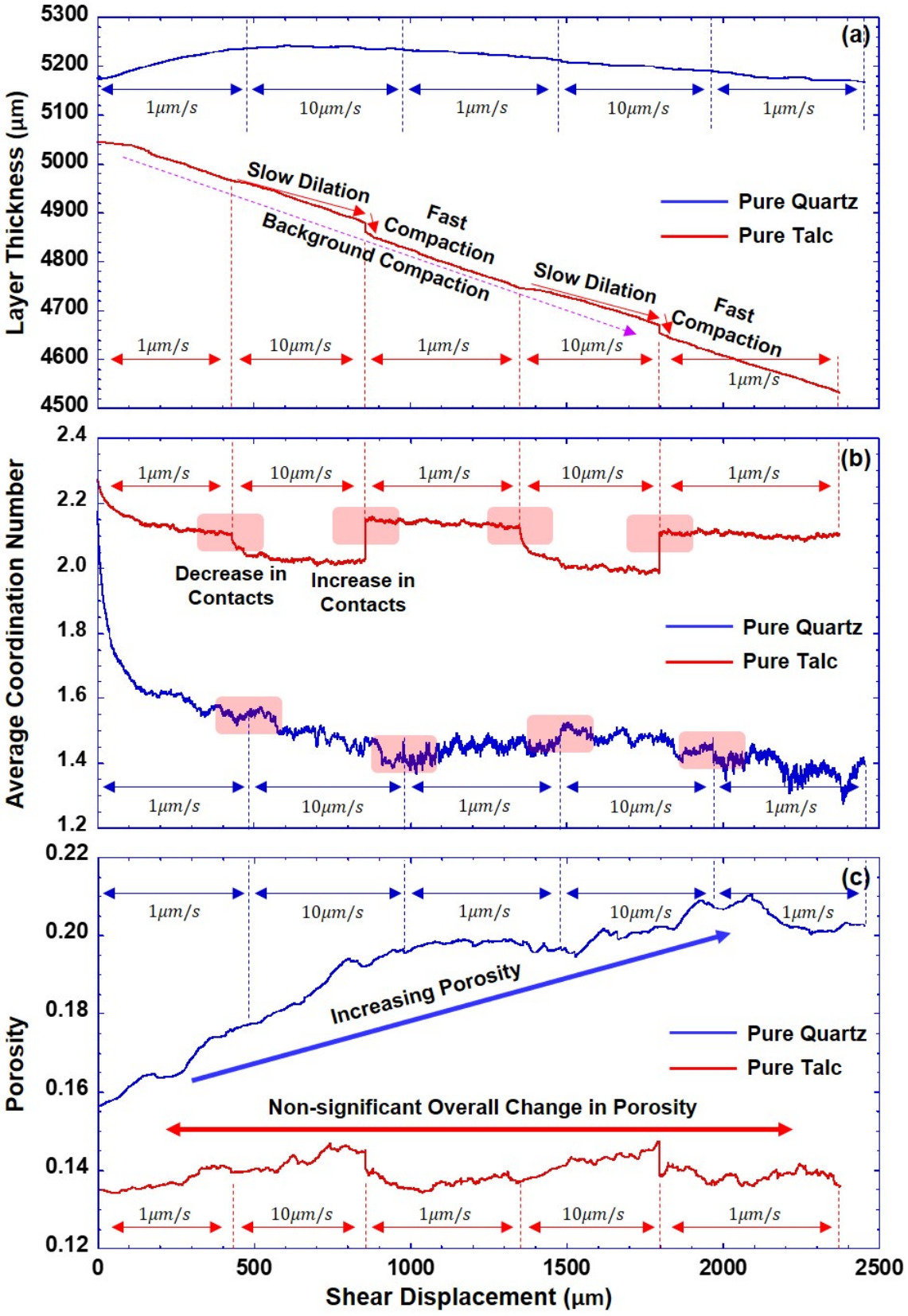
(a)
Layer Thickness (μm)
5300
5200
5100
5000
4900
4800
4700
4600
4500
1μm/s
10μm/s
1μm/s
10μm/s
1μm/s
Slow Dilation
Fast Compaction
Background Compaction
Slow Dilation
Fast Compaction
Pure Quartz
Pure Talc
(b)
Average Coordination Number
2.4
2.2
2.0
1.8
1.6
1.4
1.2
Decrease in Contacts
Increase in Contacts
Pure Quartz
Pure Talc
(c)
Porosity
0.22
0.20
0.18
0.16
0.14
0.12
Increasing Porosity
Non-significant Overall Change in Porosity
Pure Quartz
Pure Talc
0
500
1000
1500
2000
2500
Shear Displacement (μm)

Figure 1-6. (a) Evolution in layer thickness of a pure quartz/talc sample during velocity stepping experiments., quartz shows strong dilation despite background compaction while talc shows slow dilation upon velocity up-steps and fast compaction upon velocity down-steps; (b) Evolution of average coordination number of the same tests, Talc shows a gradual decrease in coordination number at velocity up-steps, but a rapid increase in coordination number at velocity down-steps; quartz shows a negligible change in coordination number at velocity steps; (c) Sample porosity evolution of the same tests, Quartz shows overall increasing porosity while talc shows relatively insignificant porosity change throughout the test.

Estimates of permeability evolution are shown in **Figure 1-7** using equation (14) and (15) [*Ouyang and Elsworth*, 1993; *Samuelson et al.*, 2011]:

$$\frac{k}{k_0} \cong \left(1 + \frac{\Delta H}{H}\right)^3 \tag{14}$$

$$\frac{\Delta H}{H} \cong \Delta\phi \tag{15}$$

Where k/k_0 is the relative ratio in permeability, $\Delta H/H$ is the relative ratio in sample thickness, $\Delta\phi$ is the relative difference in porosity. **Figure 1-7** shows that the permeability of pure quartz increases regardless of the change in velocity, while the permeability of the pure talc sample remains stable with a slight increase during velocity up-steps and a sharp decrease during velocity down-steps. While a compaction effect is generally expected during velocity down-steps, the observations can be plausibly explained by the tight packing of the quartz sample in our specific runs, thus only dilation is observed. Furthermore, the strong tendency of the dilation of quartz can also be explained by a higher elastic modulus and higher particle interlocking caused by higher friction resistance at contacts.

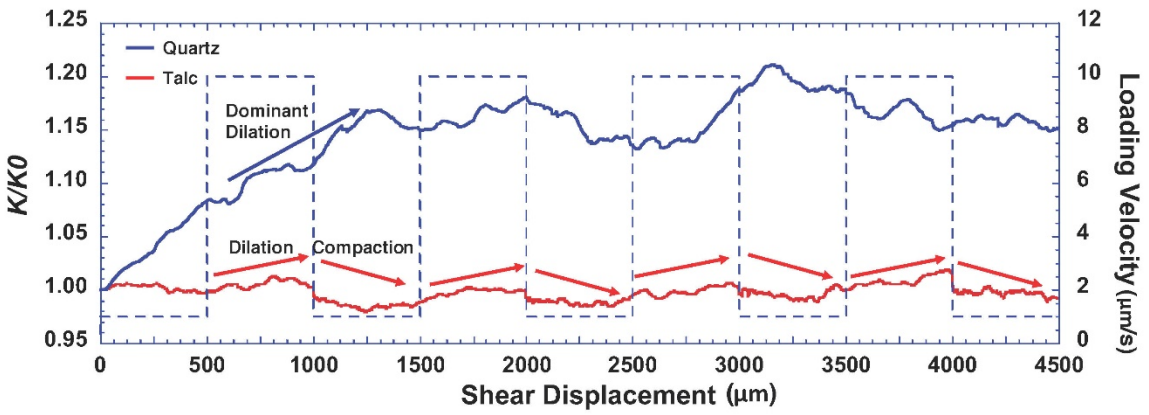

Figure 1-7. Permeability evolution of gouge consisting of pure quartz or talc: gouge consisting of quartz is dilation-dominated while gouge consisting of talc exhibits dilation only on velocity up-steps, but rapid compaction on velocity down-steps.

4.4 Effect of normal stress, characteristic slip distance, and particle size

We test the model with variations in normal stress, critical slip distance and particle size to analyze the sensitivity of the DEM model. We examine behavior at normal stresses of 5, 10,15, 30, and 50 MPa. The frictional evolution curves for 75% quartz and 25% talc mixtures under these different normal stresses are shown in **Figure 1-8** (a). From the initial frictional evolution, we observe a trend indicating that it takes less shear displacement for the assembly to reach steady state friction at lower normal stress - this may be attributed to less normal constraints on particles to rearrange under shearing. The remainder of the evolution curve shows bulk shear strengths to be generally higher during velocity up-steps at low normal stress (5 MPa) - this is likely due to the stronger tendency for dilation at low

normal stresses. Despite these observations, the friction evolution curves generally overlie each other and feature no general trend in shear strength and stability parameters.

In terms of characteristic slip distance (D_c), **Figure 1-8** (b) shows the frictional evolution curves for a 75% quartz and 25% talc mixture under a normal stress of 10 MPa with 2×, 1×, and 0.5× values of D_c (refer to **Table 1-1**). Again, the frictional evolution curves overlie each other. We observe no significant difference in the frictional evolution due to the change in D_c. This is possibly caused by the contact mechanism described in Section 5.5. In the case of smaller D_c, the assembly requires a shorter slip distance to reach steady state, which is subtly observed from the first and the second velocity down-steps. However, the significant amplitude of noise masks this.

The effect of particle size on the evolution of friction is shown in **Figure 1-8** (c), for 2×, 1×, and 0.5× particle radius (refer to **Table 1-1**) under a normal stress of 10 MPa. For smaller particle sizes, the amplitude of the fluctuation is reduced. The evolution curve is not generally offset by reducing the particle diameter except in the initial velocity-step, where for 0.5× particle radius the friction coefficient is smallest. This is potentially due to the increase in surface area of the talc particles when the number of particles increases. However, this initial offset is soon annulled.

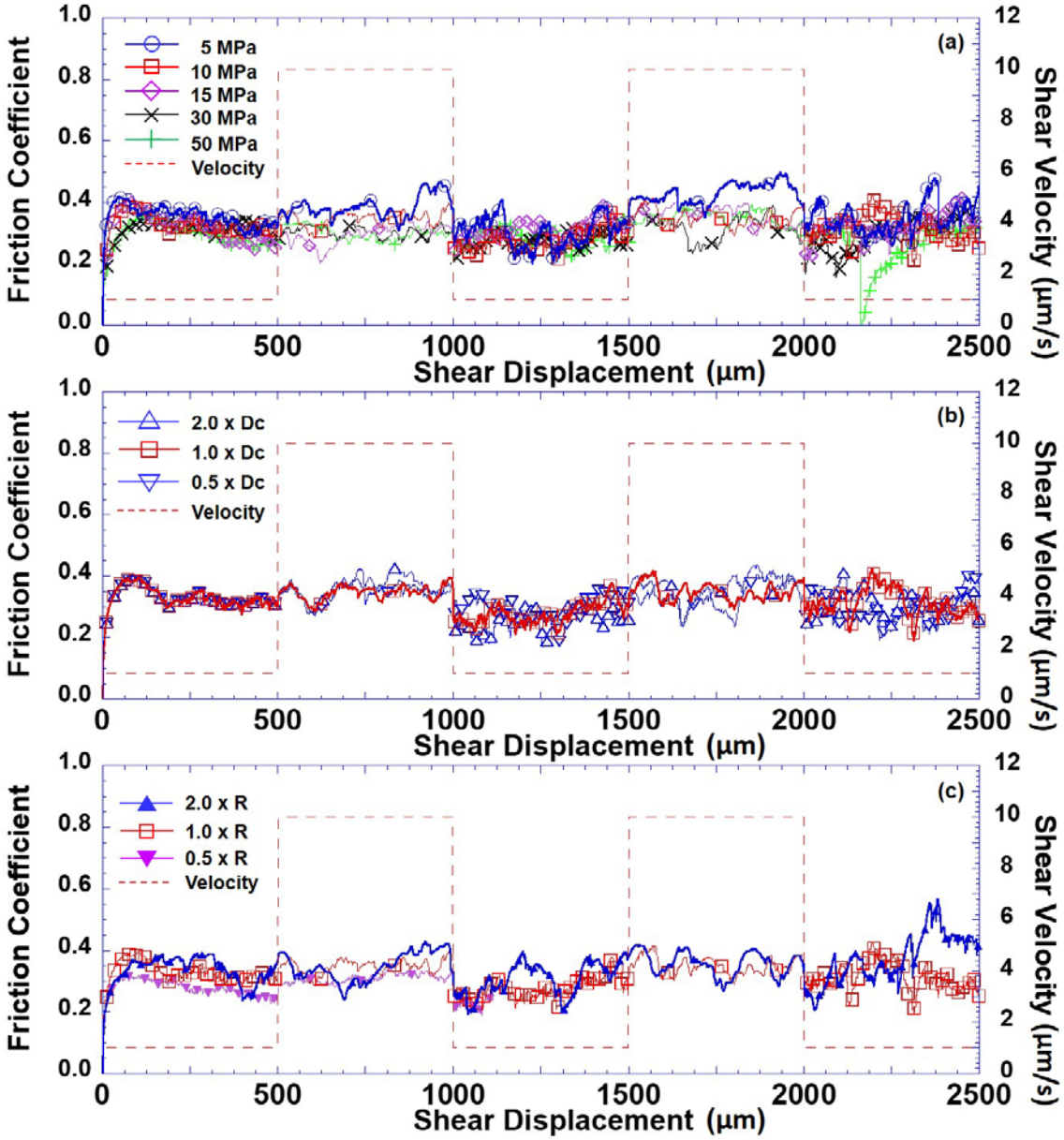

Figure 1-8. Friction evolution of a uniform mixture containing 75% quartz and 25% talc, at: (a) normal stresses of 5, 10, 15, 30, and 50 MPa; (b) with D_c set at 0.5, 1.0, and 2.0× characteristic slip distance; (c) with particle sizes of 0.5, 1.0, and 2.0× particle size,

5 Discussion

The numerical simulation results suggest that evolution of shear strength and stability of the simulated fault gouge is largely related to weight percentage and texture of the talc in the mixture. It is observed that for uniform mixtures, a relatively small amount of talc (~25% in weight percentage) can significantly weaken the fault; while for layered mixtures, a minimal amount of talc (a relative thickness of 3-particles) can provide the same level of influence. These results in turn pose questions of what the possible mechanics behind the observed evolution trends are and their implications. The following discussion examines the slip weakening law, by examining: fluctuations within the numerical friction measurements, the influence of localization effects of shear due to heterogeneity, the effect of platen rigidity and system stiffness, the stability of the calculated slip and mechanism for frictional healing, and the scaling of stability parameters in the two-dimensional numerical model.

5.1 Model validation and stress fluctuations

The frictional evolution of 75% quartz and 25% talc with a slip weakening friction law and constant friction is used to validate the effect of the friction law. **Figure 1-9** shows the comparison between friction evolution using both friction constitutive relations (slip weakening and constant) under a normal stress of 10 MPa. Both laws yield similar magnitudes of friction coefficient, however, the effect of instantaneous friction evolution

is only observed while using a slip weakening law. This identifies the key impact of the contact-contact slip weakening law in defining ensemble behavior.

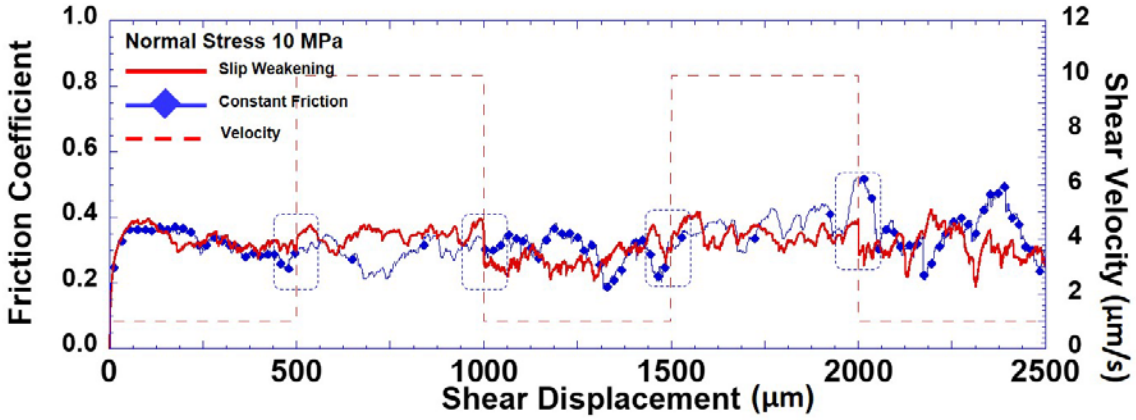

Figure 1-9. Contact model validation with comparison of velocity-stepping shear experiments on uniform mixtures with 75% quartz and 25% talc using models with a slip weakening friction law or constant friction. The dashed rectangle highlights the frictional evolution after the velocity steps. Shear experiments with implemented slip weakening model show clear frictional evolution at the velocity steps while it is difficult to observe a clear evolution of friction at velocity steps with a constant friction law.

Both dimensionality and particle size have a major influence on fluctuations in friction evolution data [Knuth and Marone, 2007]. In 2-D laboratory experiments, it is common to observe frictional fluctuation magnitudes of 0.1~0.15. Our simulation results show similar or even smaller amplitudes of fluctuations.

Becasue the simulation results show relatively large fluctuations in the frictional evolution (of the order of 0.1~0.2), the resulting $(a - b)$ values need to be similarly scaled, which are one order-of-magnitude smaller than the fluctuations; they are originally too small and will be lost inside the noise should laboratory scale values be used (in the order of 0.001). Therefore, in order to capture the evolution of friction due to velocity changes,

we implement $(a-b)$ values one magnitude larger than the laboratory measured $(a-b)$ values to capture the rate-and-state behavior. This is further discussed in Section 5.7

Large fluctuations are observed in frictional evolution in quartz-rich samples, especially in those with quartz content greater than 75%. This may due to the nature of the 2-D configuration of this study. Particle dimensionality is associated with large fluctuations of shear strength especially in a 2-D configuration [*Knuth and Marone*, 2007]. However, the fluctuations in shear strength in talc-rich samples are much smaller than those in quartz-rich samples (this study). We believe there are two main governing factors influencing the shear strength fluctuations in our model, namely: particle abundance (particle sizing), and inter-particle friction coefficient. **Figure 1-10** (a) (b) shows a comparison of frictional evolution of pure quartz during dynamic shearing with normal and reduced particle size (half of original particle size in this study, D_c value for quartz analog is adjusted accordingly). Smaller fluctuations are observed in the simulation with smaller particles. The magnitude of these fluctuations is not so significant in the context of this study compared to the exponentially increased computational cost in eliminating them. Inter-particle friction coefficient is another important factor which may govern the fluctuations of the bulk shear strength. In this study, the mineral analogs are geometrically defined as circular particles without any angularity, with the rotation of particles also restricted. Therefore, inter-particle friction coefficient may have a strong effect on the dilation behavior of particles. **Figure 1-10** (b) also shows frictional evolution of a quartz analog with artificially reduced inter-particle friction coefficient (0.05), from which a reduction in

shear strength fluctuation is observed. However, the ensemble shear strength is also reduced significantly with the reduction of inter-particle friction coefficient.

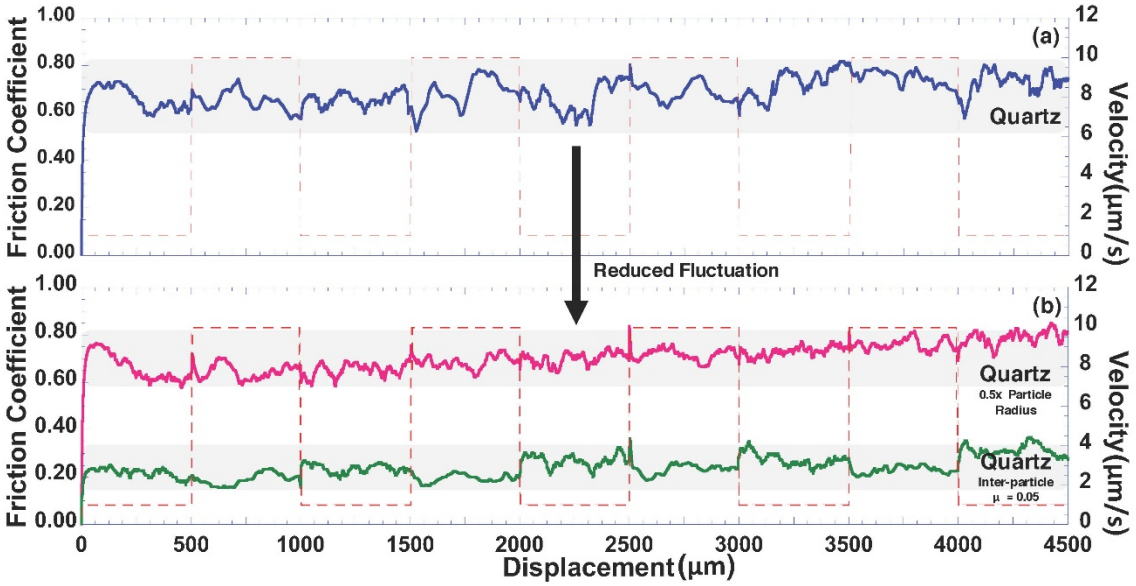

Figure 1-10. (a) Frictional evolution of pure quartz analog showing large fluctuations; (b) Frictional evolution of pure quartz analog with reduced particle size (0.5×) and reduced inter-particle friction coefficient (0.05) shows reduced fluctuations.

5.2 Comparison with established rate and state contact models

Rate and state dependent frictional evolution has been previously implemented into particle dynamics simulations (*Abe et al.*, 2002). A full rate and state constitutive relation was implemented at contact level in their approach, with the state variable θ (described in equation (5)) updated by local relative shear velocity and contact surface parameters. The contact model was implemented in a Lattice Solid Model, with simulation results suggesting a good match with theoretical bare-surface rate and state models and laboratory

experiments. The results also indicated that critical slip distance D_c is related to fault roughness. However, this approach is too computationally expensive to carry out using the large number of particles we use. Another approach (*Morgan*, 2004) simplified the complex rate and state constitutive relation by implementing a time dependent frictional healing constitutive law onto contacts. The constitutive relation of friction in this model is described by equation (16) through (17) as follows:

$$\mu_p^a = \mu_p^0, \quad t = 0 \tag{16}$$

$$\mu_p^a = \mu_p^0 + b\ln(t), \quad t > 0 \tag{17}$$

where μ_p^a is the time-dependent interparticle friction coefficient and b is a scalar coefficient. This constitutive law was tested in a simulated gouge assembly consisting of circular shaped particles with three different radii. Dynamic shear experiment under periodic boundary condition were conducted on the assembly to show that the model delivered a good match with laboratory hold-slide-hold experiments on fault gouge [*Marone*, 1998b].

The constitutive relation of friction described in this study is a slip weakening law. Compared to the full implementation of rate and state friction law described above, the state variable θ is not included in the slip weakening law due to the high computational cost to update θ on every contact through solving a series of nonlinear equations. Also, we do not implement time-dependent frictional healing onto each contact compared to the second example stated above. This will make the simulation of long term friction evolution under hold-slide-hold conditions impractical for our model. However, the focus of this study is not in precisely simulating the micro-mechanisms of rate and state friction,

implementing even second-order mechanisms. Instead, we simplify the problem by implementing a slip weakening law to study instantaneous friction evolution response upon velocity steps and focus on the response of mineral mixtures. Our implementation is best suited for studying the transitional behavior of stability of minerals mixtures consisting of minerals with different stability parameters (a and b values). Additionally, our implementation also shows a good match with laboratory results of transitional behavior in stability using quartz and talc mixtures, which implies the validity and capacity of our simplification in predicting this transitional behavior of stability on mineral mixtures.

5.3 Shear localization within the slip zone and effect of shear zone thickness

In this study, numerical double direct shear tests are conducted on gouge mixtures with two representative structural distributions of talc. Observations suggest that the spatial distribution of talc has a strong influence not only on the frictional strength but on slip stability as well. These strong effects may be caused by enhanced shear localization corresponding to the spatial distribution of talc. **Figure 1-11** shows a displacement map of the assembly (uniform mixture, 75% quartz and 25% talc; layered mixture, relative talc layer thickness of 8) and the distribution of slipped contacts at the end of representative numerical runs with both uniform (upper row) and textured mixtures (lower row). The displacement maps show that for uniform mixtures, there is a high degrees of particle rearrangement, and shear planes are likely to form within the assembly (from upper left to lower right). However, for layered mixtures, the shear plane is more horizontal, matching the location of the talc layer. Therefore, we suggest that for uniform mixtures, the

localization zones tend to bridge between the two shear platens with an inclined shear zone across the sample. For textured mixtures, the localization pattern appears to be similar to that for uniform mixtures with very little talc present in the sample (first column of **Figure 1-11**). However, with a relative layer thickness larger than 3-particles, slip contacts are mainly present in the talc layer while few slipped contacts are present in the surrounding quartz matrix. This observation suggests that in structured (layered) samples, slip is easily mobilized on the interfaces or inside the weak layer. When slip events occur mostly on the layer interfaces or inside the weak layer, the bulk shear strength is governed by the weak layer and exhibits similar behavior to that for pure talc.

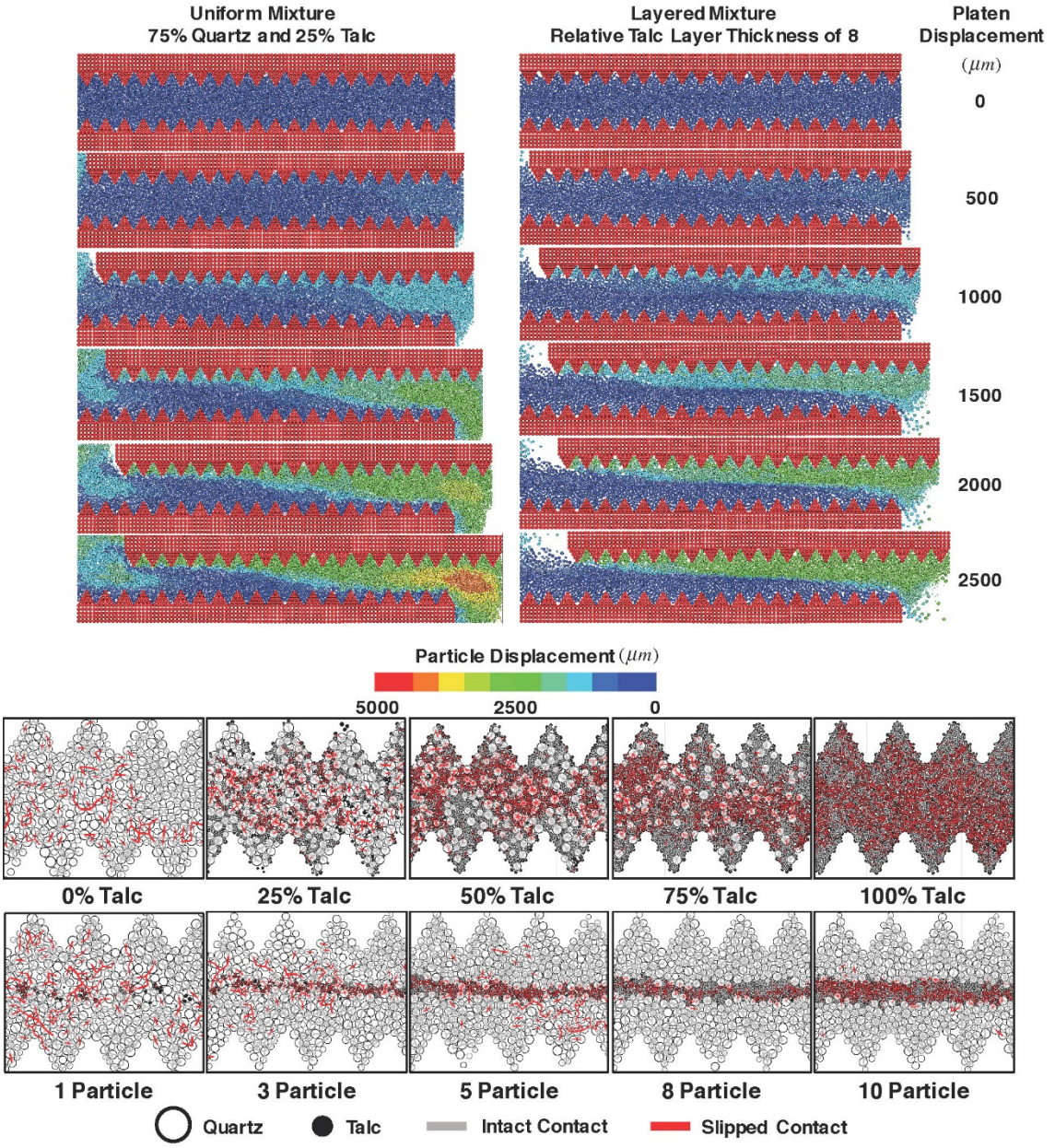

Figure 1-11. Displacement map of uniform mixture (75% quartz and 25% talc, upper left) shows higher degree of particle rearrangement during shear while layered mixture (relative layer thickness of 8, upper right) shows distinctive shear localization along the intervening talc layer. Slipped contacts at the end-stage (steady friction, lower two rolls) of representative numerical runs. Representative plot of slipped contacts in uniform mixtures showing shear zones localized between the two shear platens (upper row). Representative plots of slipped contacts in layered mixtures showing shear zones localized inside or at the interfaces of the talc layer (lower row).

The same mechanism applies to the evolution of slip stability. Although talc exerts a strong influence on slip stability of the gouge, the scattered talc particles in uniform mixtures exert less impact on the bulk slip stability than the localized talc layer. This is mostly explained since slip tends to occur around and between talc particles due to the substantially lower contact friction. A thicker talc layer can greatly promote creep in the gouge, changing from velocity-weakening to velocity-strengthening. However, this transition is accompanied by a significant reduction in shear strength. Therefore, talc has a two-fold influence: increasing the stability as evident in the ensemble parameters $(a - b)$ but simultaneously reducing the shear strength of the fault.

These observed localization effects are consistent with those observed previously [*Morgan*, 2004]. In addition, previous studies also suggest that there is a localization effect on weakening as well, indicating that the slipped localization patch will become even weaker. In this study, we did not consider, at the contact level, the further weakening localization of a slipped weak patch since there is a further evolution law defined beyond slip weakening. This further effect in weakening is, however, out of the scope of our study. We consider the results and conclusions of this study, i.e. the transitional behavior of slip stability and evolution of transport behavior of mineral mixtures may not be heavily impacted by this further weakening of localization. This is due to the nature of this study which is focused on the bulk weakening effect of frictionally weak minerals.

Shear zone thickness is an important parameter to determine the relative shear velocity between particles. Thicker shear zones feature lower relative shear velocity between particles than thinner zones. In this study, the slip-weakening law is defined as

global velocity and local strain based, i.e. the local friction evolution is calculated by the global reference velocity of the previous velocity step, the global load point velocity, local slip state, and local accumulated slip distance (described in the numerical methods section). We do not take into account local relative shear velocity. Therefore, shear zone thickness will not impose a significant effect on the results and conclusions of this study. This simplification is specific to this study and shear zone thickness must be considered in the scenario of precisely modeling the rate and state behavior, however, this is beyond the scope of this study.

Grain shape is another important factor in controlling shear localization [*Kock and Huhn*, 2007]. Talc is a microscopically platy mineral, which is different from the circular shaped particles we use in this study. However, despite the difference in representation, our simulation results of transitional behavior in shear strength and slip stability are consistent with previous laboratory experiments, which implies that circular shaped particles may be sufficient in deriving the transitional behavior of mineral mixtures. Regardless, the effect of grain shape is important and need to be further explored in DEM simulation.

5.4 Effect of system stiffness and platen rigidity

In this work, a slip-weakening contact law is implemented, rather than full rate-state behavior. Where we assume system stiffness to be infinitely large, this will always result in stable slip regardless of critical stiffness of the contact and sign of $(a - b)$, although velocity weakening behavior may still evolve; this will be an index of the

potential for unstable behavior. Thus, this study contributes to the understanding of the true mechanism and potential for unstable behavior as there is an intrinsic system stiffness that must be accommodated in nature in assessing the potential for unstable slip. In other words, we use the metric of velocity/slip weakening as an absolute measure of the potential for unstable slip, unmodulated by an arbitrary system stiffness.

5.5 Dilation in granular systems under dynamic shearing

As discussed in the results section, the initial strong dilation of quartz upon shearing is observed. This behavior is drastically different from the cyclic dilation-compaction of talc in response to velocity up-steps and velocity down-steps. The mechanism of dilation/compaction and the concept of force chain generation and brittle failure has already been described in previous studies [*Morgan and Boettcher*, 1999; *Anthony and Marone*, 2005]. Essentially, in granular systems, dilation, compaction, and compliant shear deformation during dynamic shearing is governed by the generation and breakage of force chains. The same theory applies in our model. We propose that the differences in dilatant behavior upon dynamic shearing may be due to differences in contact elastic stiffness and the inter-particle friction coefficient. Quartz analog particles feature much higher contact stiffness (essentially effective modulus) and inter-particle friction coefficient than talc analog particles (refer to **Table 1-1**). High elastic stiffness and inter-particle coefficients contribute to a higher degree of resistance in particle self-rearrangement during dynamic shearing, thus promoting strong dilation. Furthermore, this high resistance in self-rearrangement may delay the prompt reaction to changes in shear velocity. This may be the

reason why no significant compaction is observed during velocity down-steps in the quartz-rich samples. This may also explain the large initial dilation of pure quartz and the quartz rich analog during dynamic shearing since it takes more shear displacement for the particles in these assemblies to reach a dynamic equilibrium. In contrast, talc particles feature a significantly lower contact stiffness and inter-particle friction coefficient, which greatly reduces the resistance to particle self-rearrangement during dynamic shearing. Therefore, the assembly reacts more quickly to changes in shear velocity. The self-rearrangement resistance can also be affected by the abundance of particles. **Figure 1-12** (a) shows the evolution of porosity of pure quartz over 4500 microns of shear displacement. The porosity evolution of quartz with reduced particle size is also shown **Figure 1-12** (b). It can be clearly observed that for a quartz assembly, with half-sized particles (more particles overall), after ~1200 μm of shear displacement the assembly reaches a dynamic equilibrium as indicated by a halted increase in overall porosity. This is significantly faster than the original evolution of pure quartz (~2000 μm) in reaching dynamic equilibrium. But in both cases, the tendency of dilation in quartz is strong and the porosity evolution is of similar magnitude.

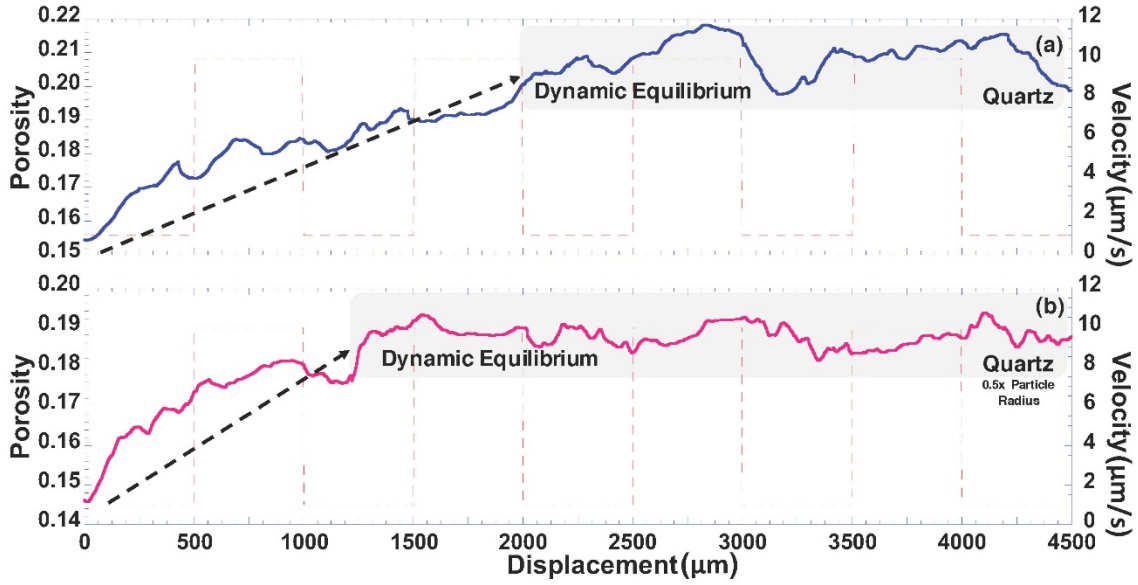

Figure 1-12. (a) Porosity evolution of pure quartz analog over a shear displacement of 4500 μm. Dynamic equilibrium is reached at ~2000 μm of shear displacement; (b) Porosity evolution of pure quartz analog with reduced particle radius over a shear displacement of 4500 μm, dynamic equilibrium is reached at ~ 1200 μm of shear displacement.

In the quartz-talc analog mixtures, the inter-particle elastic stiffness of a quartz-talc contact is taken by connecting the contact stiffness of quartz and talc in series, with the inter-particle friction coefficient is taken as the minimum of the two. In this case, talc will dominate in determining the contact stiffness. Essentially this will cause increased weakening on the quartz particles connected by talc particles (due to lowered contact elastic stiffness and talc-dependent inter-particle friction coefficient). Meanwhile, the reduction in inter-particle friction coefficient and elastic stiffness also contributes to the reduction in resistance to self-rearrangement during dynamic shearing, thereby reducing the dilation tendency, which eventually leads to the transition from strong dilation (pure quartz) to cyclic dilation and compaction (pure talc).

There are other properties affecting the dilation of granular assemblies, such as particle shape, angularity and surface roughness. The study of the effects of these multiple parameters are important to illuminate mechanisms of the shearing of granular materials, but is beyond the scope of this study.

5.6 Stability of slip events

Slip events at contacts may and will occur in the gouge assembly once shear begins. It is worth noting that not all contacts will slip at once under dynamic shearing due to particle packing and local effects. Slip is triggered once the Coulomb criterion is reached locally, and evolves according to a prescribed slip-weakening law as the slip proceeds. Once local slip occurs, under the assumption that the system stiffness is infinite, the calculated slip at the sliding contact will always be stable, but will evolve to a new state following the slip weakening law and according to local slip distance. However, if local contact slip does not occur at a given time, the friction coefficient will remain constant and not evolve. In any fault gouge sample, there are both contacts undergoing slip as well as those that are stationary. Therefore, the ensemble friction evolution is a combination of local friction evolution (either undergoing slip weakening or not) of every contact in the assembly.

5.7 Scaling of empirical stability parameters and uncertainties

In the DEM model, there are inevitable differences and conversions between grain-grain scale mechanical parameters and macroscopic mechanical parameters. For example, the macroscopic elastic modulus is converted into an effective modulus, and through normal to shear stiffness ratio, effective modulus is then converted to normal and shear contact stiffness. These conversions map the grain-grain scale parameters from macroscopic parameters. The same rules also apply to stability parameters. Considering the fluctuation of the 2-D numerical shear model, the stability parameters measured from the bulk stability evolution data differ from those used at grain-grain scale. Particularly, the stability parameters from curve fitting are of similar magnitude (0.01~0.05) to the stability parameters assigned at grain-grain scale. They are however, one order-of-magnitude larger than the laboratory measured parameters shown in **Figure 1-5** (b) (0.001~0.008). This is due to the two-dimensional configuration generating a relatively large amount of noise in the frictional evolution [*Knuth and Marone*, 2007], which prevents clear analysis of stability parameters at the laboratory scale. Therefore, the use of relatively large and artificial stability parameters in two-dimensional models helps to identify the transitional behaviors in frictional strength and slip stability.

Uncertainties remain since simplifications and assumptions have been made for this numerical study. Specifically, the mineral particles are assumed to be circular and a slip-weakening constitutive relation has been taken as a simplification of rate and state constitutive behavior. These assumptions, might not be applicable in every situation, but serve well in reproducing the transitional behavior of shear strength and slip stability of

frictionally strong/weak mineral mixtures, as well as predicting evolutionary trends in permeability. Besides, the method we use to calculate the resultant stability parameters for quartz-talc mineral contacts reveals a potential relation of the resultant stability parameters of contacts between surfaces with drastically different stability properties.

6 Conclusions

A DEM model is established to simulate the mechanical responses of synthetic gouge mixtures consisting of a quartz and talc analogs. Direct shear experiments with pre-defined velocity up-steps and down-steps were conducted on both uniform and textured mixtures. This is achieved by altering the weight percentage of talc in uniform mixtures and the relative thickness of the talc layer in textured (layered) mixtures, and in then analyzing experimental results. The following conclusions are drawn:

1. Talc has a significant weakening effect on the shear strength of quartz-rich fault gouges. This effect is enhanced when talc forms a through-going layer in the gouge.
2. Relatively small amounts of talc (10% to 25% talc in the uniform mixtures or 3-particles to 5-particles in the textured mixtures) can transform the stability behavior of the gouge from velocity-weakening to velocity strengthening.
3. Minerals with high elastic modulus and frictional resistance at contacts tend to dilate universally upon slip, while minerals with low elastic modulus and frictional resistance dilate during velocity up-steps but compact quickly during velocity down-steps.

4. Quartz tends to be dilation dominant and thus an increase in permeability could be expected in quartz-rich faults during slip events; while talc also dilates, but compacts much faster, therefore a decrease in permeability could be expected in talc-bearing faults.

The numerical modeling-derived conclusions suggests that DEM modeling is capable of simulating the shear strength and stability evolution of granular fault gouge using a simplified rate-state friction law. Also, it is possible to simulate gouge with complex mineralogical composition and with varying degrees and forms of heterogeneity. The analysis of coordination number and porosity evolution suggest new methods to examine the nature of permeability evolution of faults during the seismic cycle.

References

Abe, S., and K. Mair (2009), Effects of gouge fragment shape on fault friction: New 3D modelling results, *Geophys. Res. Lett.*, *36*(23), 2–5, doi:10.1029/2009GL040684.

Abe, S., J. H. Dieterich, P. Mora, and D. Place (2002), Simulation of the influence of rate- and state-dependent friction on the macroscopic behavior of complex fault zones with the lattice solid model, *Pure Appl. Geophys.*, *159*(9), 1967–1983, doi:10.1007/s00024-002-8718-7.

Abe, S., H. van Gent, and J. L. Urai (2011), DEM simulation of normal faults in cohesive materials, *Tectonophysics*, *512*(1–4), 12–21, doi:10.1016/j.tecto.2011.09.008.

Ampuero, J. P., and Y. Ben-zion (2008), Cracks, pulses and macroscopic asymmetry of dynamic rupture on a bimaterial interface with velocity-weakening friction, *Geophys. J. Int.*, *173*(2), 674–692, doi:10.1111/j.1365-246X.2008.03736.x.

Anthony, J. L., and C. Marone (2005), Influence of particle characteristics on granular friction, *J. Geophys. Res. B Solid Earth*, *110*(8), 1–14, doi:10.1029/2004JB003399.

Antonellini, M. A., and D. D. Pollard (1995), Distinct element modeling of deformation bands in sandstone, *J. Struct. Geol.*, *17*(8), 1165–1182, doi:10.1016/0191-8141(95)00001-T.

Bos, B., and C. J. Spiers (2002), Frictional-viscous flow of phyllosilicate-bearing fault rock: Microphysical model and implications for crustal strength profiles, *J. Geophys. Res.*, *107*(B2), 2028, doi:10.1029/2001JB000301.

Burbidge, D. R., and J. Braun (2002), Numerical models of the evolution of accretionary wedges and fold-and-thrust belts using the distinct-element method, *Geophys. J. Int.*, *148*(3), 542–561, doi:10.1046/j.1365-246x.2002.01579.x.

Carpenter, B. M., C. Marone, and D. M. Saffer (2009), Frictional behavior of materials in the 3D SAFOD volume, *Geophys. Res. Lett.*, *36*(5), 1–5, doi:10.1029/2008GL036660.

Collettini, C., A. Niemeijer, C. Viti, and C. Marone (2009), Fault zone fabric and fault weakness, *Nature*, *462*(7275), 907–910, doi:10.1038/nature08585.

Cundall, P. A., and O. D. L. Strack (1979), A discrete numerical model for granular assemblies, *Géotechnique*, *29*(1), 47–65, doi:10.1680/geot.1979.29.1.47.

Dieterich, J. H. (1978), Time-dependent friction and the mechanics of stick-slip, *Pure Appl. Geophys. PAGEOPH*, *116*(4–5), 790–806, doi:10.1007/BF00876539.

Dieterich, J. H. (1979a), Modeling of rock friction 1. Experimental results and constitutive equations, *J. Geophys. Res. Solid Earth*, *84*(B5), 2161–2168, doi:10.1029/JB084iB05p02161.

Dieterich, J. H. (1979b), Modeling of rock friction 2. Simulation of preseismic slip, *J. Geophys. Res. Solid Earth*, *84*(B5), 2169–2175, doi:10.1029/JB084iB05p02169.

Engelder, J. T., J. M. Logan, and J. Handin (1975), The sliding characteristics of sandstone on quartz fault-gouge, *Pure Appl. Geophys. PAGEOPH*, *113*(1), 69–86, doi:10.1007/BF01592900.

Fang, Y., D. Elsworth, C. Wang, T. Ishibashi, and J. P. Fitts (2017), Frictional stability-permeability relationships for fractures in shales, *J. Geophys. Res. Solid Earth*, *122*(3), 1760–1776, doi:10.1002/2016JB013435.

Faulkner, D. R., and E. H. Rutter (2001), Can the maintenance of overpressured fluids in large strike-slip fault zones explain their apparent weakness?, *Geology*, *29*(6), 503–506, doi:10.1130/0091-7613(2001)029<0503:CTMOOF>2.0.CO;2.

Guan, C., J. Qi, N. Qiu, G. Zhao, Q. Yang, X. Bai, and C. Wang (2012), Macroscopic Young's Elastic Modulus Model of Particle Packing Rock Layers, *Open J. Geol.*, *2*(July), 198–202, doi:10.4236/ojg.2012.23020.

Guo, Y., and J. K. Morgan (2004), Influence of normal stress and grain shape on granular friction: Results of discrete element simulations, *J. Geophys. Res. B Solid Earth*, *109*(12), 1–16, doi:10.1029/2004JB003044.

Hieher, P. Y. (1996), Elastic Properties of Soils, *J. Geotech. Eng.*, *122*(August), 641–648.

Ikari, M. J., C. Marone, and D. M. Saffer (2011), On the relation between fault strength and frictional stability, *Geology*, *39*(1), 83–86, doi:10.1130/G31416.1.

Knuth, M., and C. Marone (2007), Friction of sheared granular layers: Role of particle dimensionality, surface roughness, and material properties, *Geochemistry, Geophys. Geosystems*, *8*(3), doi:10.1029/2006GC001327.

Kock, I., and K. Huhn (2007), Numerical investigation of localization and micromechanics in a stratified soil specimen, *J. Struct. Geol.*, *29*(10), 1679–1694, doi:10.1016/j.jsg.2007.07.013.

Mair, K., and C. Marone (1999), Friction of simulated fault gouge for a wide range of velocities and normal stresses, *J. Geophys. Res. Solid Earth*, *104*(B12), 28899–28914, doi:10.1029/1999JB900279.

Marone, C. (1998a), Laboratory-Derived Friction Laws and Their Application To Seismic Faulting, *Annu. Rev. Earth Planet. Sci.*, *26*(1), 643–696, doi:10.1146/annurev.earth.26.1.643.

Marone, C. (1998b), The effect of loading rate on static friction and the rate of fault healing during the earthquake cycle, *Nature*, *391*(6), 69–72, doi:10.1038/nature34157.

Marone, C., C. B. Raleigh, and C. H. Scholz (1990), Frictional behavior and constitutive modeling of simulated fault gouge, *J. Geophys. Res. Solid Earth*, *95*(B5), 7007–7025, doi:10.1029/JB095iB05p07007.

Melosh, H. J. (1996), Dynamic weaking of faults by acoustic fluidization, *Nature*, *379*(February 1996), 601, doi:10.1038/379601a0.

Moore, D. E., and D. A. Lockner (2011), Frictional strengths of talc-serpentine and talc-quartz mixtures, *J. Geophys. Res. Solid Earth*, *116*(1), 1–17, doi:10.1029/2010JB007881.

Moore, D. E., and M. J. Rymer (2007), Talc-bearing serpentinite and the creeping section of the San Andreas fault, *Nature*, *448*(7155), 795–797, doi:10.1038/nature06064.

Morgan, J. K. (1999), Numerical simulations of granular shear zones using the distinct element method 2 . Effects of particle size distribution and interparticle, *J. Geophys. Res.*, *104*(B2), 2721–2732.

Morgan, J. K. (2004), Particle dynamics simulations of rate- and state-dependent frictional sliding of granular fault gouge, *Pure Appl. Geophys.*, *161*(9–10), 1877–1891, doi:10.1007/s00024-004-2537-y.

Morgan, J. K., and M. S. Boettcher (1999), Numerical simulations of granular shear zones using the distinct element method: 1. Shear zone kinematics and the micromechanics of localization, *J. Geophys. Res.*, *104*(B2), 2703–2719, doi:10.1029/1998JB900056.

Morgan, J. K., and P. J. McGovern (2005), Discrete element simulations of gravitational volcanic deformation: 1. Deformation structures and geometries, *J. Geophys. Res. B Solid Earth*, *110*(5), 1–22, doi:10.1029/2004JB003252.

Niemeijer, A., C. Marone, and D. Elsworth (2010), Fabric induced weakness of tectonic faults, *Geophys. Res. Lett.*, *37*(3), 1–5, doi:10.1029/2009GL041689.

Niemeijer, A. R., and C. J. Spiers (2006), Velocity dependence of strength and healing behaviour in simulated phyllosilicate-bearing fault gouge, *Tectonophysics*, *427*(1–4), 231–253, doi:10.1016/j.tecto.2006.03.048.

Ouyang, Z., and D. Elsworth (1993), Evaluation of groundwater flow into mined panels, *Int. J. Rock Mech. Min. Sci.*, *30*(2), 71–79, doi:10.1016/0148-9062(93)90701-E.

Press, W., S. Teukolsky, W. Vetterling, B. Flannery, E. Ziegel, W. Press, B. Flannery, S. Teukolsky, and W. Vetterling (1987), *Numerical Recipes: The Art of Scientific Computing*.

Rathbun, A. P., F. Renard, and S. Abe (2013), Numerical investigation of the interplay between wall geometry and friction in granular fault gouge, *J. Geophys. Res. Solid Earth*, *118*(3), 878–896, doi:10.1002/jgrb.50106.

Rice, J. R. (1992), Fault Stress States, Pore Pressure Distributions, and the Weakness of the San Andreas Fault.

Ruina, A. (1983), Slip instability and state variable friction law, *J. Geophys. Res.*, *88*, 10359–10370, doi:10.1029/JB088iB12p10359.

Samuelson, J., D. Elsworth, and C. Marone (2011), Influence of dilatancy on the frictional constitutive behavior of a saturated fault zone under a variety of drainage conditions, *J. Geophys. Res. Solid Earth*, *116*(10), 1–17, doi:10.1029/2011JB008556.

Scholz, C. H. (1998), Earthquakes and friction laws, *Nature*, *391*(6662), 37–42, doi:10.1038/34097.

Sun, Z., D. N. Espinoza, and M. T. Balhoff (2016), Discrete element modeling of indentation tests to investigate mechanisms of CO2-related chemomechanical rock alteration, *J. Geophys. Res. Solid Earth*, *121*(11), 7867–7881, doi:10.1002/2016JB013554.

Di Toro, G., T. Hirose, S. Nielsen, G. Pennacchioni, and T. Shimamoto (2006), Natural and Experimental Evidence of Melt Lubrication of Faults During Earthquakes, *Science (80-.).*, *311*(5761), 647–649, doi:10.1126/science.1121012.

Chapter 2

Ensemble Shear Strength, Stability, and Permeability of Mixed Mineralogy Fault Gouge Recovered from 3D Granular Models

Abstract

We conduct numerical shear reactivation experiments on analog mixtures of quartz and talc gouge using a three-dimensional (3D) distinct element model (DEM). We follow the evolution of shear strength, slip stability, and permeability of the gouge mixture during dynamic shear and explore the mesoscopic mechanisms. A modified slip-weakening constitutive law is applied at contacts. We perform velocity-stepping experiments on both uniform, and layered mixtures of quartz and talc analogs. We separately vary the proportion of talc in the uniform mixtures and talc layer thickness in the layered mixtures. Shear displacements are cycled through shear velocities of 1 and 10μm/s. Simulation results show that talc has a strong weakening effect on shear strength - a thin shear-parallel layer of talc (~8.1 wt%) can induce significant weakening. However, the model offsets laboratory derived strong weakening effects of talc observed in uniform mixtures, implying the governing mechanisms may be the strong shear localization effect of talc, which is enhanced by its natural platy shape. Ensemble stability (a-b) can be enhanced by increasing talc content in uniform talc-quartz mixtures. No apparent influence of increasing talc layer thickness on (a-b) is observed in layered mixtures. Talc enhances compaction at velocity down-steps, potentially reducing fault permeability. Additionally, we show that

dimensionality significantly impacts the resolution of dynamic responses. 3D simulations are more representative of laboratory observed behavior. Numerical noise is shown to be of the order of ~0.1 of previous 2D counterparts. Evolution trends of stability parameters regarding the composition and structure of the fault gouge can be straightforwardly obtained from the 3D simulation. Our study elaborates a DEM approach to mechanistically investigate the mechanical and rheological response of faults during shearing and enhances the understanding of fault weakening mechanism.

1. Introduction

Seismic events commonly occur in mature faults consisting of fault cores and damage zones (Faulkner et al., 2010). Frictional response and stability of faults are usually governed by fault gouge present in the fault core. Extensive studies have documented the friction and stability of fault gouge under varied stress conditions, shear velocity regimes, and fluid saturations in the laboratory using natural and synthetic samples (Fang et al., 2014; Ikari et al., 2011; Mair and Marone, 1999). Fault gouge can contain mixtures of frictionally strong tectosilicates and weak phyllosilicates (Collettini and Holdsworth, 2004; Faulkner et al., 2003; Vrolijk and Van Der Pluijm, 1999; Wintsch et al., 1995), including talc (Giorgetti et al., 2015; Moore and Lockner, 2011; A. R. Niemeijer et al., 2010a). Talc can be derived from the metamorphic alteration of ultramafic rocks with silica-saturated hydrothermal fluids, and from dissolution of dolomite under the alteration of silica-rich fluids (D'Orazio et al., 2004; Escartín et al., 2008; Grasemann and Tschegg, 2012; Moore and Rymer, 2007; Peacock, 1987; Taylor and Huchon, 2002; Viti and Collettini, 2009).

Laboratory studies suggest that talc may exert a significant effect on the shear strength and slip stability of gouge mixtures. In order to strongly weaken the gouge, a ~50 wt% of talc is required in uniform mixtures (Moore and Lockner, 2011). Only ~4 wt% of talc is required to weaken the gouge in layered mixtures (Niemeijer et al., 2010). Laboratory shear tests using uniform mixtures of talc and strong minerals (quartz, calcite) show that talc has a dominant effect on shear strength at weight percentages of ~20% or higher (Giorgetti et al., 2015). The study of layered gouge mixture with talc, e.g., layered talc sandwiched by frictionally strong minerals, has always been a challenge in the laboratory due to the difficulty in preparing a uniform and consistent talc layer (Niemeijer et al., 2010), tracking localized shear deformation, and machanistcally analyzing shear deformation within the gouge layer during shearing. An alternative way to study the dynamic responses of gouge materials is to take advantage of numerical methods. One effective method is to conduct a similar study on friction evolution of synthetic fault gouge during dynamic shearing by discrete element methods (DEM) (Cundall and Strack, 1979). DEM has been successfully applied to the simulation of fault gouge and many other laboratory experiments on rocks and granular materials (Guo and Morgan, 2004; Morgan, 1999; Sun et al., 2016; Wang et al., 2017). Granular gouge materials are represented by an assembly of particles which can move independently within preset degrees of freedom. The dynamics of particles are updated by explicit representation of Newton’s second law, and the interaction of particles is evaluated by various constitutive contact models depending on different applications and scenarios.

DEM simulations of granular materials are usually carried out in two-dimensions for equivalent media and with compensation mechanisms to represent suppressed out-of-plane displacements (Morgan, 1999; Morgan and Boettcher, 1999; Wang et al., 2017). Gouge models constructed in 2D are widely adopted due to the significantly lower computational cost. However, the shape and dimensionality of particles can also affect the maximum shear strength of simulated faults (Abe et al., 2011; Ferdowsi et al., 2014; Knuth and Marone, 2007). Additionally, 2D models typically fail to reproduce out of plane particle interactions, lack particle interlocking mechanisms, and exaggerate shear dilation. Studies have been conducted both numerically and experimentally to investigate the effects of particle dimensionality on the shear strength of faults (Knuth and Marone, 2007). Unusual fluctuations in shear strength evolution are observed in laboratory double direct shear experiments using metal rods (representing 2D particles). Unrealistically low shear strength is also observed, and this is believed to be caused by free-rolling of the particles (rods).

The shear stability of faults is commonly described by rate and state friction law (Dieterich, 1992; Marone, 1998; Ruina, 1983). Shear stability of granular shear is analyzed by direct measurement of shear stress and shear displacement in the laboratory; it is also implemented in DEM simulations by introducing contact-based constitutive laws. A contact-based slip-weakening law has been implemented in 2D DEM simulations for slip stability analysis (Wang et al., 2017). Although a large number of studies and discussions have been carried out to investigate shear strength and slip stability of granular shear using 2D or 3D configurations (Anthony and Marone, 2005; Ferdowsi et al., 2014; Hazzard and

Mair, 2003; Knuth and Marone, 2007), few studies have combined slip stability and permeability evolution of gouge mixture containing frictionally weak minerals using 3D DEM simulation.

In this study, we complete 3D DEM simulations of granular gouge in shear experiments using quartz and talc analogs. Specifically, we explore the shear strength, slip stability, and permeability evolution of the mixture in the configurations of uniform and layered mixtures (*e.g.*, layered talc). The weight percentage of talc in these two configurations is systematically varied. By performing direct shear simulations with velocity steps, transitional behavior in shear strength and changes in the stability parameter $(a - b)$ are captured and its impact on permeability inferred. We present mechanistical analysis of the transitional behavior and report substantial discussions.

2. Method

Seismic events commonly occur in mature faults consisting of fault cores and damage zones (Faulkner et al., 2010). Frictional response and stability of faults are usually governed by fault gouge present in the fault core. Extensive studies have documented the friction and stability of fault gouge under varied stress conditions, shear velocity regimes, and fluid saturations in the laboratory using natural and synthetic samples (Fang et al., 2014; Ikari et al., 2011; Mair and Marone, 1999)

2.1 Model configuration

The 3D DEM model represents one symmetric half of the double direct shear configuration (Marone, 1998) (**Figure 2-1**). In this model, gouge analogs are confined between two saw-tooth grooved platens consists of particle clumps. The length of the shear platen is 20mm. The thickness of the gouge sample assembly is approximately 5mm including the platens; the exact thickness varies with mineral content. Virtual walls are generated outside of the assembly to prevent the extrusion of particles during shear. These virtual walls do not obey Newton's second law due to the lack of mass. However, they preserve linear elastic contact properties and can thus perform as elastic boundaries to the assembly.

The direct shear simulations are conducted under a normal stress (applied normal to the shear direction) of 10MPa with the stress magnitude maintained *via* a servo-loading algorithm. The algorithm constantly adjusts the relative velocity of the upper and lower platens to retain the normal stress within 0.5% of the preset magnitude (10MPa in this study). The 3D model simulates the full process of direct shear by the following steps:

1. Generate a domain, virtual walls, and shear platens;
2. Generate loosely distributed mineral analogs with an initial target porosity of 55%, allowing initial particle overlaps;
3. Equilibrate the assembly by iterating until the ratio of unbalanced forces to the sum of body force, applied force, and contact forces on one particle in all degrees of freedom (mechanical ratio) is less than 0.001;

4. Activate the servo-displacement algorithm to compact the sample until the normal stress (10MPa) is reached while maintaining the mechanical ratio below 0.001.
5. Actuate the upper platen in shear to a preset velocity and cycle between velocity steps.

The analog mixture is sheared through a full displacement of 500 μm at 1 $\mu m/s$ with the velocity then up-stepped to 10 $\mu m/s$ over a further 500 μm of shear displacement. The velocity is then decreased to 1 $\mu m/s$ and the process repreated. The maximum shear displacement for each simulation is 3500 μm, enabling a total of 6 successive steady states to be reached. The numerical simulation monitors the evolution of ensemble friction coefficient, sample layer thickness, average coordination number, and porosity of the gouge sample during dynamic shear. Shear stress is calculated from the unbalanced force on upper shear platen divided by effective shear area. Friction coefficient is then interpreted by the ratio of shear stress to normal stress. The sample layer thickness is calculated from the average distance between the two shear platens prescribing the outer boundary (the distance from the outer flat surface of the upper platen to the lower platen). Porosity is monitored in seven spherical control volumes distributed along the gouge analog. The diameter of each spherical control volumes is 750 μm. The locations (unit in mm) are $(\pm 4,0)$, $(\pm 3,0)$, $(\pm 2,0)$, $(0,0)$, in which $(0,0)$ is the geometric center of the compacted sample before shear.

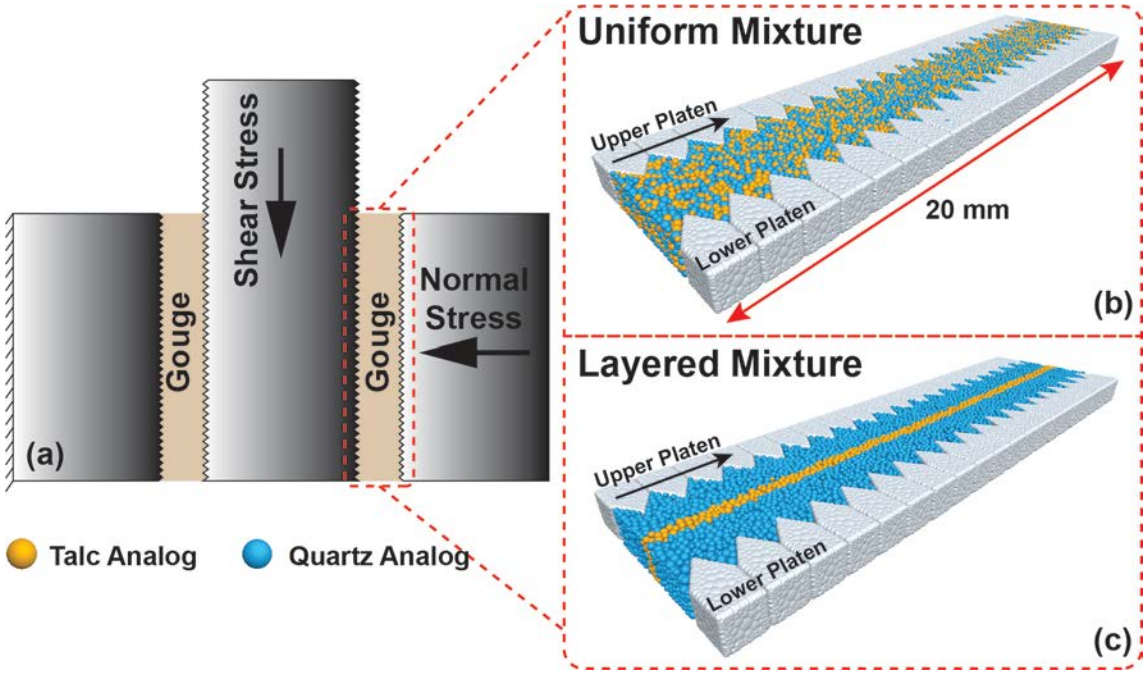

Figure 2-1. Model configuration represents one half of the double direct shear configuration (Mair and Marone, 1999). (a) Double direct shear configuration; (b) DEM model for homogeneous mixtures (red line marks the model scale; black arrow marks the direction of shear); (c) Layered mixture.

2.2 Contact Model

In order to reduce the rolling tendency of the uniformly spherical particles in the model and to thereby reproduce realistic particle interlocking effects, we use a contact model accommodating rolling resistance and linear elastic contact (Ai et al., 2011; Iwashita and Oda, 1998; Jiang et al., 2015; Wensrich and Katterfeld, 2012). This is effective in reducing the undesirable strong rolling effect of particles during simulation. Specifically, the contact model consists of linear elastic components in both the normal and shear direction (**Figure 2-2**(a)). All components act at a vanishingly small contacting area, with

only forces and moments transmitted. The contact force ($\boldsymbol{F}_c$) is resolved into normal (F_n) and shear components ($\boldsymbol{F}_S$). Magnitudes of shear force $\boldsymbol{F}_s$ is compared to a threshold F_s^{μ}, and if more than this magnitude allows contact slip with the friction coefficient evolving according to a slip-weakening constitutive relation. The iterative constitutive relation for normal and shear elastic components are:

$$\boldsymbol{F}_c = -F_n\hat{\boldsymbol{n}}_c + \boldsymbol{F}_S + \boldsymbol{F}_d \tag{1}$$

$$F_n = (F_n)_0 + k_n\Delta\delta_n \tag{2}$$

$$\boldsymbol{F}_s = (\boldsymbol{F}_s)_0 - k_s\Delta\boldsymbol{\delta}_s \tag{3}$$

$F_s^{\mu} = -\mu_0 F_n$ (before slip initiates); $F_s^{\mu} = -\mu F_n$ (after slip initiates) (4)

in which $(F_n)_0$, $(\boldsymbol{F}_s)_0$, and $\boldsymbol{F}_d$ are the normal force, shear force vector, and dashpot force vector (damping coefficient of 0.2 is implemented in both normal and shear direction); $\hat{\boldsymbol{n}}_c$ is the contact normal; k_n and k_s are the normal and shear contact stiffness; $\Delta\delta_n$ and $\Delta\boldsymbol{\delta}_s$ are the increments of local displacement and displacement vector in the normal and shear directions; μ_0 is the coulomb friction coefficient of the contact before slip initiates(also μ_{ref}); μ is the transient friction coefficient of the contact after slip initiates.

The contact moment ($\boldsymbol{M}_c$) is determined by the rolling resistance moment ($\boldsymbol{M}^{\mathrm{r}}$) determined by rolling resistance stiffness k_r, and local bend-rotation increment ($\Delta\boldsymbol{\theta}_b$). $\boldsymbol{M}^{\mathrm{r}}$ is updated as:

$$\boldsymbol{M}^{\mathrm{r}} = (\boldsymbol{M}^{\mathrm{r}})_0 - k_r\Delta\boldsymbol{\theta}_b \tag{5}$$

$$k_r = k_s\bar{R}^2 \tag{6}$$

$$\frac{1}{\bar{R}} = \frac{1}{R^{(1)}} + \frac{1}{R^{(2)}} \tag{7}$$

in which $(\boldsymbol{M}^{\mathrm{r}})_0$ is the rolling resistance moment vector of the previous time step; and $\bar{R}$ is the contact effective radius calculated from the radii ($R^{(1)}$ and $R^{(2)}$) of two contacting particles.

The rolling resistance moment is capped by a rolling resistance coefficient μ_r, particle properties (size, contact stiffness) and normal force. The rolling resistance moment ($\boldsymbol{M}^{\mathrm{r}}$) is checked against a threshold limit ($\boldsymbol{M}^{*}$), with $\boldsymbol{M}^{*}$ calculated according to equation (8). The rolling resistance moment is set as $\boldsymbol{M}^{*}$ if the resultant $\boldsymbol{M}^{\mathrm{r}}$ is greater than the threshold. This mechanism works in a sense similar as Coulomb's law of friction as,

$$\boldsymbol{M}^{*} = \mu_r \bar{R} \boldsymbol{F}_n \tag{8}$$

The implementation of this rolling resistance makes it feasible to simulate particle interlocking by restricting the rolling tendency of uniform spherical particles.

When slip occurs, instead of evaluating frictional behavior using Coulomb's law of friction, rate-and-state approach (Dieterich, 1979; Marone et al., 1990; Ruina, 1983; Scholz, 1998) is commonly applied. The rate and state friction laws are interpreted with a single degree of freedom elastic coupling system, and the associated constitutive relations implemented as,

$$\mu(V,\theta) = \mu_0 + aln\left(\frac{V}{V_0}\right) + bln\left(\frac{V_0\theta}{D_c}\right) \tag{9}$$

$$\frac{d\mu}{dt} = k\left(V_{lp} - V\right) \tag{10}$$

in which μ_0 is the reference friction coefficient prior to friction evolution; a and b are the empirical stability parameters associated with the material; V, V_{lp}, and V_0 are the current, load point, and reference sliding velocity; θ is the state variable; D_c is the characteristic slip distance; k is the system stiffness.

The commonly accepted evolutions for the state variables are the Dieterich and Ruina laws as,

$$\frac{d\theta}{dt} = 1 - \frac{V\theta}{D_c} \quad (Dieterich\ law) \tag{11}$$

$$\frac{d\theta}{dt} = \frac{V\theta}{D_c} ln\left(\frac{V\theta}{D_c}\right) \quad (Ruina\ law) \tag{12}$$

Both laboratory and simulation studies show that rate and state friction laws adequately describe seismic and frictional healing during fault slip events. DEM simulations involve updating friction evolution at many active contacts in every time step. Implementation of full rate and state friction laws for all contacts is currently computational ineffective (Abe et al., 2002). To reduce the computational cost, we assume that the system stiffness is infinitely large and implemented a modified slip-weakening response at each contact. The slip-weakening law is described as,

$$\mu_p = \mu_{ref} + aln\left(\frac{V_{lp}}{V_{ref}}\right) \tag{13}$$

$$\mu_{ss} = \mu_{ref} + (a-b)ln\left(\frac{V_{lp}}{V_{ref}}\right) \tag{14}$$

$$\mu = \begin{cases} \mu_p & D_{acc} = 0 \\ \mu_p - \left(\frac{\mu_p - \mu_{ss}}{D_c}\right) D_{acc} & 0 < D_{acc} < D_c \\ \mu_{ss} & D_{acc} \geq D_c \end{cases} \tag{15}$$

in which μ_p is the peak friction coefficient at the initiation of evolution; μ_{ss} is the presumed steady-state friction coefficient after evolution; μ_{ref} is the reference friction coefficient between particles; V_{lp} and V_{ref} are the load point velocity and reference velocity of the shear platens; a, b, and D_c are contact surface stability parameters and are not

necessarily identical to the laboratory derived values for rate and state friction; D_{acc} is the accumulative shear displacement on the contact.

This constitutive relation is implemented for each contact of the assembly. The behavior of this modified slip-weakening constitutive relation is shown in **Figure 2-2**(b). In the numerical implementation, the value of the current load point velocity and reference velocity is stored for each contact. The evolution of friction at contacts will evolve in the following manner:

1. The friction coefficient follows the (green) path shown in **Figure 2-2**(b) before local shear force reaches the friction threshold.
2. Once the local shear force reaches the threshold and triggers local slip, friction evolution follows the slip-weakening path (red path of **Figure 2-2**(b)).
3. The local friction coefficient reaches a steady-state (purple path in **Figure 2-2**(b)). Note that the final steady-state can be either velocity strengthening or weakening with both paths (black) shown for demonstration.

There are cases when a local slip on a contact halts before the full evolution of friction can occur. In such cases, the friction coefficient of the contact will remain as-is (shown as the blue dot in **Figure 2-2**(b)). The evolution continues once slip is reinitiated, and when the contact is still active. If the contact is no longer active, due to large shear displacement, then the friction evolution will halt. When a new contact forms, the friction evolution always follows the three stages noted above.

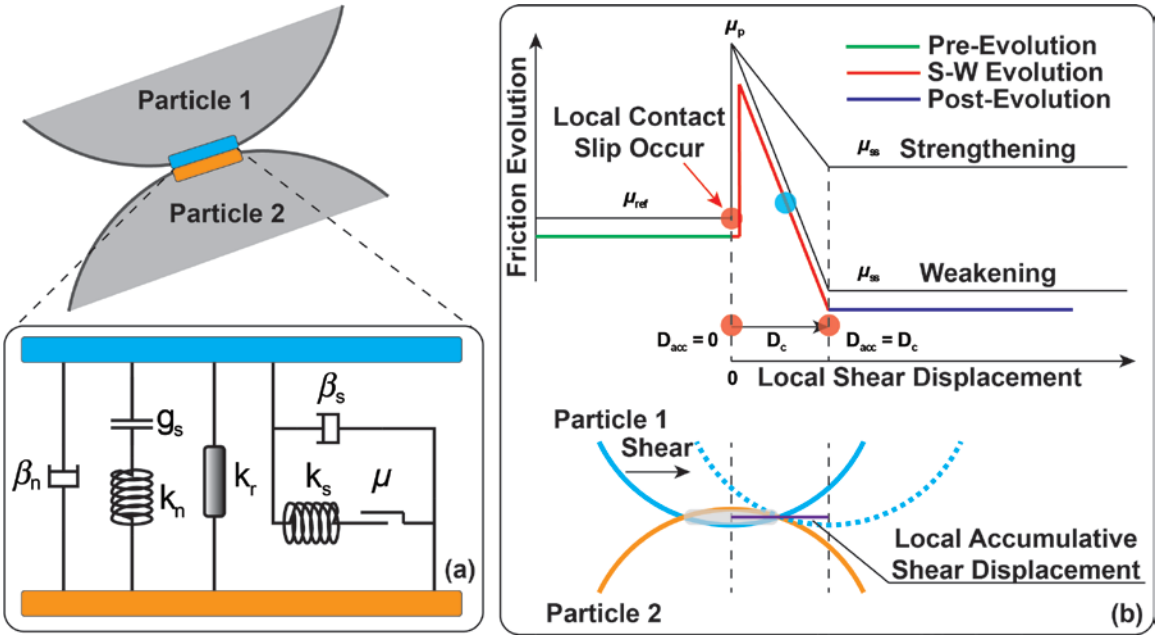

Figure 2-2. (a) Contact model between two particles comprises linear elastic components in the local shear and normal directions with a moment-based rolling resistant component (k_r); (b) modified slip-weakening constitutive relation acting at each particle-particle contact.

2.2 Mineral Analogs

We use quartz and talc analog particles to represent analog mixtures. Quartz and talc exhibit importantly contrasting frictional properties. Quartz is frictionally strong but with velocity neutral or weakening, while talc is frictionally weak, but velocity strengthening (Ikari et al., 2011). It is observed both in nature and the laboratory that small amounts of talc can greatly weaken the shear strength of a mineral assembly comprising a majority of strong minerals in the matrix (Giorgetti et al., 2015; Moore and Lockner, 2011; Moore and Rymer, 2007).

The elastic modulus of granular materials is dependent on particle size distribution, particle shape, mean stress, and is usually much smaller than that of the intact bulk materials (Guan et al., 2012). In this model, the elastic interaction between particles is governed by a combination of local elastic stiffness in the normal and shear directions. The normal and shear stiffness are derived from a calibrated effective modulus (E^*) and normal-to-shear stiffness ratio (κ^*) via,

$$k_n = \frac{AE^*}{L} \tag{16}$$

$$k_s = \frac{k_n}{\kappa^*} \tag{17}$$

where A is the virtual contact area between two particles, typically calculated with the smaller diameter of the two contact particles (πR_{min}^2); L is the distance between the centers of gravity of the two particles.

Notably, the effective modulus (E^*) is not equivalent to the macroscopic elastic modulus. This is directly assigned as a contact property in a mesoscopic sense. Nevertheless, effective modulus is related to the macroscopic elastic modulus, and the normal-to-shear stiffness ratio is related to Poisson's ratio. Specifically, the effective modulus is calibrated through a series of pseudo triaxial compression simulation on packs of candidate quartz and talc analogs, respectively. The calibration process is defined as:

1. Make initial estimations of the effective modulus and normal-to-shear stiffness ratio;
2. Generate an assemblage of candidate particles in a cylindrical vessel with a 3:2 height: diameter ratio;

3. Conduct pseudo triaxial compression tests under a normal stress of 10MPa up to an axial strain of 0.05%;
4. Calculate the resultant macroscopic elastic modulus from the stress-strain relation;
5. Repeat by varying normal-to-shear stiffness ratios (#1) until the macroscopic estimate is within 3% of literature-derived values.

The calibrated contact properties are presented in **Table 2-1**.

Table 2-1. Model parameters including calibrated elastic modulus for quartz and talc (Guan et al., 2012).

	Quartz Analog	Talc Analog	Unit
Density	2650	2800	kg/m^3
Radius	25-50	25-50	μm
Inter-particle Friction	0.3	0.1	[-]
Effective Modulus	35	1.0	GPa
Normal-to-shear Stiffness Ratio	1	1.5	[-]
Calibrated Elastic Modulus	9.35	0.94	GPa
Rolling resistance coefficient	0.5	0.3	[-]
Inter-particle a Value	0.0025	0.0050	[-]
Inter-particle b Value	0.0050	0.0025	[-]
Inter-particle D_c	50	25	μm

Density scaling (10^{12}) has been implemented in shear simulations, the corresponding time step is in the magnitude of $10^{-3}s$. The influence of density scaling is discussed in section 5.2.

In this study, there are often cases when contrasting mineral analog particles are in direct contact. In such cases, the contact surface stability parameters (a and b) are

calculated from the harmonic average of parameters for the two contrasting materials. The normal and shear stiffnesses are connected in series. The contact surface friction coefficient (μ) and characteristic slip distance (D_c) is determined by the smaller value of the two particles.

3. Simulation

We study the evolution of shear strength, slip stability, and permeability of quartz and talc mixtures in each of two configurations: a uniform mixture and as a layered mixture. We estimate the local permeability from the evolution of local porosity measured in seven spherical control volumes arranged along the shear localization zone. The relationship between the evolution of porosity and permeability is given by Samuelson et al., (2011),

$$\frac{k}{k_0} \cong (1 + \Delta\phi)^3 \quad (18)$$

where k/k_0 is the relative ratio of current to initial permeability and $\Delta\phi$ is the change in average local porosity.

The uniform mixtures comprise uniformly distributed quartz and talc analog particles representing mass fractions from 0:100% to 100:0% quartz: talc. The layered mixtures consist of a thin layer of talc analog sandwiched within a quartz matrix with a variable thickness of ~1-particle, 3-particles, 5-particles, 8-particles, and 10-particles across the talc layer at the initiation of each test. The detailed list of simulations is presented in **Table 2-2**.

Table 2-2. Simulation suite.

Name	Quartz Analog (wt%)	Talc Analog (wt%)	Talc Layer Thickness[a]	Sample Thickness[b](μm)	Number of Particles
qztc100-00	100%	0%	N/A	5998.91	19190
qztc90-10	90%	10%	N/A	5863.02	19117
qztc80-20	80%	20%	N/A	5762.72	19130
qztc70-30	70%	30%	N/A	5646.12	19076
qztc60-40	60%	40%	N/A	5519.43	19132
qztc50-50	50%	50%	N/A	5453.57	19121
qztc40-60	40%	60%	N/A	5393.31	19139
qztc30-70	30%	70%	N/A	5364.67	19197
qztc20-80	20%	80%	N/A	5347.15	19198
qztc00-100	00%	100%	N/A	5381.38	19192
qztc005	95.9%	4.1%	1 (~125 μm)	5958.33	19170
qztc010	91.9%	8.1%	3 (~250 μm)	5920.28	19114
qztc015	87.9%	12.1%	5 (~375 μm)	5908.96	19116
qztc020	83.4%	16.6%	8 (~500 μm)	5869.70	19063
qztc030	76.6%	23.4%	10 (~750 μm)	5810.17	19026

[a] The relative thickness of the talc analog layer is determined by the approximate number of particles across the initial talc layer, the approximate width in μm are also listed.

[b] The sample thickness is measured at the initiation of shear.

4. Results

Direct shear simulations with a prescribed velocity schedule are conducted for mixtures of quartz and talc analogs under controlled normal stress and prescribed shear

velocities. Both uniform and layered mixtures are used to define the evolution of shear strength, stability parameters, and permeability.

4.1 Evolution of shear strength

Simulations of direct shear tests are conducted on uniform and layered mixtures of quartz and talc analogs. Since the normal stress in all simulations is identical (10MPa), we use the shear strength evolution to represent the ensemble friction coefficient of the mixture. The full friction evolution of the representative uniform mixtures and layered mixtures are shown in **Figure 2-3**.

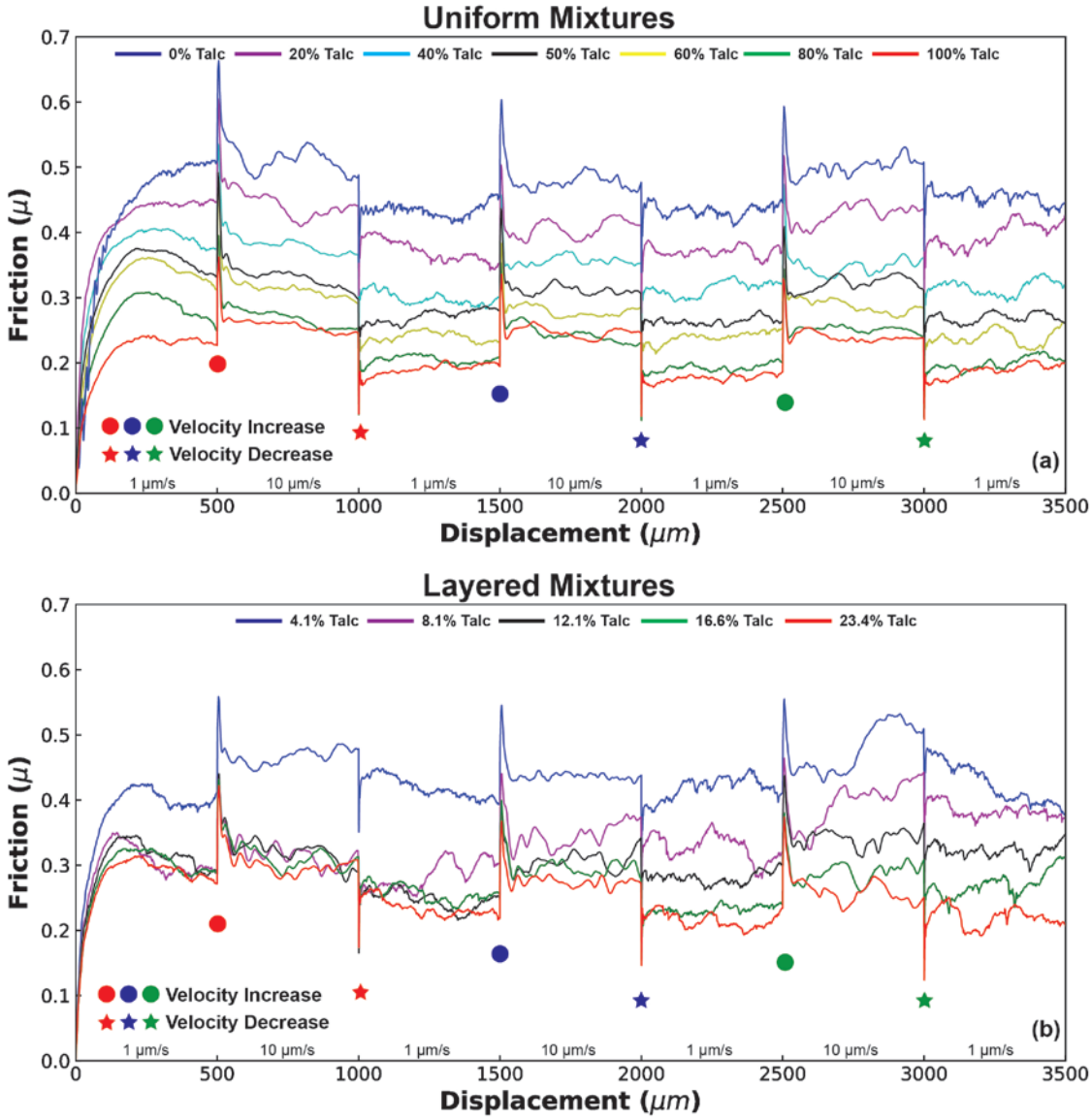

Figure 2-3. (a) Friction evolution of representative uniform talc-quartz mixtures, i.e., 0%, 20%, 40%, 50%, 60%, 80%, and 100% talc-quartz mixtures. (b) Friction evolution of layered mixtures, i.e., 4.1%, 8.1%, 12.1%, 16.6%, and 23.4% talc in terms of weight percentage.

The friction coefficient of uniform mixtures after a shear displacement of 500 μm is summarized in **Figure 2-4**. It is clearly observed that an increase in talc content results in a reduction in shear strength. With 50% talc, the friction coefficient of the mixture is

reduced from ~0.52 to ~0.34, from that of 100% quartz. The weakening continues with >50% talc.

The frictional evolution of a layered mixture is also shown in **Figure 2-4**. The friction coefficient decreases with an increase in talc layer thickness. Specifically, friction decreases from ~0.52 to <0.3 with ~8% of talc (relative layer thickness of 5-particles) present in the mixture. This trend is consistent with previous laboratory observations (Niemeijer et al., 2010) and 2D simulation results using DEM (Wang et al., 2017).

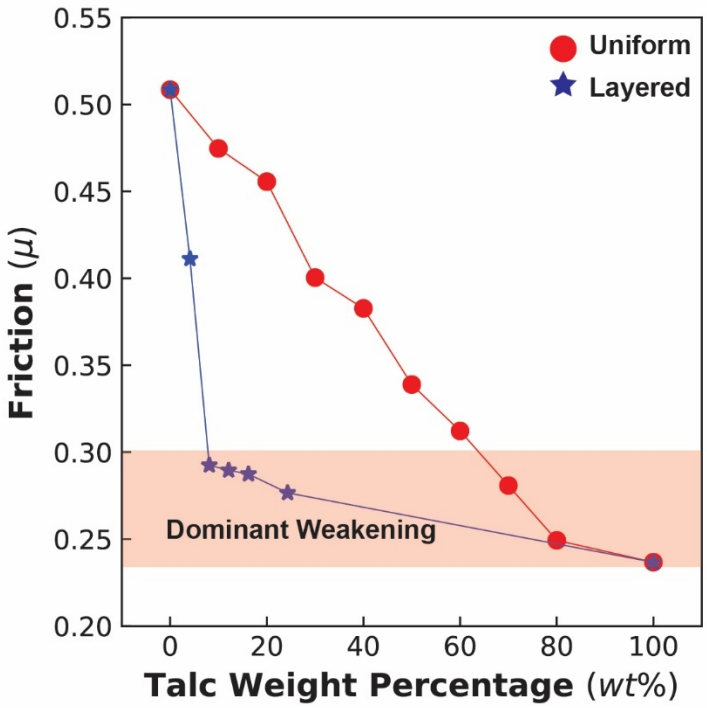

Figure 2-4. Friction coefficient after 500 μm of shear displacement. Significant weakening in the uniform mixture happens at >50% talc, while ~8 wt% of talc can induce similar weakening effect in the layered mixtures.

4.2 Evolution of slip stability

Previous laboratory observations suggest that talc can affect the slip stability of faults comprising a strong tectosilicate matrix. Specifically, the presence of talc can increase the value of the stability parameter $(a - b)$ with increasing weight percentage. Gouge mixtures of quartz and talc show a transition from velocity weakening to velocity strengthening at 25-50 wt% talc; calcite and talc mixtures show mainly velocity strengthening behavior (Giorgetti et al., 2015; Moore and Lockner, 2011). This strong influence of talc on behavior has been simulated using 2D DEM modeling (Wang et al., 2017). In this study, we conduct velocity stepping simulations on quartz and talc mixtures using a modified slip-weakening constitutive law.

Zooming into friction evolution at each velocity step enables the analysis of stability parameters, i.e., $(a - b)$ values. The friction evolution of each velocity step is best fitted by a rate and state friction law using a iterative Levenberg-Marquardt (L-M) algorithm (Press et al., 1987). In the fitting process, a set of initial guesses for a and b values are made. The L-M algorithm then searches from a range of 0.001 to 1000 times the initial estimations. The algorithm fits the evolution curve by solving the rate and state friction law using a 4th order Runge-Kutta algorithm (Press et al., 1987). The algorithm converges at conditions where both the difference between the previous and current trial parameter or Chi square of the fitted data is sufficiently small. **Figure 2-5**(a) and (b) show the fitted $(a - b)$ values analyzed from uniform mixtures and layered mixtures respectively.

Figure 2-5(a) and 5(b) shows the summarized plot of $(a-b)$ values of corresponding velocity steps marked in **Figure 2-3**, as well as trendlines of $(a-b)$ values from the same velocity steps from different simulations. The value of $(a-b)$ are mostly positive in both uniform and layered mixtures. The positive slopes of $(a-b)$ trendlines suggest that, in uniform mixtures, an increase in talc content can increase the $(a-b)$ value, with the exception of the first velocity-increase step (negative slope). The exception could be explained by the bulk gouge not reaching steady state after 500 μm of initial shear displacement. The $(a-b)$ values do not show apparaent trends with increasing thickness of talc layer, suggesting by scattered data and trendline slopes.

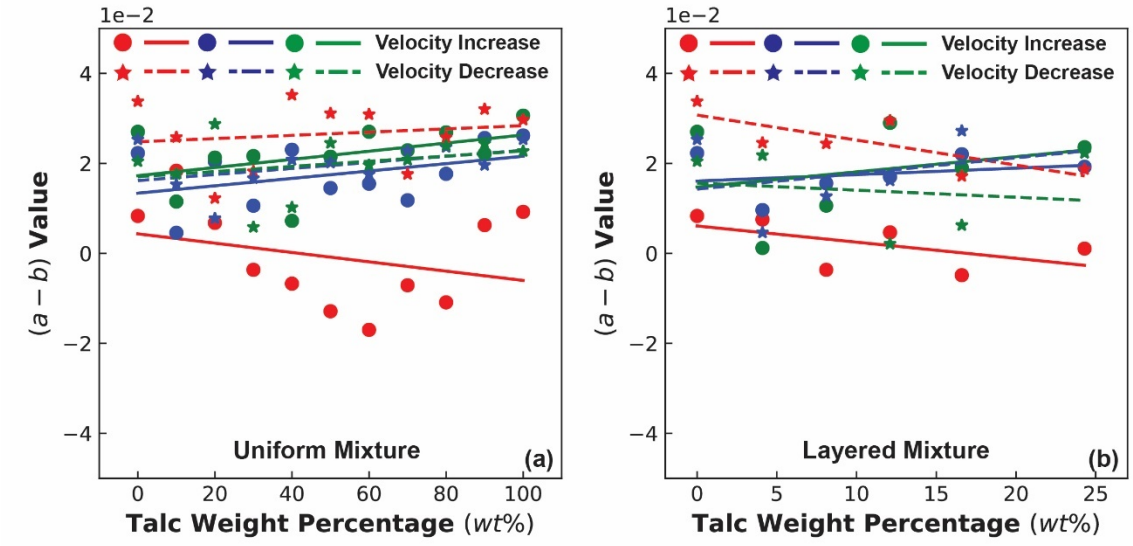

Figure 2-5. (a) $(a-b)$ of uniform mixture plotted against talc weight percentage; (b) $(a-b)$ of layered mixture plotted against talc weight percentage., the markers correspond to the velocity steps shown in Figure 2-3.

4.3 Evolution of layer thickness, coordination number, and local permeability

The permeability of reactivated faults will evolve as the fault slips. The permeability of fault gouge is related to the evolution of layer thickness and porosity (Samuelson et al., 2009). We represent the overall evolution of the layer thickness by monitoring the dilation of gouge during the experiment. Local permeability evolution is also determined from local changes in porosity recorded during shear. The original and corrected sample layer thicknesses of 10% and 90% uniform talc-quartz mixtures are shown in **Figures 2-6**(a) and (b), respectively. Geometric thinning is evaluated by compensating the gouge volume engaged in shear by the extruded volume of gouge at the two ends of the platens. Long-term shear dilation is observed in both cases. Specifically, the 10% talc-quartz mixture shows a faster dilation during 10 $\mu m/s$ velocity step and a slower dilation during 1 $\mu m/s$ velocity step. The 90% talc-quartz mixture shows apparent compaction at 1 $\mu m/s$ velocity steps, i.e., when velocity drops from 10 $\mu m/s$ to 1 $\mu m/s$, but the compaction halts shortly, followed by a slow dilation until the next velocity step.

The local permeability of the 10% and 90% talc quartz mixture is shown in **Figure 2-6**(c). The 10% talc-quartz mixture shows an initial increase in local permeability, followed by a sharp decrease at ~2000 μm of shear displacement, and continues to slowly level off afterwards. The 90% talc-quartz mixture shows a sharp decrease in local permeability at ~1000 μm of shear displacement, and stabilizes after ~2000 μm. In both cases, the local permeability decreases after a velocity drop but may slightly recover before the next change in velocity, suggesting a maturation of a localization zone. However, this behavior is not apparent before ~1000 μm and ~2000 μm of shear offset for 90% and 10%

talc-quartz mixtures, respectively, suggesting that higher content of talc may accelerate the development of shear localization zone.

The average coordination numbers (the average number of active contacts around each particle) of the 10% and 90% talc-quartz mixtures are shown in **Figure 2-6**(d). Both cases show an overall decrease in coordination number with shear offset, which is consistent with the observation of long-term dilation. 10% talc-quartz mixture shows significantly lower average coordination number than 90% talc-quartz, indicating a less dense packing. In the case of the 90% talc-quartz mixture, the average coordination number increases with a velocity decrease, with the converse behavior observed for the 10% talc-quartz mixture. These observed behaviors can be viewed as the additive effect of compaction, dilation, and self-rearrangement. Quartz exhibits a higher shear strength, contact rolling resistance, incapable of rapid rearrangement, suggesting by the negligible compaction after a velocity drop (**Figure 2-6**(a)). Talc exhibits significantly smaller contact friction and thus may self-rearrange rapidly - reflected in the slight dilation (decrease in coordination number) promoted by a velocity increase and rapid compaction (increase in coordination number) caused by a velocity decrease. Given the non-periodic model configuration, the extruded particles at the two ends features less dense packing than the effective shear zone in the quartz-rich mixtures, however, they feature similar packing as the shear zone in the talc-rich mixtures. Higher shear velocity may promote self-rearrangement of the quartz-rich gouge in the non-periodic system, thus increasing coordination number during velocity increases. This observed rate of self-rearrangement is also suspect to be related to normal stress, i.e., higher normal stress may reduce the effect

of self-rearrangement thus neutralizing the difference of velocity-dependent compaction and dilation behavior between talc-rich and quartz-rich gouge.

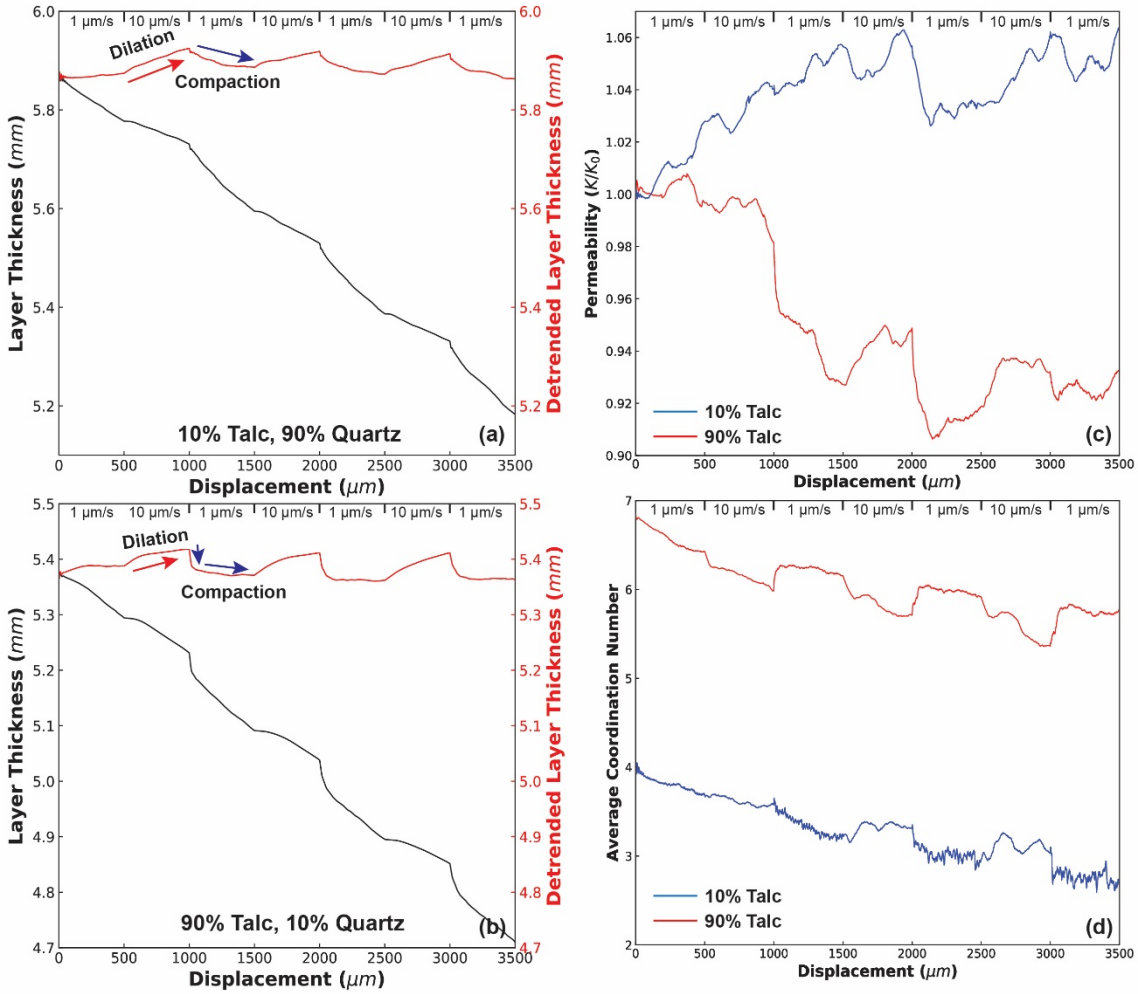

Figure 2-6. Uncorrected/corrected evolution of sample layer thickness with shear displacement for (a) 10% talc-quartz mixture, (b) 90% talc-quartz mixture. (c) Local normalized permeability evolution of 10% and 90% talc-quartz mixtures estimated from local porosity evolution. (d) Evolution of average coordination number of 10% and 90% talc-quartz mixtures.

5. Discussion

5.1 Shear Localization and permeability evolution

Uniform mixtures of quartz and talc show a linear trend of weakening while layered mixtures show a non-linear (exponential) trend in our simulation results. In laboratory experiments, dominant weakening of talc is commonly observed. Our observation of uniform mixtures matches previous laboratory observation (Moore and Lockner, 2011) but contradicts the other laboratory observations of dominant weakening at ~25% talc in uniform mixtures (Giorgetti et al., 2015), and 2D simulation results using a similar DEM setup (Wang et al., 2017). However, the dominant weakening trend of layered mixtures in our simulation matches laboratory observations very well (Niemeijer et al., 2010). In a granular gouge system, the transient shear strength is determined by ensemble strength of force chains formed during shear, weak patches can reduce the amount of effective strong force chains or hinder strong force chains to form. Talc particles feature much lower surface friction and elastic contact stiffness than quartz particles thus acting as a weak patch in the quartz matrix by connecting quartz particles as shown in **Figure 2-7**(a). The weakening behavior of quartz-talc mixtures is believed to be caused by the connection of weak talc patches in the uniform mixtures and shear localization in the layered mixtures. Introducing more talc by weight increases the number of weak patches as well as their affected areas. Weak patches are often preferentially self-relocated along the shear zone after a certain amount of shearing. The weakening effect can be largely enhanced if the weak particles (patches) are pre-imposed as a through-going layer in the gouge, forming a

connected weak zone as shown in **Figure 2-7**(b). The weak zone prevents the formation of stronger force chains, reduces the ensemble shear strength significantly.

Figures 2-7(c) and (d) show the filtered contact friction map of the uniform mixture and layered mixture at a shear displacement of 3000 μm, at the end of a velocity increase. Weak contacts with friction in the range 0.106 to 0.100 (according to the slip-weakening law introduced in section 2.1) are plotted, representing the evolved contacts in the assembly where the majority of shear displacement is accommodated. Strong contacts with friction coefficient outside of the range (0.1 to 0.106) are not shown (filtered). It can be clearly observed that these contacts are mainly distributed in the Riedel-shear direction in the uniform mixtures.

In layered mixtures, the weak talc patches are naturally connected and are pre-imposed as a through-going layer, resulting in strong weakening and localization. In this configuration, the talc layer transects the gouge and prevents these mechanically-isolated quartz particles from forming strong force chains, creating a barrier effect. However, when the talc layer is relatively thin, some quartz particles penetrate the talc layer and form continuous force chains across the horizontal transect and between shear platens. Increasing talc layer thickness enhances the barrier effect obviating the penetration of quartz across the talc. Therefore, the observation of a strong weakening effect with an increase in the thickness of the talc layer is rational. The force chains are truncated mostly at the boundary of the talc layer. **Figure 2-8** shows the assembly at a shear displacement of 3500 μm with talc weight percentages of 4.1%, 8.1%, 12.1%, 16.6%, and 24.3% (these weight percentages correspond to the relative talc layer thickness of 1-particle, 3-particles,

5-particles, 8-particles, and 10-particles, respectively). Penetration of quartz through the talc layer is clearly decreased as the increase in talc layer thickness (**Figure 2-8**(a) through 8(e)). A major increase in shear localization is observed between 4.1% talc and 8.1% talc, suggested by the strong weakening effect (large drop in friction shown in **Figure 2-4**), minor differences are observed with even greater talc layer thicknesses, indicating a dominate effect.

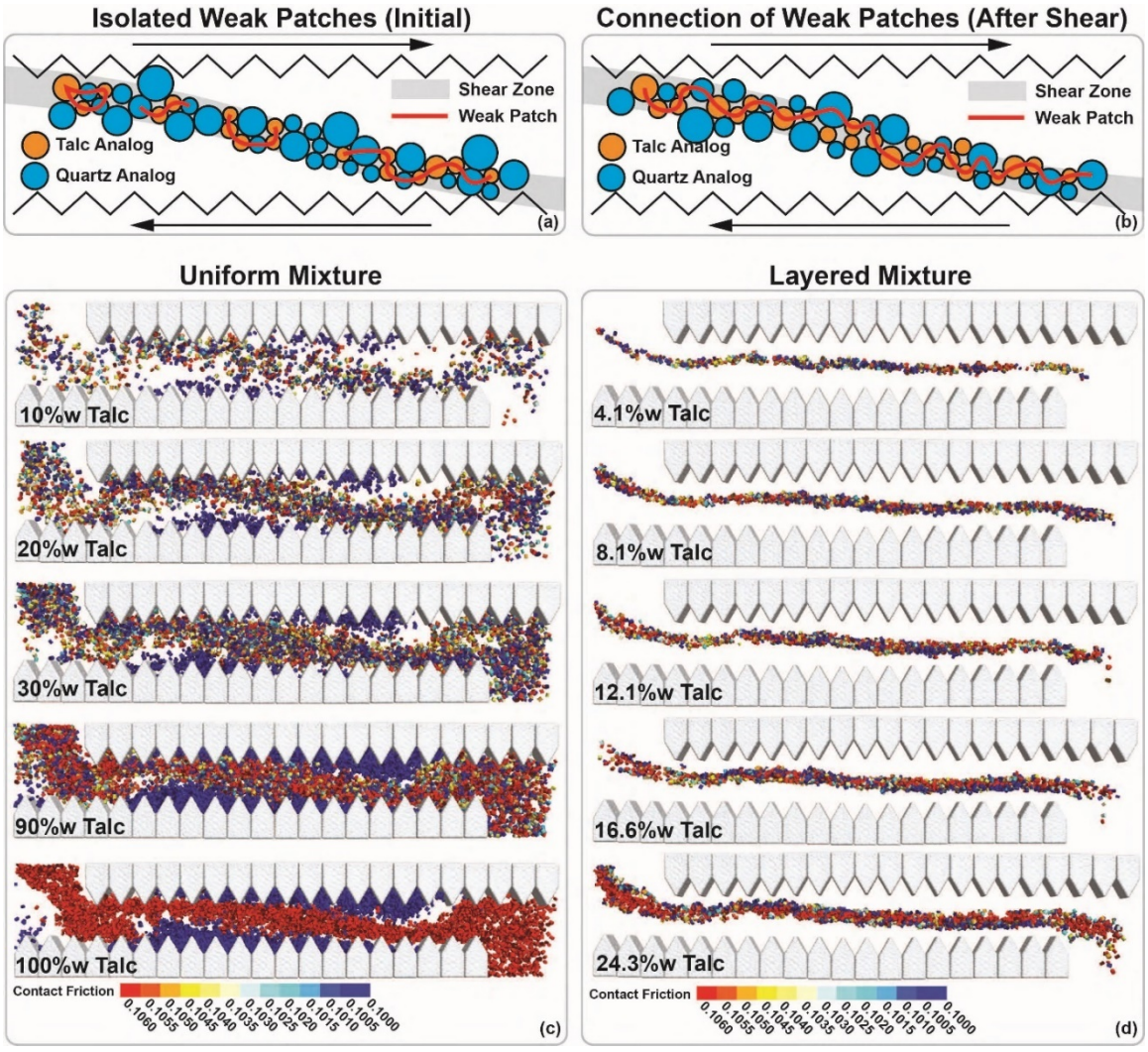

Figure 2-7. (a) Schematic of weak patches formed by talc. (b) Schematic of weak patches preferentially self-rearranged into a shear zone after a given shear displacement. (c) Evolved weak

contacts in a uniform mixture oriented along the R-shear direction. (d) Evolved weak contacts in layered mixture only appear in the talc layer, indicating strong localization.

The volume and interconnectivity of pore volume are linked directly to the permeability of porous media. Porosity is often measured as a proxy for permeability although requires scaling against a necessary length dimension. In this study, the permeability of the gouge is estimated from porosity measured in seven (spherical) sampling windows, spaced along the shear zone, overlapping with the localization zone. The evolution of porosity during dynamic shear in the localization zone accounts for the permeability evolution. We have shown a distinct difference in permeability evolution between the 90% talc (talc-rich) gouge and 10% talc (quartz-rich) gouge mixtures (**Figure 2-6**(c)). Specifically, permeability decreases with talc-rich gouge while increases with quartz-rich gouge. This distinct behavior is plausibly caused by different elastic properties and frictional resistance of quartz and talc contacts. Contacts between quartz grains feature much higher contact stiffness and friction than talc, indicating a large potential for shear dilation rather than shear compaction during shear. Contacts between talc grains, or contacts between talc and quartz grains are weakened by talc, in terms of both elastic properties and friction. Therefore, these contacts are less prone to shear dilation, exhibiting shear compaction, thus destroying permeability. Notably, once the gouge accumulates a certain amount of shear displacement (~2000 μm in this study), the overall local porosity stabilizes, implying an overall steady-state permeability, and a maturation of shear localization. In nature, talc grains are platy, deformable, and featuring a tendency towards self-organization to align with the shear localization direction. These features increase the

number of weakened contacts, therefore enhancing the weakening effect and shear compactive nature of talc.

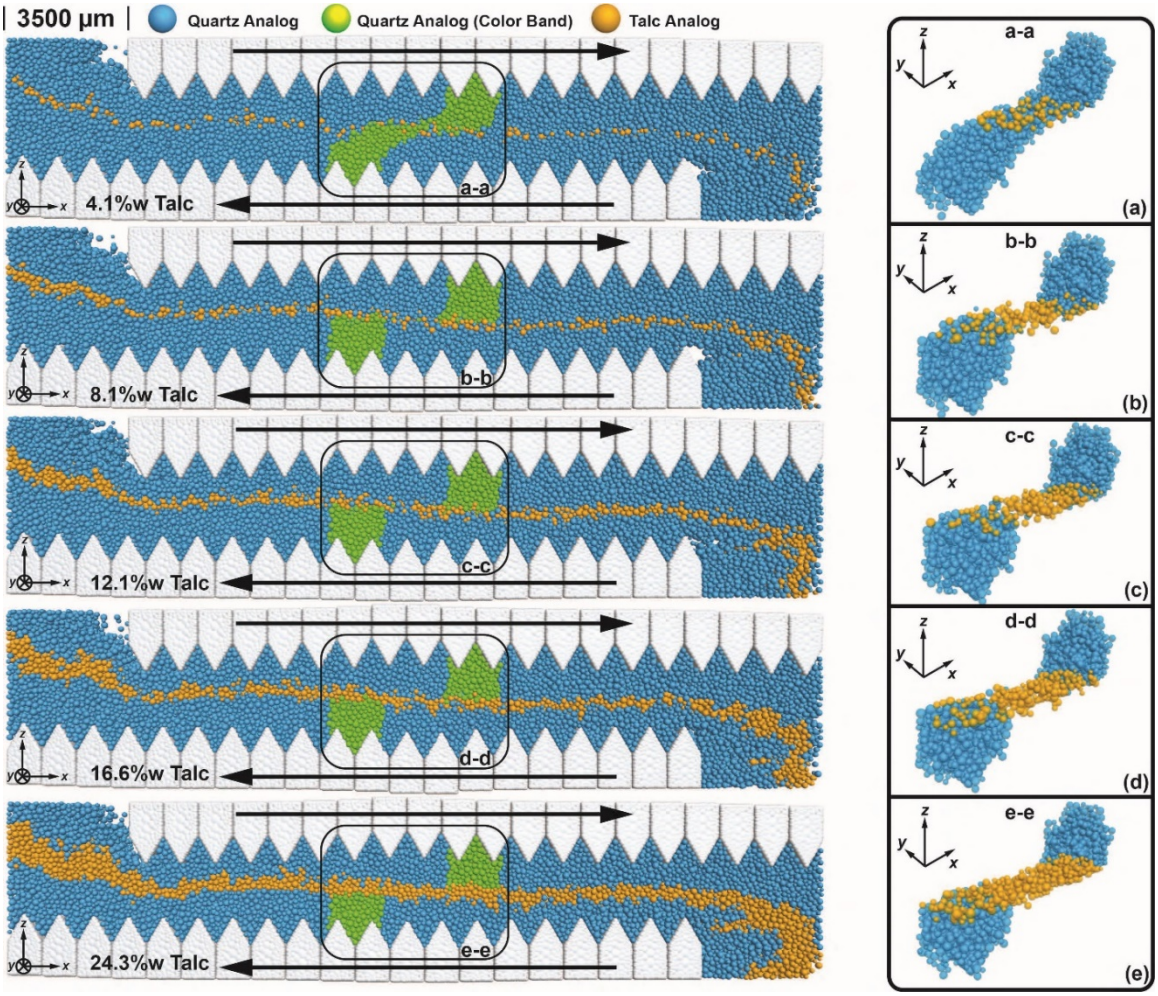

Figure 2-8. Localization of shear deformation in a layered mixture. The green band shows the deformation pattern of the gouge for different talc layer thicknesses. Penetration of quartz through the talc layer is reduced by increased talc layer thickness. A major difference in shear localization are observed between 4.1% talc and 8.1% talc, as a strong weakening effect is observed, however, minor differences are observed greater talc layer thicknesses.

5.2 Modeling of stability parameters

The DEM modeling of enhance of shear stability (increase in $(a-b)$ values) with an increasing proportion of talc matches well with previous studies. However, the stability parameters (a and b) applied to the analog minerals in this study are approximately one order-of-magnitude larger than laboratory measured values and are always positive. Previous laboratory studies suggest that phyllosilicates feature negative b values, which is presumably due to the platy particle shape (Giorgetti et al., 2015). In the DEM model, spherical particles are implemented to conduct the simulations. The spherical grain shape could result in greater geometric dilation and produce increased numerical noise as shear strength evolves. This numerical noise would mask the evolution in instability and hinder the direct assignment of lab-measured stability parameters. 3D DEM simulations are often computational expensive, which takes significant amount of real-time in computing. In our simulation, a density scaling factor of 10^{12} has been implemented to reduce the computational time to a feasible range (around 24 hours on current hardware), reduce the density scaling factor by two magnitudes will result in one magnitude increase in the computational time. Density scaling may induce additional inertial effect on velocity change events which can affect the magnitude of $(a-b)$ values, i.e., large density scaling factor can increase the value of a. We use density scaling and exaggerated a and b values to, first, unmask the stability behavior from the numerical noise. The scaling-up of stability parameters a and b improves the resolution of the instantaneous response to velocity change during dynamic shear with velocity steps. Second, we focus on defining the transition in slip stability behavior, i.e., exploring the evolution trends of $(a-b)$. Large

magnitude of the selected stability parameters and density scaling would not presumably influence the evolution trend of stability parameters against the gouge composition. Third, the precise reproduction of rate and state response using DEM remains a major challenge, and is beyond the principal foci of this study. Nevertheless, this study provides useful insights in approaching the problem *via* appropriate simplifications.

5.3 Effect of grain size and grain shape

A rolling resistance mechanism is implemented at particle contacts to mimic grain angularity and interlocking. Previous simulation studies have considered grain angularity, anisotropy, local rate and state friction, and grain deformation (Abe and Mair, 2009; Guo and Morgan, 2004; Kim et al., 2016; Mair et al., 2002). However, these physical features and mechanisms are never combined into a single numerical model, as doing so makes the model overly complicated and computationally expensive. In this study, we specifically explore the evolution of shear strength, slip stability, and permeability of quartz and talc analog mixtures. Nonetheless, grain size and grain shape no doubt play a key role in determining the resolution of the simulation and the transitional behavior of the mixture. Reducing particle size can improve the resolution of shear strength evolution (Wang et al., 2017), however, a smaller grain size necessarily increases of the number of particles in the assembly – this is especially true in 3D space, resulting in increased computational cost. We manage to achieve a balance between the choice of grain size, computational cost, and resolution of the simulation.

The drawback of spherical particles, in allowing unfettered rolling, is well understood but can be countered by adding rolling resistance to the particle contact. The aspect of quartz particles generally ranges from near spherical to angular, and that of talc is platy. These are the key microscopic features which dictate distinct frictional properties. Platy talc particles would be anticipated to form increased contacts with quartz particles, with this, coupled with its high deformability, providing the potential to create large weakening areas. It was found that the microscopic weakening mechanism for talc mixtures is related to the deformation and self-reorientation of the platy particles, as well as strong mineral particles tends to slide along the plate interfaces of talc particles in an angular grain matrix, forming localized weak patches. These weak patches are self-organizing and localized in the shear zone to further weaken the bulk gouge during shear (Giorgetti et al., 2015). The weakening mechanism applies to both uniform and layered mixture. However, certain amount of shear strain is required in uniform mixtures for talc to form a shear localization, while the localization has already been imposed in layered mixtures. The numerical simulations in this study are compared to previous laboratory data in **Figure 2-9**. The numerical results of uniform mixtures in this study differ by ~10 to ~20% in terms of the transition from dominantly frictionally-strong dominantly to frictionally-weak, resulting from the spherically-shaped grains in the model. However, the weakening effect of a pre-imposed localization (layered mixtures) shown by our simulation is mechanistically similar to that of laboratory results, due to the fact that platy talc particles promotes localization in uniform mixtures by forming through-going talc-rich layers. Full implementation of platy grains with appropriate high deformability could be achieved in a

future study. Nonetheless, we argue that our simulation results show an overall creditable match with previous laboratory and simulation results, especially for the layered mixture configuration (Niemeijer et al., 2010), which is most likely to appear in nature.

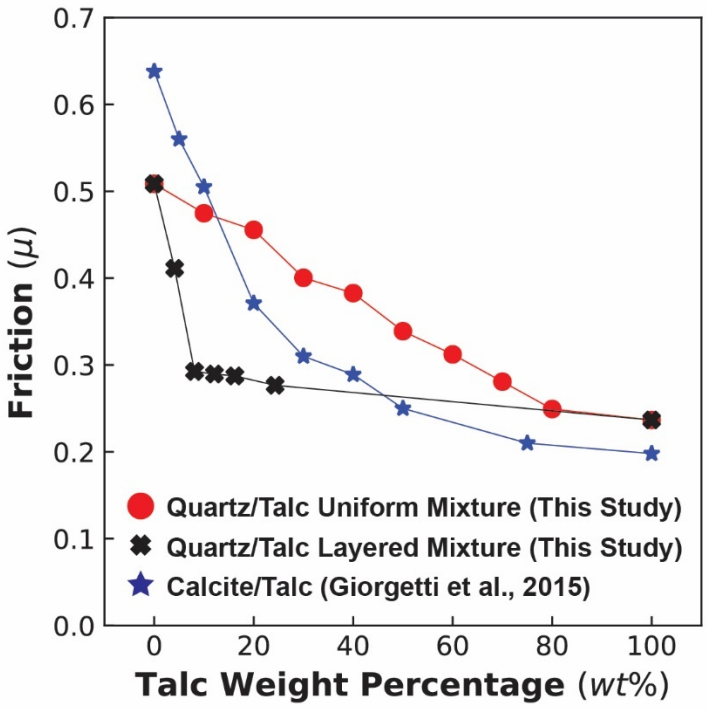

Figure 2-9. Comparison of weakening effect of talc explored in this study relative to previous laboratory results using calcite-talc mixtures (Giorgetti et al., 2015). Data replotted from original paper.

5.4 Comparison of 3D and 2D response

The effect of problem dimensionality on the shear strength of gouge has been studied both in the laboratory and in numerical simulations. In laboratory studies, metal rods were used to represent the 2D configuration (Knuth and Marone, 2007) and behavior

was compared to experiments using glass beads (3D). 2D materials have a high potential for dilation and compaction, creating large fluctuations in shear strength during shear evolution. Additionally, due to the strong tendency for the rolling of rods, the friction coefficient in the 2D configuration is reduced (maximum of ~0.35). Numerical studies of 2D direct shear on gouge (Morgan and Boettcher, 1999; Wang et al., 2017a) indicate similar friction evolution and fluctuation to laboratory results on metal rods. Realistic magnitudes of friction can only be reproduced by fully restraining the rotation of particles. We compare the resolution of friction evolution from previous 2D simulation with particle rotation disabled (Wang et al., 2017) and 3D simulation in this study. **Figure 2-10**(a) and 10(b) show the simulated evolution of friction of 100% analog quartz in both 2D and 3D configurations where model parameters are consistent. A significant reduction in fluctuations is observed in the 3D evolution. The direct effect and evolution effect of rate and state friction are independently apparent in 3D but are almost masked in 2D.

In terms of reducing fluctuations in shear strength evolution, the additional dimension and related extra displacement-degree-of-freedom in 3D reduces the strong dilation effect apparent in 2D. For example, particles that need to override other particles to rearrange in 2D, are able to move both obliquely and sideways in 3D. This 3D rearrangement in our numerical model better accommodates the natural rearrangement of gouge grains during shear.

3D numerical simulations also show an improved representation of the direct and evolution effects described by rate and state friction. This is plausibly due to the increase in the number of contacts in the 3D configuration. The average coordination number is

nearly double that in 2D. This indicates that more contacts are evolving during a velocity step, resulting in a crispier resolution.

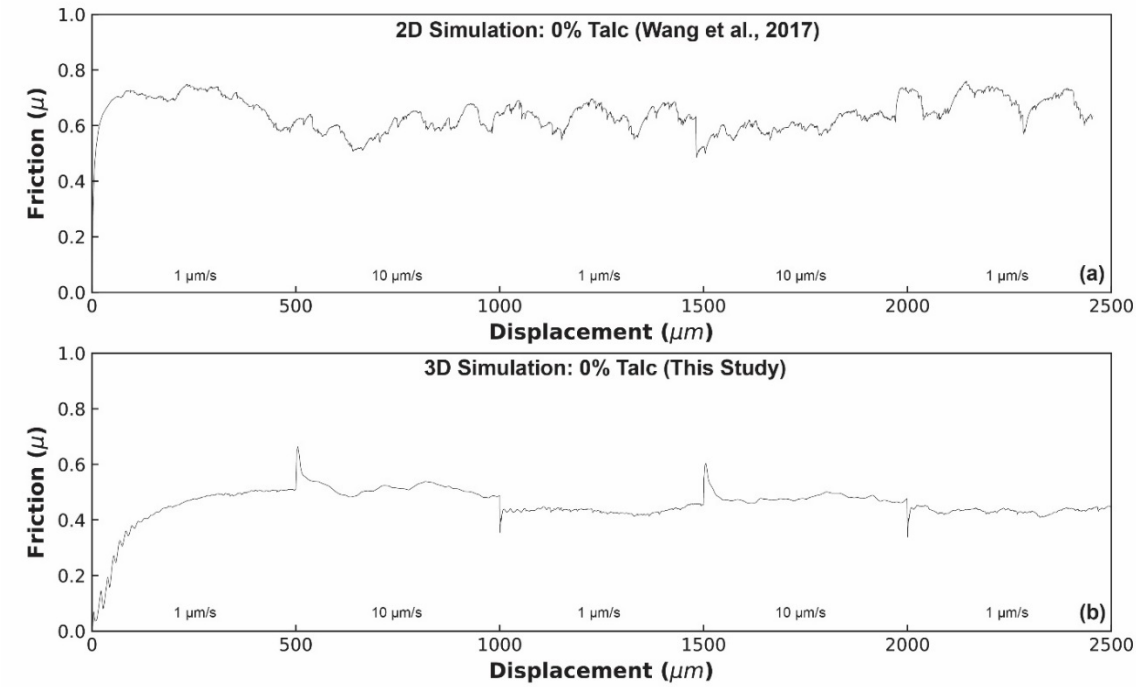

Figure 2-10. Comparison of 2D and 3D simulations: (a) 2D friction evolution of 0% talc under dynamic shear (Wang et al., 2017); (b) 3D friction evolution of 0% talc under dynamic shear (this study).

6. Conclusions

In this study, we explore the shear strength, slip stability, and permeability of analog quartz and talc mixtures *via* 3D discrete element modeling. Specifically, configurations of both uniform and layered mixtures with various talc: quartz weight proportions are examined. We perform numerical direct shear tests with velocity stepping

on the sample mixtures and capture the evolution of shear strength, slip stability, and permeability. We conclude the following based on the observed results:

1. Simulations show strong weakening effects in uniform mixtures of talc; a linear weakening effect is observed due to the limitation of particle shape - in this case restricted to spherical. A dominant weakening effect is observed for layered talc. A mixture with ~8% talc can induce an ~50% reduction in shear strength.
2. Increased talc content can enhance the stability of uniform mixtures by increasing $(a - b)$ values, however, increasing talc layer thickness in layered mixtures shows no apparent influence on the stability behavior.
3. In uniform mixtures, permeability increases in the shear localization zone with more quartz present, while decreases with more talc. Permeability evolves to a steady state, and is enhanced with velocity up-steps while suppressed with down-steps after the maturation of shear localization.
4. Dimensionality can greatly impact the resolution of the dynamic response of gouge mixtures during shear. The friction evolution during a velocity change can be clearly observed in 3D simulations which are largely obscured in 2D models.

The results fit previous laboratory observations while some slight mismatches are also noticed. These inaccuracies can be related to the idealized particle shape and size distribution, simplified to spherical in these mixtures. Future research of full implementation of realistic particle shape and deformable grains need to be achieved to better simulated the behavior of faults during shear. Nonetheless, our work shows an alternative way of exploring the rheological properties of faults during dynamic shear.

References

Abe, S., & Mair, K. (2009). Effects of gouge fragment shape on fault friction: New 3D modelling results. *Geophysical Research Letters*, *36*(23), 2–5. https://doi.org/10.1029/2009GL040684

Abe, S., Dieterich, J. H., Mora, P., & Place, D. (2002). Simulation of the influence of rate- and state-dependent friction on the macroscopic behavior of complex fault zones with the lattice solid model. *Pure and Applied Geophysics*, *159*(9), 1967–1983. https://doi.org/10.1007/s00024-002-8718-7

Abe, S., van Gent, H., & Urai, J. L. (2011). DEM simulation of normal faults in cohesive materials. *Tectonophysics*, *512*(1–4), 12–21. https://doi.org/10.1016/j.tecto.2011.09.008

Ai, J., Chen, J. F., Rotter, J. M., & Ooi, J. Y. (2011). Assessment of rolling resistance models in discrete element simulations. *Powder Technology*, *206*(3), 269–282. https://doi.org/10.1016/j.powtec.2010.09.030

Anthony, J. L., & Marone, C. (2005). Influence of particle characteristics on granular friction. *Journal of Geophysical Research B: Solid Earth*, *110*(8), 1–14. https://doi.org/10.1029/2004JB003399

Collettini, C., & Holdsworth, R. E. (2004). Fault zone weakening and character of slip along low-angle normal faults: insights from the Zuccale fault, Elba, Italy. *Journal of the Geological Society*, *161*(6), 1039–1051. https://doi.org/10.1144/0016-764903-179

Cundall, P. A., & Strack, O. D. L. (1979). A discrete numerical model for granular assemblies. *Géotechnique*. https://doi.org/10.1680/geot.1979.29.1.47

D'Orazio, M., Boschi, C., & Brunelli, D. (2004). Talc-rich hydrothermal rocks from the St. Paul and Conrad fracture zones in the Atlantic Ocean. *European Journal of Mineralogy*, *16*(1), 73–83. https://doi.org/10.1127/0935-1221/2004/0016-0073

Dieterich, J. H. (1979). Modeling of rock friction 1. Experimental results and constitutive equations. *Journal of Geophysical Research: Solid Earth*, *84*(B5), 2161–2168. https://doi.org/10.1029/JB084iB05p02161

Dieterich, J. H. (1992). Earthquake nucleation on faults with rate-and state-dependent strength. *Tectonophysics*, *211*(1–4), 115–134. https://doi.org/10.1016/0040-1951(92)90055-B

Escartín, J., Andreani, M., Hirth, G., & Evans, B. (2008). Relationships between the microstructural evolution and the rheology of talc at elevated pressures and temperatures. *Earth and Planetary Science Letters*, *268*(3–4), 463–475. https://doi.org/10.1016/j.epsl.2008.02.004

Fang, Y., den Hartog, S. A. M., Elsworth, D., Marone, C., & Cladouhos, T. (2014). Anomalous distribution of microearthquakes in the Newberry Geothermal Reservoir: Mechanisms and implications. *Geothermics*, *63*, 62–73. https://doi.org/10.1016/j.geothermics.2015.04.005

Faulkner, D. R., Lewis, A. C., & Rutter, E. H. (2003). On the internal structure and mechanics of large strike-slip fault zones: Field observations of the Carboneras fault in southeastern Spain. *Tectonophysics*, *367*(3–4), 235–251. https://doi.org/10.1016/S0040-1951(03)00134-3

Faulkner, D. R., Jackson, C. A. L., Lunn, R. J., Schlische, R. W., Shipton, Z. K., Wibberley, C. A. J., & Withjack, M. O. (2010). A review of recent developments concerning the structure, mechanics and fluid flow properties of fault zones. *Journal of Structural Geology*, *32*(11), 1557–1575. https://doi.org/10.1016/j.jsg.2010.06.009

Ferdowsi, B., Griffa, M., Guyer, R. A., Johnson, P. A., Marone, C., & Carmeliet, J. (2014). Three-dimensional discrete element modeling of triggered slip in sheared granular media. *Physical Review E - Statistical, Nonlinear, and Soft Matter Physics*, *89*(4), 1–12. https://doi.org/10.1103/PhysRevE.89.042204

Giorgetti, C., Carpenter, B. M., & Collettini, C. (2015). Frictional behavior of talc-calcite mixtures. *Journal of Geophysical Research B: Solid Earth*, *120*(9), 6614–6633. https://doi.org/10.1002/2015JB011970

Grasemann, B., & Tschegg, C. (2012). Localization of deformation triggered by chemo-mechanical feedback processes. *Bulletin of the Geological Society of America*, *124*(5–6), 737–745. https://doi.org/10.1130/B30504.1

Guan, C.-Y., Qi, J.-F., Qiu, N.-S., Zhao, G.-C., Yang, Q., Bai, X.-D., & Wang, C. (2012). Macroscopic Young's Elastic Modulus Model of Particle Packing Rock Layers. *Open Journal of Geology*, *02*(03), 198–202. https://doi.org/10.4236/ojg.2012.23020

Guo, Y., & Morgan, J. K. (2004). Influence of normal stress and grain shape on granular friction: Results of discrete element simulations. *Journal of Geophysical Research B: Solid Earth*, *109*(12), 1–16. https://doi.org/10.1029/2004JB003044

Hazzard, J. F., & Mair, K. (2003). The importance of the third dimension in granular shear. *Geophysical Research Letters*, *30*(13), 41–1. https://doi.org/10.1029/2003GL017534

Ikari, M. J., Marone, C., & Saffer, D. M. (2011). On the relation between fault strength and frictional stability. *Geology*, *39*(1), 83–86. https://doi.org/10.1130/G31416.1

Iwashita, K., & Oda, M. (1998). Rolling Resistance at Contacts in Simulation of Shear Band Development by DEM. *Journal of Engineering Mechanics*, *124*(3), 285–292. https://doi.org/10.1061/(ASCE)0733-9399(1998)124:3(285)

Jiang, M., Shen, Z., & Wang, J. (2015). A novel three-dimensional contact model for granulates incorporating rolling and twisting resistances. *Computers and Geotechnics*, *65*, 147–163. https://doi.org/10.1016/j.compgeo.2014.12.011

Kim, K. Y., Suh, H. S., Yun, T. S., Moon, S.-W., & Seo, Y.-S. (2016). Effect of particle shape on the shear strength of fault gouge. *Geosciences Journal*, *20*(3), 351–359. https://doi.org/10.1007/s12303-015-0051-0

Knuth, M., & Marone, C. (2007). Friction of sheared granular layers: Role of particle dimensionality, surface roughness, and material properties. *Geochemistry, Geophysics, Geosystems*, *8*(3). https://doi.org/10.1029/2006GC001327

Mair, K., & Marone, C. (1999). Friction of simulated fault gouge for a wide range of velocities and normal stresses. *Journal of Geophysical Research: Solid Earth*, *104*(B12), 28899–28914. https://doi.org/10.1029/1999JB900279

Mair, K., Frye, K. M., & Marone, C. (2002). Influence of grain characteristics on the friction of granular shear zones. *Journal of Geophysical Research: Solid Earth*, *107*(B10), ECV 4-1-ECV 4-9. https://doi.org/10.1029/2001JB000516

Marone, C. (1998). Laboratory-Derived Friction Laws and Their Application To Seismic Faulting. *Annual Review of Earth and Planetary Sciences*, *26*(1), 643–696. https://doi.org/10.1146/annurev.earth.26.1.643

Marone, C., Raleigh, C. B., & Scholz, C. H. (1990). Frictional behavior and constitutive modeling of simulated fault gouge. *Journal of Geophysical Research*, *95*(B5), 7007–7025. https://doi.org/10.1029/JB095iB05p07007

Moore, D. E., & Lockner, D. A. (2011). Frictional strengths of talc-serpentine and talc-quartz mixtures. *Journal of Geophysical Research: Solid Earth*, *116*(1), 1–17. https://doi.org/10.1029/2010JB007881

Moore, D. E., & Rymer, M. J. (2007). Talc-bearing serpentinite and the creeping section of the San Andreas fault. *Nature*, *448*(7155), 795–797. https://doi.org/10.1038/nature06064

Morgan, J. K. (1999). Numerical simulations of granular shear zones using the distinct element method: 2. Effects of particle size distribution and interparticle friction on mechanical behavior. *Journal of Geophysical Research*, *104*(B2), 2721. https://doi.org/10.1029/1998JB900055

Morgan, J. K., & Boettcher, M. S. (1999). Numerical simulations of granular shear zones using the distinct element method: 1. Shear zone kinematics and the micromechanics of localization. *Journal of Geophysical Research: Solid Earth*, *104*(B2), 2703–2719. https://doi.org/10.1029/1998JB900056

Niemeijer, A. R., Marone, C., & Elsworth, D. (2010). Fabric induced weakness of tectonic faults. *Geophysical Research Letters*, *37*(3), 1–5. https://doi.org/10.1029/2009GL041689

Peacock, S. M. (1987). Inverted Metamorphic Gradients of New England. *Journal of Geophysical Research*, *92*(B12), 12763–12781. https://doi.org/doi:10.1029/JB092iB12p12763

Press, W., Flannery, B., Teukolsky, S., & Vetterling, W. (1987). Numerical Recipes: The Art of Scientific Computing. *Technometrics*, *29*(4), 501. https://doi.org/10.2307/1269484

Ruina, A. (1983). Slip instability and state variable friction laws. *Journal of Geophysical Research: Solid Earth*. https://doi.org/10.1029/JB088iB12p10359

Samuelson, J., Elsworth, D., & Marone, C. (2009). Shear-induced dilatancy of fluid-saturated faults: Experiment and theory. *Journal of Geophysical Research: Solid Earth*, *114*(12), 1–15. https://doi.org/10.1029/2008JB006273

Samuelson, J., Elsworth, D., & Marone, C. (2011). Influence of dilatancy on the frictional constitutive behavior of a saturated fault zone under a variety of drainage conditions. *Journal of Geophysical Research: Solid Earth*, *116*(10), 1–17. https://doi.org/10.1029/2011JB008556

Scholz, C. H. (1998). Earthquakes and friction laws. *Nature*, *391*(6662), 37–42. https://doi.org/10.1038/34097

Sun, Z., Espinoza, D. N., & Balhoff, M. T. (2016). Discrete element modeling of indentation tests to investigate mechanisms of CO2-related chemomechanical rock alteration. *Journal of Geophysical Research: Solid Earth*, *121*(11), 7867–7881. https://doi.org/10.1002/2016JB013554

Taylor, B., & Huchon, P. (2002). Active continental extension in the western Woodlark Basin: a synthesis of Leg 180 results. *Proceedings of the Ocean Drilling Program, 180 Scientific Results*, *180*(July 2001). https://doi.org/10.2973/odp.proc.sr.180.150.2002

Viti, C., & Collettini, C. (2009). Growth and deformation mechanisms of talc along a natural fault: A micro/ nanostructural investigation. *Contributions to Mineralogy and Petrology*, *158*(4), 529–542. https://doi.org/10.1007/s00410-009-0395-4

Vrolijk, P., & Van Der Pluijm, B. A. (1999). Clay gouge. *Journal of Structural Geology*, *21*(8–9), 1039–1048. https://doi.org/10.1016/S0191-8141(99)00103-0

Wang, C., Elsworth, D., & Fang, Y. (2017). Influence of weakening minerals on ensemble strength and slip stability of faults. *Journal of Geophysical Research: Solid Earth*, *122*(9), 7090–7110. https://doi.org/10.1002/2016JB013687

Wensrich, C. M., & Katterfeld, A. (2012). Rolling friction as a technique for modelling particle shape in DEM. *Powder Technology*, *217*, 409–417. https://doi.org/10.1016/j.powtec.2011.10.057

Wintsch, R. P., Christoffersen, R., & Kronenberg, A. K. (1995). Fluid-rock reaction weakening of fault zones. *Journal of Geophysical Research: Solid Earth*, *100*(B7), 13021–13032. https://doi.org/10.1029/94JB02622

Chapter 3

The Influence of CO2-transformed Iron Oxide Grain Coatings on the Rheological and Transport Behaviors of Faults

Abstract

Fugitive emissions of CO_2 along faults may significantly influence their rheology and permeability by altering cementation and transforming gouge components. We conduct laboratory double direct shear experiments on pristine hematite-, and CO_2-transformed goethite-coated quartz gouge to investigate the evolution of shear strength, slip stability and permeability. The gouge samples are synthesized in the laboratory and are characterized by particle size distribution and through SEM imaging both before and after shear-permeability experiments. Shear strength (at 3 MPa), a-b stability values, frictional healing and creep rates and (fault parallel) permeability are measured in velocity-stepping and slide-hold-slide loading modes. Hematite-coated quartz exhibit the highest peak shear strength, followed by goethite- then un-coated quartz. Coated and un-coated gouge samples exhibit similar residual shear strength. Hematite-coated quartz may undergo potential seismic slip, suggesting by negative (a-b) values. Goethite-coated quartz shows velocity-strengthening behavior by featuring positive (a-b) values but higher frictional healing rate and creep rate. All samples show an initial increase in permeability followed by a decline. However, goethite-coated samples show much less reduction in permeability than others. Characterization suggests that the liberation, transport and clogging of coating

particles and shear-produced wear products can be the main mechanism for permeability evolution. These observations suggest CO_2-transformed goethite-coated quartz-rich faults feature reduced risk of seismic reactivation, while greater loss of inventory in the long-term containment of CO_2 may be expected.

1 Introduction

Geological carbon sequestration injects carbon dioxide (CO_2) into aquifers or reservoirs. It is a promising technology for removing atmospheric CO_2 while replenishing carbon resources in the Earth's subsurface (Benson & Cole, 2008). However, injecting large volumes of fluid at high rates can disturb the subsurface stress field, creating fractures, reactivating pre-existing fractures and faults, and causing unfavorable consequences of gas breaching, loss in inventory, and induced seismicity (Ellsworth, 2013; Elsworth et al., 2016; Guglielmi et al., 2015; Zoback & Gorelick, 2012). Additionally, CO_2 is chemically active, thus may alter the mineralogy of pre-existing rocks and faults, inducing mechanical weakening effects (Altman et al., 2014a, 2014b; Rinehart et al., 2016; Wang, Elsworth, Fang, et al., 2017). CO_2-bleached sandstone samples retrieved from an analog CO_2 reservoir (near Crystal Geyser, Utah) shows significantly lower fracture toughness relative to the unaltered sandstone (Major et al., 2014). Characterization of these samples indicates the presence of hematite as quartz grain coating in the intact samples that is transformed to goethite by CO_2-bleaching - and may be the cause of this weakening.

Iron oxides are the most common products of weathering by geochemical processes, with Goethite ($\alpha - FeOOH$) being the most abundant (Cornell & Schwertmann,

2003). Hematite, however, is a more mature and stable iron oxide which can be commonly found in soils and sandstones in regions with higher temperatures and water activities. Geological alteration of Goethite into hematite in soils has been previously reported (Schwertmann, 1971). Natural hematite and Goethite are poorly crystalized, with small crystalline size ranging from sub-microns to microns; they can typically form Fe^{2+}-O-Si bonds with silica in acidic environments, forming an iron oxide coating layer on the quartz grains. These coating iron oxides, hematite and Goethite in particular, serve an important role in characterizing the mechanical properties of hosting rocks. For example, one previous study (Cundy & Hopkinson, 2005) suggests the precipitation of iron oxides can enhance the undrained shear strength of soil. Since quantifying the influences of iron oxide coating materials are challenging, previous studies intentionally remove iron oxide coatings using strong reductants (Rao et al., 1995). Other studies investigate the influence of iron oxide coatings on the shear strength of sand using lab synthesized hematite and Goethite coated quartz sand (Choo et al., 2015; Larrahondo et al., 2011a; Larrahondo & Burns, 2014). These results indicate that hematite coated sands feature the highest shear strength followed by Goethite-coated sand then uncoated sand. In addition to merely shear strength, slip stability and permeability are two crucial factors that influence the potential for injection-induced seismicity and loss of CO_2 inventory. The potential for this response may be codified through rate and state friction (RSF) laws, that describe the frictional evolution and stability of faults during earthquake cycles (Dieterich, 1978, 1979b, 1979a; Marone, 1998; Rice et al., 2001; Ruina, 1983) and the linkage of RSF to the evolution of

permeability (Fang et al.). For rate state friction, the constitutive relation can be summarized as:

$$\mu = \mu_0 + a \ln\left(\frac{V}{V_0}\right) + b \ln\left(\frac{V_0 \theta}{D_c}\right) \quad (1)$$

in which, μ and μ_0 are the friction coefficients of the current state and previous steady state; V and V_0 are the slip velocity of the current state and previous steady state. V_{lp} is the loading velocity; θ and D_c are the state variable and characteristic slip distance; a and b are the stability parameters.

Reactivation of faults and fractures are common concerns for carbon sequestration, and it is crucial to understand the influencing factors. In particular, most characterizations of concurrent evolution of friction and permeability (Fang et al., 2016; Fang et al., 2017, 2018; Im et al., 2018a; Samuelson et al., 2009; Wang, Elsworth, & Fang, 2017; Yasuhara et al., 2006) ignore the impacts of coatings. To rectify this, we examine key mechanisms implicated in the evolution of friction, stability, and permeability on hematite-, Goethite- and un-coated quartz. These experiments are conducted in a novel double direct shear apparatus within a traditional simple-triaxial pressure vessel and constrained by SEM imaging and particle size measurements.

2 Experimental materials and methods

2.1 Experimental materials

We coat US F-110 (mean particle diameter of 95 μm) fine grain silica sand with hematite and Geothite using the “heterogeneous suspension reaction” method (Scheidegger

et al., 1993). Hematite is purchased in powder form and used as is. Goethite is synthesized by maturing ferrihydrite (prepared from potassium hydroxide and ferric nitrate, PH = 13.6) at 70℃ for 60 hours then air-drying and grinding to fine powder form. To synthesize the iron oxide coated sand, the uncoated sand is wet sieved (#200 sieve) to remove fines, pre-washed by 3% hydrogen peroxide solution (H_2O_2), then air dried. The prepared uncoated sand is mixed and stirred with hematite or Goethite (weight ratio of 25:1) in sodium nitrate solution ($NaNO_3$, 0.01M ionic strength) with a controlled PH of 3.0 (achieved by nitric acid, HNO_3) for 24 hours, resulting in uniformly coated sands (**Figure 3-1**).

2.2 Experimental method and program

We use a miniaturized double direct shear (DDS) configuration similar to the macro-apparatuses reported previously (Collettini et al., 2009; Mair & Marone, 1999; Marone et al., 1990; Marone, 1998). The DDS comprises three loading blocks sandwiching two layers of gouge or intact rock. The normal load (confining stress) is applied to the sides of the blocks with the shear load applied by displacing the center block, perpendicular to the normal loading (**Figure 3-1**). DDS apparatuses are particularly effective in concurrently measuring the evolution of shear strength, slip stability, frictional healing and creep behavior – the elimination of excess moment and spurious rotations yields highly resolved measurements. This DDS configuration may also make highly resolved measurements of friction-permeability on rock coupon surfaces (Im et al., 2017, 2018b) and in slightly different configuration on gouge (this study). In this study, we conduct DDS experiments using novel DDS fluid-flow through platens (**Figure 3-1**(a-a)) inside a

TEMCO simple-triaxial pressure vessel (**Figure 3-1**). These components comprise three steel plates with saw-tooth grooves sandwiching two layers of gouge. The DDS sample is jacketed with normal stress applied and controlled by a single precision pump (A; **Figure 3-1**). A second precision pump (B; **Figure 3-1**) applies shear loading, and a third pump (C; **Figure 3-1**) circulates fluid along the sample in the direction of shear by maintaining a constant upstream pressure (~35kPa). Darcy's law is used to evaluate the permeability of the sample:

$$\kappa = \frac{\mu Q L}{A \Delta p} \tag{2}$$

in which, κ is the permeability parallel to the direction of shear; μ is the dynamic viscosity of the fluid; Q is the monitored flow rate from pump C; A and L are the estimated transient area of flow and length of the flow path, respectively; Δp is the hydraulic pressure difference from upstream and downstream.

Two experiments (layer thicknesses of 2mm and 3mm, for validation purposes) are conducted on each of three sample (hematite-, Goethite- and un-coated) types (**Figure 3-1**(a-a)). Confining stress and upstream hydraulic pressure are maintained at 3 MPa and 35 kPa respectively for all the tests. For each test, the shear loading is applied according to the following stages:

Stage1. **Constant Rate Loading:** Load at constant shear velocity (10 $\mu m/s$) to ~4000 μm shear displacement to reach steady state.

Stage2. **Velocity-Stepping Experiments:** Step shear velocity between 10 $\mu m/s$ and 5 $\mu m/s$ (or 3 $\mu m/s$) every 800 μm in shear displacement to capture slip stability behavior, until reaching 9600 μm in total shear displacement.

Stage3. **Slide-Hold-Slide Experiments:** Reactivate fractures after various hold durations (100 s, 500 s, 800 s, and 1000 s) to determine frictional healing and creep.

The experimental program is summarized in **Table 3-1**, with the results of each test reported, analyzed and summarized in the following sections.

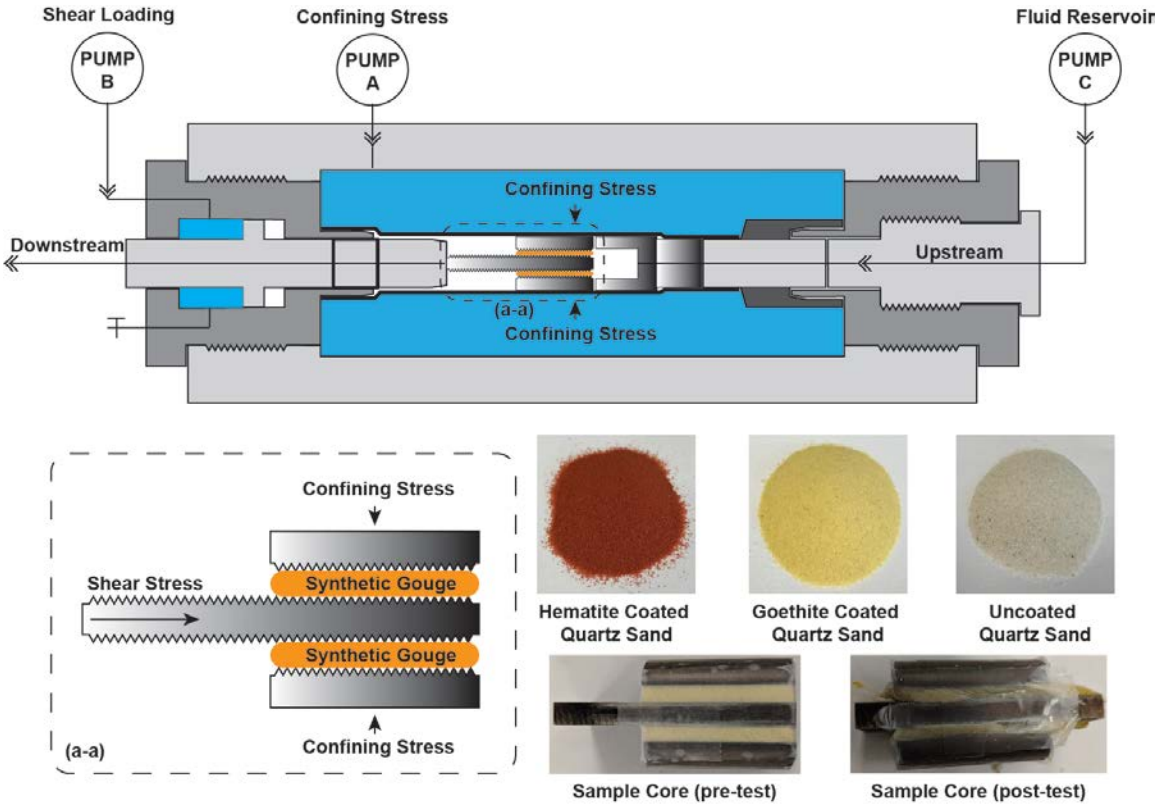

Figure 3-1. DDS inside a TEMCO simple-triaxial pressure vessel (upper). Confining stress is maintained via pump A, shear loading is supplied by pump B, and fluid flow parallel to the shear direction is supplied by pump C. (a-a) is the zoomed-in view of the sample core, showing the arrangement of the gouge and the direction of the applied stress. The lower right panels show the experimental materials (hematite coated quartz sand, goethite coated quartz sand, and uncoated quartz sand) and the platens and samples both before and after the shear test.

Table 3-1. Test program.

Test	Experiment Material	Initial Sample Thickness (mm)	Velocity Step (μm/s)	Hold-slide-hold duration (s)
uqz-2mm	Uncoated quartz	2	10/5/10/5/3/5/10	100/500/800/1000
uqz-3mm	Uncoated quartz	3	10/5/10/5/3/5/10	100/500/800/1000
hqz-2mm	Hematite coated quartz	2	10/5/10/5/3/5/10	100/500/800/1000

hqz-3mm	Hematite coated quartz	3	10/5/10/5/3/5/10	100/500/800/1000
gqz-2mm	Goethite coated quartz	2	10/5/10/5/3/5/10	100/500/800/1000
gqz-3mm	Goethite coated quartz	3	10/5/10/5/3/5/10	100/500/800/1000

3 Results

3.1 Evolution of shear strength and permeability

The evolution of shear strength (friction) and permeability of all experiments are shown in **Figure 3-2**. All samples show a typical trajectory reaching peak strength in the first ~1000 μm of shear displacement then decline to a residual strength over the next ~500 μm. Specifically, the hematite-coated quartz shows the highest peak shear strength followed by the Goethite then the un-coated control (**Figure 3-2**(a-a)), with these consistent with previous laboratory observations using similar test materials (Choo et al., 2015; Larrahondo et al., 2011b; Larrahondo & Burns, 2014). Despite the difference in peak shear strengths, all samples return similar residual shear strengths (except hqz-2mm which is slightly higher). All tests exhibit a slight long-term strengthening effect, which is plausibly an artifact caused by the geometric thinning of the gouge sample and resulting strain-strengthening effect.

Permeability evolution for the 2 mm and 3 mm thickness samples are shown in **Figures 3-2**(b) and (c), respectively. Permeability generally increases during the first ~4000 μm of shear displacement, followed by a continuous decrease. For the 3 mm thickness samples, the un-coated quartz features the highest peak permeability and the most

significant permeability decline; the Goethite-coated quartz shows a lower overall permeability with only a moderate decrease; and the hematite-coated quartz, begins with the smallest permeability and then further decreases with shear displacement. Conversely, permeability evolution for the 2 mm gouge samples shows similar permeability enhancement during the first ~4000 μm of shear displacement, after which the permeability of the un-coated and hematite-coated samples both significantly decrease while the permeability of goethite-coated quartz only decreases slightly. Interestingly, although different initial sample thickness seems to not affect the permeability evolution pattern and results in similar residual permeabilities ($5 \times 10^{-12}\ m^2$), the peak permeability of the 2 mm gouge samples is almost double that of the permeability of 3 mm gouge samples. One possible explanation is that there are more grains perpendicular to the fluid flow direction in the 3 mm samples than that of 2 mm samples – resulting in more tortuous flow channels which affect bulk permeability negatively.

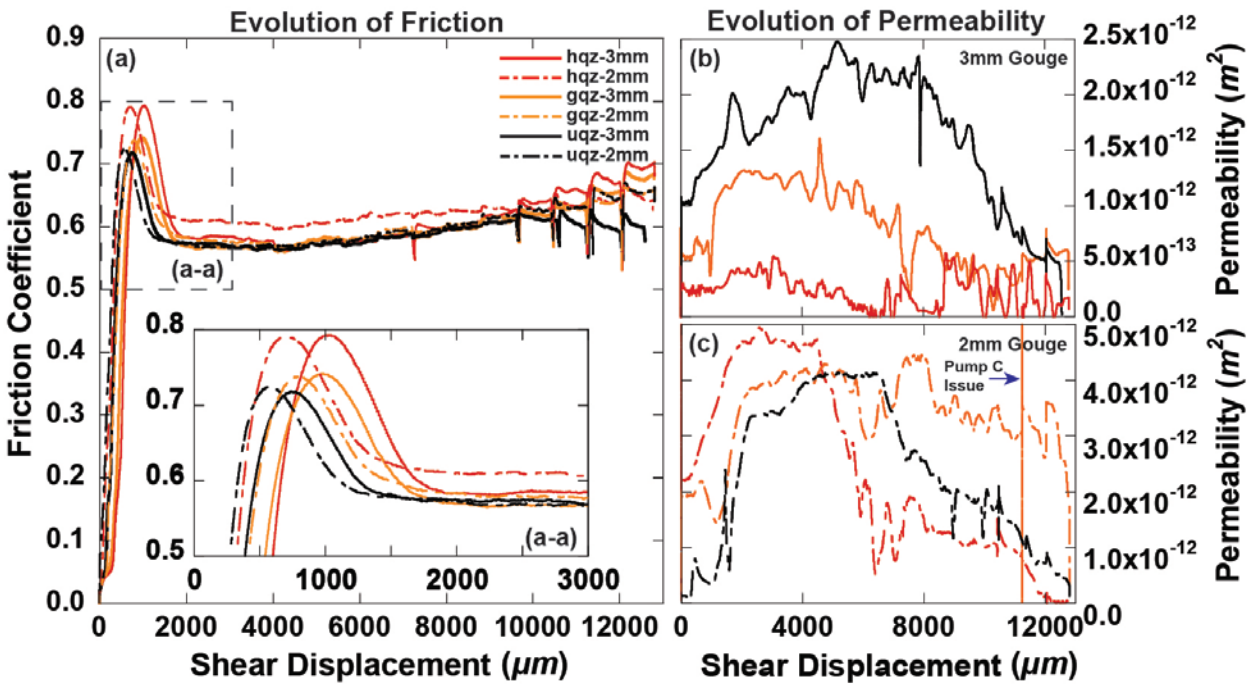

Figure 3-2. (a) Evolution of shear strength (interpreted as friction) for all six experiments, (a-a) is a zoomed-in on friction evolution from 0 to 3000 μm. Hematite-coated quartz shows the highest peak shear strength while uncoated quartz shows the lowest; (b) Permeability evolution of 3 mm gouge samples. Permeabilty generally increases initially and then decreases. Un-coated quartz shows the largest permeability reduction with hematite-coated quartz having the lowest initial permeabilty; (c) Permeability evolution for 2 mm and 3mm thick gouge sampls show similar trends. Hematite-coated quartz and un-coated quartz show a significant reduction in permeability after an initial increase, while the Goethite-coated quartz shows only a moderate decrease.

3.2 Slip stability, frictional healing and creep

$(a-b)$ values, frictional healing rate, and creep rate are the among the most important stability parameters which determine the potential-for, and style-of, reactivation of faults. $(a-b)$ values are obtained from the friction evolution of each velocity step (Stage2; velocity stepping, typically from ~4000 μm to ~9600 μm in shear displacement). A typical friction evolution at a velocity step is shown in **Figure 3-3**(a), in which the long-

term global strenghtneing trend is removed (red vs. black evolution curve). The $(a-b)$ values of all tests are summarized in **Figure 3-3**(b). Both hematite-coated and un-coated quartz feature positive and negative $(a-b)$ values, indicating velcoity neutral behavior. However, Goethite-coated quartz shows only positive $(a-b)$ values, suggesting mostly velcoity strengthening behavior. The un-coated quartz shows a wider range of $(a-b)$ values while coated quartz shows a narrower spectrum.

Frictional healing rates and creep rates are obtained through slide-hold-slide experiments (Stage3: slide-hold-slide, typically from ~9600 μm to 12500 μm in shear displacement). Frictional healing rate defines how rapidly the sample evolves to peak friction after reinitiating sliding from the prior steady state friction before the previous hold. Creep rate is defined as the decrease in friction per unit time during holds. The results of frictional healing rate and creep rate are summarized in **Figure 3-3**(c) and (d). In terms of frictional healing, the Goethite-coated quartz shows the highest healing rate (0.013, slope calculated agaisnt logarithmic time), which is almost double that for hematite-coated quartz (0.007). Un-coated quartz shows a similar frictional healing rate as the Goethite-coated quartz (0.012). Goethite-coated quartz also shows the highest creep rate (0.056) followed by hematite- (0.048), then un-coated quartz (0.031). Goethite coatings increase both frictional healing and creep rate, while hematite coatings increase creep rate but decrease the frictional healing rate of the gouge sample.

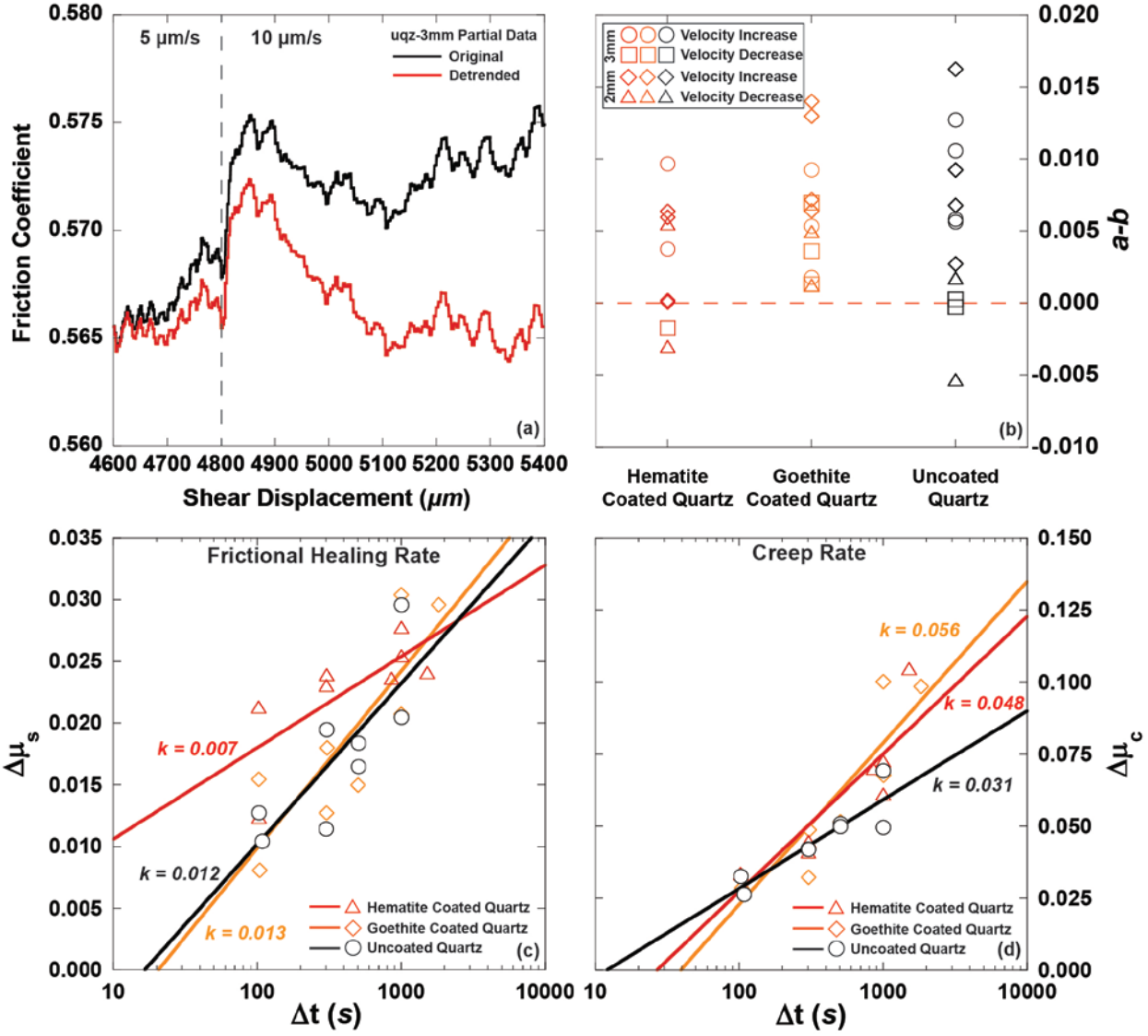

Figure 3-3. (a) Typical frictional evolution at a velocity step from test Stage 2 (velocity-stepping). The global strengthening trend is removed to determine the stability parameter (a-b); (b) Summary of stability parameter (a-b) from all tests. Un-coated and hematite-coated quartz show velocity neutral behavior (featuring both positive and negative (a-b) values), while Goethite-coated quartz shows velocity strengthening behavior (featuring positive (a-b) values); (c) Summary of frictional healing rate calculated from test Stage 3 (slide-hold-slide). Goethite-coated quartz shows the highest healing rate, while hematite-coated quartz shows the lowest; (d) Summary of creep rates. Goethite-coated quartz shows the highest creep rate followed by hematite- then un-coated quartz.

4 Discussion

4.1 Implications from morphological analysis

From the preceding, it is apparent that hematite- and Goethite- coatings exert different influences on the mechanical and rheological responses of faults. We perform a morphological analysis of the gouge samples both before and after the shear experiments to further explore the controlling micro-mechanisms. Scanning electron micrographs (SEM) of hematite- and Goethite-coated quartz grains from before and after shearing are shown in **Figure 3-4**(a) and (b), respectively. From the SEM images, the hematite coating particles are shown to be polyhedral in shape and scattered uniformly on the quartz grain surface, with individual coating particles <1 μm in diameter. Conversely, the Goethite-coating is fiber-like, featuring a moderate degree a of overlap between adjacent particles and seems to have a strongger attachment on the host quartz grains. The length of each Goethite fiber can be as small as sub-micron and as large as ~5 μm. These coating materials increase the complexity of surface texture of hosting quartz grains, thus increasing frictional resistance. Addtionally, contacting Goethite-coated quartz fibers may feature less frictional resistance due to the perpendicularly arranged fibers promoting sliding over interlocking. This geometric effect may be one of the explanations why Goethite-coated quartz shows a lower peak frictional strength than hematite-coated quartz. Due to the lack of complex grain texture provided by the coating materials, the uncoated quartz may consequently show the lowest peak shear strength.

To further investigate the influence of hematite- and goethite- coatings on the permeability evolution of faults, the samples are carefully collected, air-dried, and analyzed after the shear test. **Figures 3-4**(c) and (d) are SEM images of hematite and goethite coated quartz grains after shear tests. **Figure 3-4**(c) shows the hematite coating no longer uniformly distributed on the host grain substrate. Instead, clustered hematite coating is observed on the host grains. The origins of these clusters are possibly due to fluid-coating interactions, in which hematite coating materials are transported and deposited in clusters, by the fluid.

Additionally, wear products are typically observed either attaching to the host grain (marked in **Figure 3-4**(c)) or scattered in the background. No drastic change in the pre- and the post-test distribution of coating materials is observed in the Goethite-coated quartz after the shear tests (**Figure 3-4**(d)). Transport by the circulating fluid seems to exert less influence on the Goethite coatings, as evident from the empty substrate surface, devoid of Goethite fibers (highlighted in **Figure 3-4**(d)).

The SEM images suggest that the hematite coatings, as fabricated in this study, feature a weaker attachment to the host grains relative to goethite. However, the hematite tends to form clusters post- mechanical shear and fluid flow, suggesting a high degree of self-cohesion. The images also suggest that hematite coatings are readily transported by fluid than the Goethite coatings.

4.2 Permeability evolution mechanism

In addition to the SEM images, particle size distributions (PSD) are measured for the hematite- and goethite-coated samples, both before and after the shear tests. Coated samples pre- and post-test are dispersed on a transparent glass surface and scanned *via* identical sampling windows (100 mm^2 in area). Representative results are summarized in **Figure 3-4**(e). The hematite-coated quartz shows a slight increase in fine particles after shear. Conversely, the goethite-coated quartz sample shows a reduced percentage of fine particles. The number of particles in the hematite-coated quartz is reduced by ~25% after shear (center panel of **Figure 3-4**(e)), and is likely due to the clustering of coatings and loss of coatings through fluild transport to the downstream (reddish colorartion is noticed in the downstream fluid). Conversly, an increase in total number of particles is observed in the goethite coated quartz samples, indicating the generation of wear products.

Together, the combined PSD and SEM observations suggest that permeability evolution is controlled by the accumulation and transport of wear products and coating particles clogging the flow channels. This is the key mechanism in the signficant permeability reduction for the hematite-coated quartz, with its absence implicated in the reduced impact for the goethite cements.

Additionally, during holds (Stage3, slide-hold-slide) for several tests, a gradual permeability increase is observed. A representative example is shown in **Figure 3-4**(f) and (g). Specifically, **Figure 3-4**(f) follows permeability evolution with shear displacement, and **Figure 3-4**(g) shows permeability versus time. During the hold, between 3600 s and 5500 s, the permeability of the gouge sample increases. This may be counterintuitive as

previous observations suggest permeability decline due to fault sealing (Elkhoury et al., 2006; Im et al., 2018b). However, we argue that clogging and unclogging of wear products can dominate the permeability of gouge layers by controlling major flow channels at low confining stress. Some unclogging can occur during holds due to the effects of transport, which unclogs certain flow channels.

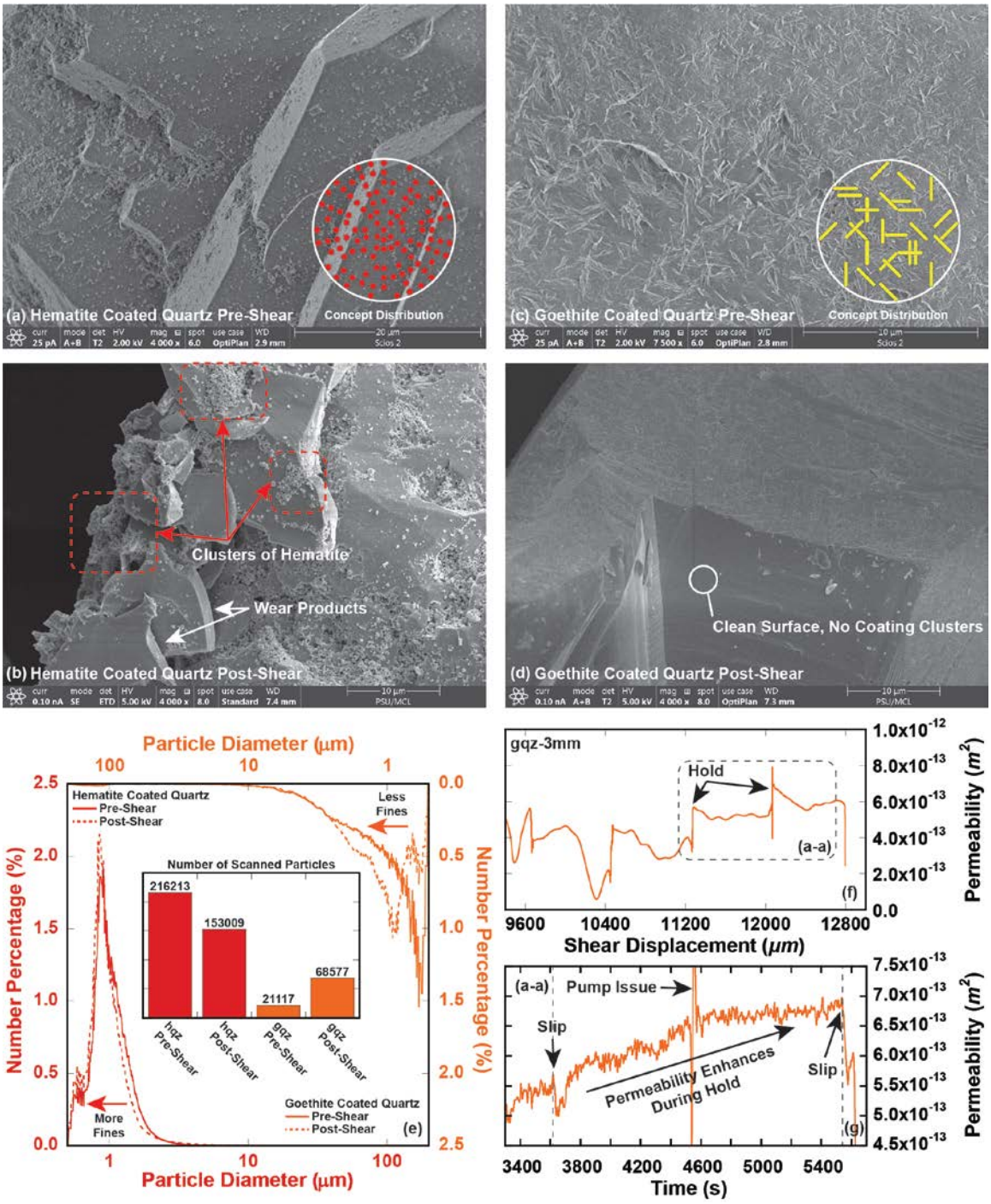

Figure 3-4. (a) Typical SEM image of hematite-coated quartz before the test. Hematite crystals are polyhedral and uniformly scattered on the quartz surface. (b) Typical SEM image of goethite-coated quartz before the test. Goethite crystals are fiber-like and uniformly distributed on the quartz surface. (c) Hematite-coated quartz after the shear-permeability test. Wear products and clustering of coating particles highlighted. (d) Goethite-coated quartz after the shear-permeability test. Clean

damage surfaces are observed, suggesting strong attachment of goethite coating. (e) Particle size distribution (PSD) analysis of hematite- and goethite- coated quartz before and after tests. (f) Permeability evolution of gqz-3mm from a displacement of ~9600 μm. Permeability increases during holds. (g) Zoomed-in (a-a) permeability vs. time. Permeability increases in holds are observed.

5 Conclusions

We report observations and analysis of the influence of hematite and goethite coatings on the shear strength, slip stability, and permeability evolution of quartz. The hematite- and goethite-coated quartz samples are synthesized in the laboratory as analog pristine and CO_2-transformed fault gouge. A novel double direct shear (DDS) apparatus has been implemented in the simple-triaxial pressure vessel to conduct shear-permeability tests on the coated samples. The response of the coated quartz samples before, during and following shear experiments suggest:

1. Both hematite- and goethite- coated quartz show higher peak shear strength than un-coated quartz; goethite-coated quartz is slightly weaker than hematite-coated quartz in peak shear strength.
2. Goethite-coated quartz show velocity-strengthening behavior while featuring a higher frictional healing rate, creep rate, and permeability. This suggests a reduced risk of seismic reactivation but greater loss of inventory in the long-term containment of CO_2.

3. Hematite coatings show weaker attachment to host quartz grains than goethite coatings and feature a high degree of mobility and self-clustering upon fluid interaction.
4. Wear products are generated during mechanical shear. The transport of these wear products can clog fluid conduits during shearing, thus significantly reducing permeability parallel to the shear direction.

This study provides insights into how hematite and goethite coatings, before and after long-term geochemical alteration by CO_2, can influence shear strength, stability, and permeability evolution of faults during shearing. Future experiments, potentially long-term shear-permeability tests, on natural samples are necessary to strengthen these conclusions.

References

Altman, S. J., Aminzadeh, B., Balhoff, M. T., Bennett, P. C., Bryant, S. L., Cardenas, M. B., et al. (2014a). Chemical and hydrodynamic mechanisms for long-term geological carbon storage. *Journal of Physical Chemistry C, 118*(28), 15103–15113. https://doi.org/10.1021/jp5006764

Altman, S. J., Aminzadeh, B., Balhoff, M. T., Bennett, P. C., Bryant, S. L., Cardenas, M. B., et al. (2014b). Chemical and hydrodynamic mechanisms for long-term geological carbon storage. *Journal of Physical Chemistry C, 118*(28), 15103–15113. https://doi.org/10.1021/jp5006764

Benson, S. M., & Cole, D. R. (2008). CO2 sequestration in deep sedimentary formations. *Elements*, *4*(5), 325–331. https://doi.org/10.2113/gselements.4.5.325

Choo, H., Larrahondo, J., & Burns, S. E. (2015). Coating Effects of Nano-Sized Particles onto Sand Surfaces: Small Strain Stiffness and Contact Mode of Iron Oxide–Coated Sands. *Journal of Geotechnical and Geoenvironmental Engineering*, *141*(1), 04014077. https://doi.org/10.1061/(ASCE)GT.1943-5606.0001188

Collettini, C., Niemeijer, A. R., Viti, C., & Marone, C. (2009). Fault zone fabric and fault weakness. *Nature*, *462*(7275), 907–910. https://doi.org/10.1038/nature08585

Cornell, R. M., & Schwertmann, U. (2003). *The Iron Oxides: Structure, Properties, Occurences and Uses.* Wiley-VCH.

Cundy, A. B., & Hopkinson, L. (2005). Electrokinetic iron pan generation in unconsolidated sediments: Implications for contaminated land remediation and soil engineering. *Applied Geochemistry*, *20*(5), 841–848. https://doi.org/10.1016/j.apgeochem.2004.11.014

Dieterich, J. H. (1978). Time-dependent friction and the mechanics of stick-slip. *Pure and Applied Geophysics PAGEOPH*, *116*(4–5), 790–806. https://doi.org/10.1007/BF00876539

Dieterich, J. H. (1979a). Modeling of rock friction 1. Experimental results and constitutive equations. *Journal of Geophysical Research: Solid Earth*, *84*(B5), 2161–2168. https://doi.org/10.1029/JB084iB05p02161

Dieterich, J. H. (1979b). Modeling of rock friction 2. Simulation of preseismic slip. *Journal of Geophysical Research: Solid Earth*, *84*(B5), 2169–2175. https://doi.org/10.1029/JB084iB05p02169

Elkhoury, J. E., Brodsky, E. E., & Agnew, D. C. (2006). Seismic waves increase permeability. *Nature*, *441*(7097), 1135–1138. https://doi.org/10.1038/nature04798

Ellsworth, W. L. (2013). Injection-induced earthquakes. *Science*, *341*(6142), 1–8. https://doi.org/10.1126/science.1225942

Elsworth, D., Spiers, C. J., & Niemeijer, A. R. (2016). Understanding induced seismicity. *Science*. https://doi.org/10.1126/science.aal2584

Fang, Y., Wang, C., Elsworth, D., & Ishibashi, T. (2016). Friction-permeability relationships for reservoir caprocks. *50th US Rock Mechanics / Geomechanics Symposium 2016*, *3*.

Fang, Y., Wang, C., Elsworth, D., & Ishibashi, T. (2017). Seismicity-permeability coupling in the behavior of gas shales, CO2 storage and deep geothermal energy. *Geomechanics and Geophysics for Geo-Energy and Geo-Resources*, *3*(2), 189–198. https://doi.org/10.1007/s40948-017-0051-9

Fang, Y., Elsworth, D., Wang, C., & Jia, Y. (2018). Mineralogical Controls on Frictional Strength, Stability, and Shear Permeability Evolution of Fractures. *Journal of Geophysical Research: Solid Earth*, *123*(5), 3549–3563. https://doi.org/10.1029/2017JB015338

Guglielmi, Y., Cappa, F., Avouac, J. P., Henry, P., & Elsworth, D. (2015). Seismicity triggered by fluid injection-induced aseismic slip. *Science*, *348*(6240), 1224–1226. https://doi.org/10.1126/science.aab0476

Im, K., Elsworth, D., Marone, C., & Leeman, J. (2017). The Impact of Frictional Healing on Stick-Slip Recurrence Interval and Stress Drop: Implications for Earthquake Scaling. *Journal of Geophysical Research: Solid Earth*, *122*(12), 10,102-10,117.

https://doi.org/10.1002/2017JB014476

Im, K., Elsworth, D., & Fang, Y. (2018a). the Influence of Pre-Slip Sealing on the Permeability Evolution on Fractures and Faults. *Geophysical Research Letters*, 1–10. https://doi.org/10.1002/2017GL076216

Im, K., Elsworth, D., & Fang, Y. (2018b). The influence of Preslip Sealing on the Permeability Evolution of Fractures and Faults. *Geophysical Research Letters*, *45*(1), 166–175. https://doi.org/10.1002/2017GL076216

Larrahondo, J., & Burns, S. E. (2014). Laboratory-Prepared Iron Oxide Coatings on Sands: Surface Characterization and Strength Parameters. *Journal of Geotechnical and Geoenvironmental Engineering*, *140*(4), 04013052. https://doi.org/10.1061/(ASCE)GT.1943-5606.0001068

Larrahondo, J., Choo, H., & Burns, S. E. (2011a). Laboratory-prepared iron oxide coatings on sands: Submicron-scale small-strain stiffness. *Engineering Geology*, *121*(1–2), 7–17. https://doi.org/10.1016/j.enggeo.2011.04.009

Larrahondo, J., Choo, H., & Burns, S. E. (2011b). Laboratory-prepared iron oxide coatings on sands: Submicron-scale small-strain stiffness. *Engineering Geology*, *121*(1–2), 7–17. https://doi.org/10.1016/j.enggeo.2011.04.009

Mair, K., & Marone, C. (1999). Friction of simulated fault gouge for a wide range of velocities and normal stresses. *Journal of Geophysical Research: Solid Earth*. https://doi.org/10.1029/1999JB900279

Major, J. R., Eichhubl, P., Dewers, T. A., Urquhart, A. S., Olson, J. E., & Holder, J. (2014). The effect of CO2-related diagenesis on geomechanical failure parameters; fracture testing of CO2-altered reservoir and seal rocks from a natural analog at Crystal Geyser, Utah. In *48th US Rocks Mechanics/Geomechanics Symposium* (Vol. 14–7463, pp. 1–5).

Marone, C. (1998). Laboratory-Derived Friction Laws and Their Application To Seismic Faulting. *Annual Review of Earth and Planetary Sciences*, *26*(1), 643–696. https://doi.org/10.1146/annurev.earth.26.1.643

Marone, C., Raleigh, C. B., & Scholz, C. H. (1990). Frictional behavior and constitutive modeling of simulated fault gouge. *Journal of Geophysical Research*, *95*(B5), 7007–7025. https://doi.org/10.1029/JB095iB05p07007

Rao, S. M., Sridharan, A., & Ramanath, K. P. (1995). Collapse behavior of an artificially cemented clayey silt. *Geotechnical Testing Journal*, *18*(3), 334–341. https://doi.org/10.1520/GTJ11002J

Rice, J. R., Lapusta, N., & Ranjith, K. (2001). Rate and state dependent friction and the stability of sliding between elastically deformable solids. *Journal of the Mechanics and Physics of Solids*, *49*(9), 1865–1898. https://doi.org/10.1016/S0022-5096(01)00042-4

Rinehart, A. J., Dewers, T. A., Broome, S. T., & Eichhubl, P. (2016). Effects of CO2on

mechanical variability and constitutive behavior of the Lower Tuscaloosa Formation, Cranfield Injection Site, USA. *International Journal of Greenhouse Gas Control*, *53*, 305–318. https://doi.org/10.1016/j.ijggc.2016.08.013

Ruina, A. (1983). Slip instability and state variable friction laws. *Journal of Geophysical Research: Solid Earth*. https://doi.org/10.1029/JB088iB12p10359

Samuelson, J., Elsworth, D., & Marone, C. (2009). Shear-induced dilatancy of fluid-saturated faults: Experiment and theory. *Journal of Geophysical Research: Solid Earth*, *114*(12), 1–15. https://doi.org/10.1029/2008JB006273

Scheidegger, A., Borkovec, M., & Sticher, H. (1993). Coating of silica sand with goethite: preparation and analytical identification. *Geoderma*, *58*(1–2), 43–65. https://doi.org/10.1016/0016-7061(93)90084-X

Schwertmann, U. (1971). Transformation of hematite to goethite in soils [4]. *Nature*, *232*(5313), 624–625. https://doi.org/10.1038/232624a0

Wang, C., Elsworth, D., & Fang, Y. (2017). Influence of weakening minerals on ensemble strength and slip stability of faults. *Journal of Geophysical Research: Solid Earth*, *122*(9), 7090–7110. https://doi.org/10.1002/2016JB013687

Wang, C., Elsworth, D., Fang, Y., Liu, K., & Jia, Y. (2017). Weakening effects of microstructural tribological films in CO2-altered reservoirs and caprocks. *American Rock Mechanics Association*, 8.

Yasuhara, H., Polak, A., Mitani, Y., Grader, A. A. S., Halleck, P. M., & Elsworth, D. (2006). Evolution of fracture permeability through fluid-rock reaction under hydrothermal conditions. *Earth and Planetary Science Letters*, *244*(1–2), 186–200. https://doi.org/10.1016/j.epsl.2006.01.046

Zoback, M. D., & Gorelick, S. M. (2012). Earthquake triggering and large-scale geologic storage of carbon dioxide. *Proceedings of the National Academy of Sciences*, *109*(26), 10164–10168. https://doi.org/10.1073/pnas.1202473109

Chapter 4

Influence of Fracture Roughness on Shear Strength, Slip Stability and Permeability: A Micro Mechanistic Analysis by 3D Digital Rock Physics

Abstract

Subsurface fluid injections can disturb the effective stress regime by elevating pore pressure and potentially reactivate faults and fractures. Laboratory studies indicate that fracture rheology and permeability s in such reactivation events are linked to the roughness of the fracture surfaces. We construct discrete element method (DEM) models to explore the influence of fracture surface roughness on the shear strength, slip stability, and permeability evolution during such slip events. For each simulation, a pair of analog rock coupons (3D bonded quartz-particle analogs) representing a mated fracture are sheared under a velocity-stepping scheme. The roughness of the fracture is defined in terms of asperity height and asperity wavelength. Results show that (1) samples with larger asperity heights (rougher), when sheared, exhibit a higher peak strength which quickly devolves to a residual strength after a threshold shear displacement; (2) these rougher samples also exhibit greater slip stability due to a high degree of asperity wear and resultant production of wear products; (3) long-term suppression of permeability is observed with rougher fractures, which is plausibly due to the removal of asperities and redistribution of wear products, which locally reduces porosity in the dilating fracture. This study provides

insights into the understanding of the mechanisms of frictional and rheological evolution of rough fractures anticipated during reactivation events.

1. Introduction

Human interventions into the subsurface, such as hydraulic fracturing, enhanced geothermal stimulation, and carbon sequestration involve injecting large volumes of fluid at high overpressures. Such interventions disturb the stress field by elevating pore pressure and altering far-field stress (Elsworth et al., 2016), potentially resulting in the reactivation and potential seismic rupture of pre-existing faults and fractures. Hydraulic fracturing, in particular, attempts to create engineered fracture networks by injection to stimulate hydrocarbon production. These hydraulic fractures, while creating possibility to extract hydrocarbon resources from tight shale, can be extremely vulnerable to seismic failure upon stress perturbation (Ellsworth, 2013; Walsh and Zoback, 2015; Zoback and Gorelick, 2012), causing hazardous consequences. One key question in understanding the seismic cycle is in unraveling the evolution of shear strength, stability, and permeability of fault and fractures that may contribute to dynamic slip events.

Previous laboratory shear experiments on faults and fractures show permeability declines over shear slip, which may be caused by clay swelling or clogging of wear products. (Fang et al., 2017b; Im et al., 2017; Fang et al., 2018a; Ishibashi, et al., 2018). These observations reflect the friction-stability-permeability relationships at low confining stresses for fractures with small roughness, i.e., asperity size of the order of micrometers. A recent study reports that in the injection-induced shear slip experiment, asperity degrades

but the surface roughness would still contribute to increasing permeability (Ye and Ghassemi, 2018). Investigations on fabricated fractures with controlled roughness suggest that roughness patterns exert a strong control on permeability evolution *via* competitive effects of compaction and dilation during shearing (Fang et al., 2018b). However, due to the lack of direct tracking in lab conditions, it is still not clear how mechanistically the asperities of fractures evolve during shear, which further controls the permeability evolution.

Traditional direct shear experimental studies have suggested that the shear strength of fractures are closely linked to surface roughness (Barton, 1973; Barton and Choubey, 1977). Empirical indices have been developed to describe the roughness of rock surfaces on the order of millimeters using parameter such as JRC (joint roughness coefficient) and JCS (joint compressive strength). Correspondingly, rougher surfaces undergo greater dilation when sheared, resulting in an increase in aperture and enhancement of permeability. However, breakage and degradation of asperities can lead to impeded dilation, reduced aperture, and reduction in permeability (Barton et al., 1985; Elsworth and Goodman, 1986; Segall and Rice, 1995). Laboratory and numerical shear experiments have been conducted on rough specimens which feature “saw-tooth” or sinusoidal shaped asperities (Asadi et al., 2013). These studies suggest that the breakage and degradation of asperities are linked to normal stress, bonding strength, and asperity geometry. These studies, however, lack proper reproduction of the stochastic characteristics of natural rough rock surfaces. Mathematical algorithms have been developed to describe the natural roughness of rock surfaces (Brown and Scholz, 1985). The theories suggest three key

parameters to describe a rough rock surface: (1) the root mean square (RMS) roughness including variance of amplitude and distribution of the asperities; (2) the length scale for degree of mismatch; and (3) fractal parameters (Brown, 1995).

Numerical approaches have been adopted to investigate the effects of roughness on the shear strength of rock joints. While continuum numerical models are implemented to simulate the onset of shear failure of rough joints and fractures, discrete element methods (DEM) (Cundall and Strack, 1979a) provide one method to follow the progression of failure of rough fractures. In DEM models, the surface profiles can be reproduced, and the damage of asperities can be tracked during a simulated shear test (Cundall, 2000). DEM studies have examined the evolution of the shear strength of fractures described by JRC profiles and shown that tensile failure dominates the breakage of asperities and development of micro cracks (Park and Song, 2009). DEM models have also been used to investigate the evolution of shear strength, slip stability, and permeability of gouge materials (Guo and Morgan, 2004; Morgan and Boettcher, 1999; Morgan, 1999; Sun et al., 2016; Wang et al., 2017). However, no DEM studies to date have explored the ensemble of rough surface profiles featuring stochastic characteristics, and the linkage of shear strength, slip stability, and permeability evolution.

We report results investigating the influences of surface roughness on the evolution of shear strength, slip stability, and permeability of fractures. We utilize a series of virtual rough surfaces by DEM with variations in asperity roughness, wavelength and degree of wavelength anisotropy.

2. Numerical method

We create virtual rough fracture surfaces using a simplified stochastic method and utilize the distinct element method (DEM) to construct our numerical model. DEM solves Newton's second law iteratively for the mechanical interactions of a bonded particle assembly. A modified slip-weakening friction constitutive model is implemented on particle-particle contacts to represent slip evolution and the evolution of fracture porosity and permeability.

2.1 Fracture roughness

Three key parameters may be used to define fracture roughness: (1) the root mean square (RMS) roughness; (2) the length scale for degree of mismatch; and (3) a fractal parameter/dimension. Each of these parameters plays a role in influencing the dynamic response of fractures during reactivation events. In this study, we focus on the first order effect of roughness on the shear strength, slip stability and permeability of mated fractures prone to reactivation. Therefore, we simplify the characterization of the surface roughness by considering only the statistical size and distribution of asperities. We use the two key parameters: (1) the root mean square (RMS) height (S_q) of the asperities; (2) the wavelength (L_w) describing the distance between two statistically independent points. The RMS height of the asperities in a sample surface of area A can be expressed as:

$$S_q = \sqrt{\frac{1}{A}\iint z(x,y)dxdy} \quad (1)$$

in which z is the individual asperity height and (x, y) is the location of the asperity. In this study, we independently vary the RMS height (S_q), and the wavelength (L_w) in the two orthogonal directions (x and y) within the mean fracture plane to characterize different roughness profiles (Section 2.3).

2.2 Model construction

The model (**Figure 4-1**) in this study is developed *via* the Particle Flow Code 3D (PFC3D, Itasca Consulting Group. Inc.) utilizing the principles of DEM (Cundall and Strack, 1979b). The applicability of DEM to simulate the dynamic response of rocks and faults is summarized elsewhere (Abe et al., 2002; Antonellini and Pollard, 1995; Burbidge and Braun, 2002; Guo and Morgan, 2004; Morgan, 1999, 2004; Sun et al., 2016; Wang et al., 2017). The majority of DEM simulations are in two-dimensional (2D) configurations to reduce computational cost yet still produce representative results. However, drawbacks of neglecting out-of-plane interactions are the inability to reproduce the interaction of fracture surfaces with texture and roughness across a plane and in 3D. Therefore, in this study, we use a three-dimensional configuration to reproduce fracture surfaces with pre-defined roughness features.

Analog virtual rough fracture pairs (10 cm by 1 cm by ~0.5 cm each half) with pre-defined rough surfaces are sheared to simulate the dynamic response of intact fractures during reactivation events. Specifically, each rough fracture coupon is generated by filling a virtual box with particles with one side of the box replaced with a prescribed rough surface profile. The infilled particles are equilibrated to dissipate the kinetic energy caused

by initial infilling, i.e., cycling until the ratio of total unbalanced force to total body force is less than 0.001. Particles are then linked into an ensemble “lithified” fracture by parallel bonding. The pair of virtual rough rock fracture coupons with mated fracture surfaces are slowly brought together and confined with a prescribed confining stress (10 MPa). Once the incremented confining stress reaches the prescribed magnitude (10 MPa), the upper coupon is displaced laterally to shear against the static lower coupon at a prescribed shear velocity (1 $\mu m/s$). The shear velocity is incremented to 10 $\mu m/s$ after 5 mm of shear displacement and cycled back to 1 $\mu m/s$ after another 5 mm of shear displacement. The cycles continue until a total shear displacement of 25 mm is reached.

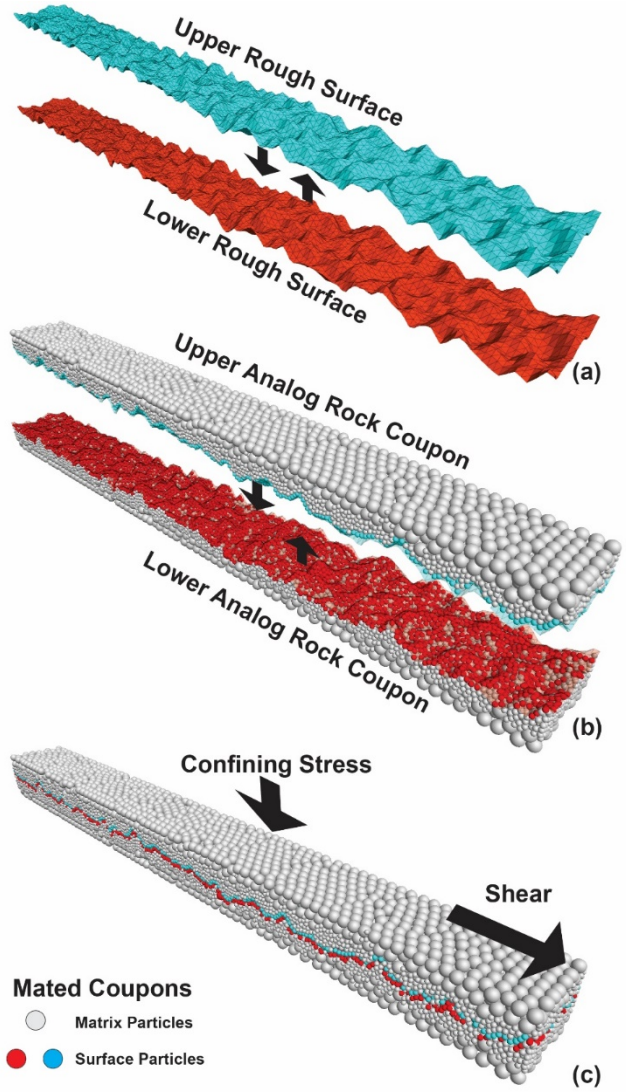

Figure 4-1. Model construction: (a) Two numerically generated rough surfaces are imported, ready to be brought together; (b) A virtual box (not shown) with one face replaced with one of the rough surfaces serves as a mold for one analog rock coupon. Particles are generated, equilibrated, and bonded inside the mold. A pair of analog rock coupons are generated at the same time. The rough surfaces are removed upon the completion of bonding. The particles located closest to the fracture surfaces are marked in blue and red; (c) The two coupons are confined under a prescribed (10 MPa) normal stress and the upper coupon of the specimen is loaded to initiate the shear test.

2.3 Contact model

The interaction of particles in the DEM model is determined by a contact model and contact properties. We use a modified parallel bond contact model (**Figure 4-2**) to describe the contact-contact interaction in the assembly. The modified parallel bond model consists of three main elastic components: (1) Linear elastic spring/sliders in the normal and shear direction of the contact; (2) Linear elastic bonds in the normal and shear direction with tensile strength and cohesion; (3) Rotation resistance (Ai et al., 2011; Iwashita and Oda, 1998; Jiang et al., 2015). The particles are bonded prior to the application of a confining stress with the breakage of bonds is tracked after the particles are bonded. The mechanical response of a contact before bond breakage is described as in **Figure 4-2**.

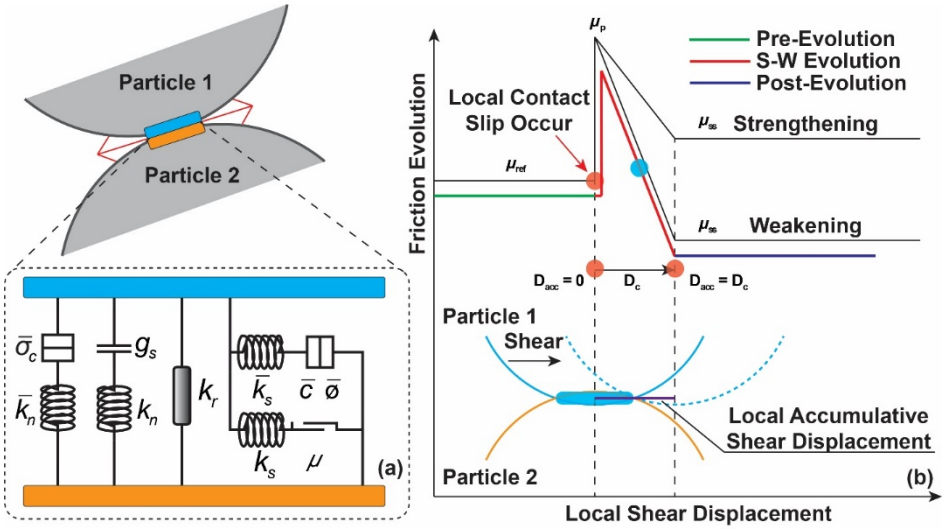

Figure 4-2. Contact model between bonded particles, (a) Schematic of the modified linear parallel bond model. A rotation resistance component is included to restrict any free rolling motion; (b) Evolution of friction coefficient at contacts upon local shear slip.

The force and moment within a bonded contact are,

$$F_c = F^l + \bar{F} \tag{2}$$

$$M_c = \bar{M} \tag{3}$$

where, F_c is the contact force and M_c is the contact moment. The contact force is resolved as the sum of linear forces (F^l) and parallel bond forces ($\bar{F}$). A detailed discussion of the component linear forces are discussed elsewhere (Potyondy and Cundall, 2004). The parallel bond force si resolved into normal and shear components and the parallel bond moment resolved into twisting and bending moments,

$$\bar{F} = -\bar{F}_n \hat{n}_c + \bar{F}_s \tag{4}$$

$$\bar{M} = \bar{M}_t \hat{n}_c + \bar{M}_b \tag{5}$$

in which, $\bar{F}_n$ and $\bar{F}_s$ are the normal and shear force components of the parallel bond, $\bar{M}_t$ and $\bar{M}_b$ are the twisting and bending moment components and $\hat{n}_c$ is the unit normal of the contacting plane. The contact force and moment are updated through the following relations,

$$\bar{R} = \begin{cases} \min\left(R^{(1)}, R^{(2)}\right) & ball - ball \\ R^{(1)} & ball - wall \end{cases} \tag{6}$$

$$\bar{A} = \pi \bar{R}^2 \tag{7}$$

$$\bar{I} = \frac{\pi \bar{R}^4}{4} \tag{8}$$

$$\bar{J} = \frac{\pi \bar{R}^4}{2} \tag{9}$$

$$\bar{F}_n := \bar{F}_n + \bar{k}_n \bar{A} \Delta \delta_n \tag{10}$$

$$\bar{F}_s := \bar{F}_s - \bar{k}_s \bar{A} \Delta \delta_s \tag{11}$$

$$\bar{M}_t = \bar{k}_s \bar{J} \theta_t \tag{12}$$

$$\bar{M}_b = \bar{k}_n \bar{I} \theta_b \tag{13}$$

in which $\bar{R}$ is the contact cross-sectional radius, $\bar{A}$ is the contact cross-sectional area, $\bar{I}$ is the moment of inertia of the cross-section, $\bar{J}$ is the polar moment of inertia of the

cross-section, $\Delta\delta_n$ and $\Delta\delta_s$ are incremental normal and shear displacements at the contact, $\bar{k}_n$ and $\bar{k}_s$ (stress/length) are the stress stiffness of the parallel bond and θ_t and θ_b is the twisting and bending angles of the contact, respectively.

The tensile and shear stresses within the parallel bond are defined as,

$$\bar{\sigma} = \frac{\bar{F}_n}{\bar{A}} + \bar{\beta}\frac{\|\bar{M}_b\|\bar{R}}{\bar{I}} \tag{14}$$

$$\bar{\tau} = \frac{\|\bar{F}_s\|}{\bar{A}} + \bar{\beta}\frac{\|\bar{M}_t\|\bar{R}}{\bar{J}} \tag{15}$$

$$\bar{\beta} \in [0,1] \tag{16}$$

where $\bar{\beta}$ is a moment-contribution factor (Potyondy, 2011). The resulting normal (tensile) and shear stresses are compared with specified bond strengths to determine survival or failure of the contact. If the contact fails, the parallel bond mechanism ceases to function, and the linear contact stiffness and rolling resistance must carry updates of the contact force and follow shear slip evolution.

The frictional response of the contact may be accommodated by quasi- rate and state friction (RSF). Rate and state friction law (Dieterich, 1978; Ruina, 1983) has been developed to describe the evolution of friction during slip of faults and fractures. The constitutive relation of rate and state friction, may be described as,

$$\mu = \mu_0 + a\ln\left(\frac{V}{V_0}\right) + b\ln\left(\frac{V_0\theta}{D_c}\right) \tag{17}$$

$$\frac{d\mu}{dt} = k\left(V_{lp} - V\right) \tag{18}$$

in which, μ is the friction coefficient μ_0 is the reference friction coefficient, V, V_0, and V_{lp} are the current, reference, and load point velocities of the system, θ, D_c, and k are

the state variable, characteristic slip distance, and system stiffness, respectively, and a and b are the stability parameters.

Although rate and state friction is able to match many of the first and second order features in the evolution of friction, it is computationally intensive when implemented on contact-level models, such as DEM (Abe et al., 2002). A simplified relation that replicates key features (Wang et al., 2017) is used here to reduce the computational cost. The constitutive relation (**Figure 4-2**(b)) may be represented as,

$$\mu_p = \mu_{ref} + a \ln\left(\frac{V_{lp}}{V_{ref}}\right) \tag{19}$$

$$\mu_{ss} = \mu_{ref} + (a - b) \ln\left(\frac{V_{lp}}{V_{ref}}\right) \tag{20}$$

$$\mu = \begin{cases} \mu_p \\ \mu_p - \left(\frac{\mu_p - \mu_{ss}}{D_c}\right) D_{acc} \\ \mu_{ss} \end{cases} \tag{21}$$

$$\mu = \begin{cases} \mu_p & D_{acc} = 0 \\ \mu_p - \left(\frac{\mu_p - \mu_{ss}}{D_c}\right) D_{acc} & D_{acc} \in (0, D_c) \\ \mu_{ss} & D_{acc} \in (0, D_c) \end{cases} \tag{22}$$

where μ_p, μ_{ref}, and μ_{ss} are the peak, reference, and steady state friction coefficient on the evolving contact, V_{lp} and V_{ref} are the current global shear velocity and global shear velocity from the last velocity step and D_{acc} is the accumulated shear displacement on the contact.

A slip event is initiated if the contact is broken by the resultant shear stress exceeding the frictional strength of the contact. The evolution of the contact friction depends on the local accumulative shear displacement, and the difference between current and previous global shear velocity. During a local slip event (single contact shear), the

friction begins to evolve following the red path in **Figure 4-2**(b) if there is a difference between current global slip rate and that of the previous velocity step. If the contact remains active (the two particles are in contact), the contact will evolve along the red path ($D_{acc} < D_c$) and transfers to the purple path at steady state ($D_{acc} \geq D_c$). The purple path is shown for velocity weakening, for clarity, but can also follow the path of velocity strengthening, depending on the magnitude of the stability parameters $(a - b)$ assigned to the contact. Where the contact becomes inactive before reaching steady state (the two particles are no longer in contact), the friction of the either contact will remain as-it-is on the red path (e.g. Wang et al., 2017). The material properties and parameters used in this study are enumerated in **Table 4-1**. Representative material properties for uniaxial compressive strength, tensile strength, and Young's modulus recovered from laboratory experiments (4 cm in diameter, 8 cm in height) are reported in **Table 4-2**.

Table 4-1. Model Parameters.

Parameter	Value
Particle Diameter (mm)	0.5 (near-fracture) / 1.25 (near-boundary)
Effective Modulus (MPa)	350
Stiffness Ratio	1
Parallel Bond Effective Modulus (MPa)	35
Parallel Bond Stiffness Ratio	1
Friction Coefficient	0.3
Rolling Resistance Ratio	0.5
a	0.0025
b	0.0050
Dc (μm)	50

Table 4-2. Material Properties.

Material Properties	Value
Young's Modulus (GPa)	2.10
Peak Compressive Strength (MPa)	76.60
Peak Tensile Strength (MPa)	11.50

2.4 Experiment matrix

We explore the influence of fracture roughness on the evolution of shear strength, slip stability, and permeability of rough fractures during slip events. Specifically, we separately contrast the impacts of: (1) Root mean square height of the asperities (rss1 through rss6); (2) Spatial distribution (asperity wavelength) of asperities (rss6, 7, 8, 9 for x-direction; rss6, 10, 11, 12, for y-direction); and (3) Tensile strength and cohesion of the wall-rock represented by particle bond strength (rss6, 13, 14). The spectrum of experimental variables are noted in **Table 4-3**.

Table 4-3. Experiment schedule.

Test	RMS (cm)	clx (cm)	cly (cm)	Tensile Strength (MPa)	Cohesion (MPa)
rss1	0.005	1.0	1.0	50	50
rss2	0.010	1.0	1.0	50	50
rss3	0.020	1.0	1.0	50	50
rss4	0.030	1.0	1.0	50	50
rss5	0.040	1.0	1.0	50	50
rss6	0.050	1.0	1.0	50	50
rss7	0.100	1.0	1.0	50	50
rss8	0.050	0.5	1.0	50	50
rss9	0.050	3.0	1.0	50	50
rss10	0.050	5.0	1.0	50	50
rss11	0.050	1.0	0.5	50	50
rss12	0.050	1.0	3.0	50	50
rss13	0.050	1.0	5.0	50	50
rss14	0.050	1.0	1.0	500	500
rss15	0.050	1.0	1.0	20	20

3. Results and analysis

We perform numerical direct shear tests on analog rock coupons with pre-defined roughness profiles. The experiments are conducted in velocity stepping mode with velocities up- and down-stepped between 1 $\mu m/s$ and 10 $\mu m/s$ over incremented shear offsets of 5 mm. The evolution of shear strength, slip stability, and permeability are followed as functions of the three properties of asperity height, wavelength and strength.

3.1 Evolution of shear strength

The virtual rock coupons are sheared to a total relative shear displacement of 25 mm in five velocity-stepped increments. The lower coupon is held in place while the upper coupon translates while restrained to deform parallel to the long-axis of the fracture. Confining stress is maintained constant at 10 MPa by a servo mechanism with shear and confining stresses monitored by summing contact forces on the corresponding loading walls. Friction coefficient is defined as the ratio of shear stress to normal stress. **Figure 4-3** shows the fracture surface profiles and the evolution of friction coefficient for tests rss1 through rss6. The analog coupons feature RMS asperity heights from 0.005 cm to 0.05 cm. Since confining stresses are maintained constant during the test, the shear strength scales as friction coefficient. The comparison shows an anticipated trend of increasing peak shear strength with increasing RMS asperity height. Shear stress builds until failure with a pronounced post-peak stress/strength drop. Test rss6 shows the highest peak friction (~0.65), and rss1 exhibits the lowest peak friction (~0.36). The magnitude of the stress drop

increases with the rms height as does the shear displacement required to mobilize peak strength. All the specimens stabilize at a similar coefficient of residual friction (~0.32) after failure.

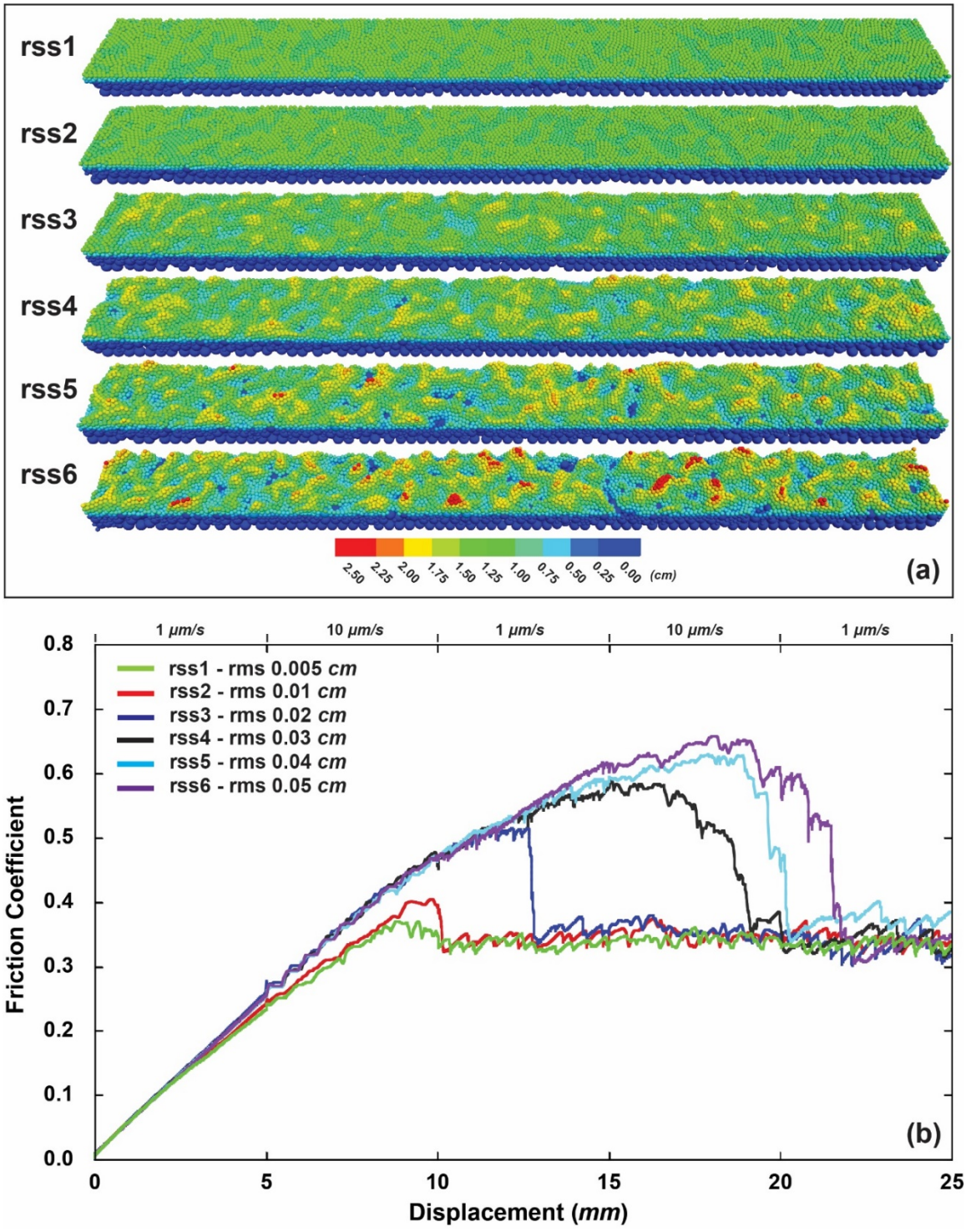

Figure 4-3. (a) Fracture surface profiles for rss1 through rss6. Lower fracture surfaces before shear with colored contours illustrating the topography of the surfaces (asperities). (b) Evolution of shear strength, interpreted as friction (τ/σ) for specimens with RMS asperity heights ranging from

0.005cm to 0.05cm (rss1 through rss6). The shear strength of the specimens generally increases with a sudden stress drop post-peak, sometimes comprising several successive stress drops. Specimens with rougher fractures exhibit a higher peak shear strength and larger threshold shear displacement to peak strength. All specimens show similar residual shear strength after failure.

3.2 Fracture dilation and permeability evolution

Fracture permeability is controlled by the local contribution to ensemble aperture along fluid channels formed by the interconnected pore network. These effects can be estimated by monitoring the evolution of sample dilatancy (scaled to change in sample thickness during shear) and local porosity along the fracture. In this study, the sample thickness is calculated as the distance between the virtual confining walls attached to the top and bottom of the analog coupons. Local porosity is measured by averaging measurements from five evenly distributed and equally sized sampling windows (spheres) placed along the fracture. The evolution of sample thickness for tests rss1 through rss6 are shown in **Figure 4-4**. The specimens begin with a total height/thickness of ~7.85 mm, and gradually dilate to a peak magnitude maintained as a plateau or slight compaction. Specimens with low RMS asperity heights (rss1 and rss2) reach a steady sample layer thickness after ~8 and ~10 mm of shear displacement, respectively. Specimens with larger asperities (rss3 through rss6, higher RMS) dilate significantly more (magnitude here) and also undergo larger relative displacement to reach peak dilation. For example, it takes ~22 mm of shear displacement for the roughest specimen (rss6) to reach maximum dilation – this peak dilation reached simultaneously with peak strength. Post peak strength, the samples no longer dilate (rss1-3) and in some cases compact slightly (rss4-6).

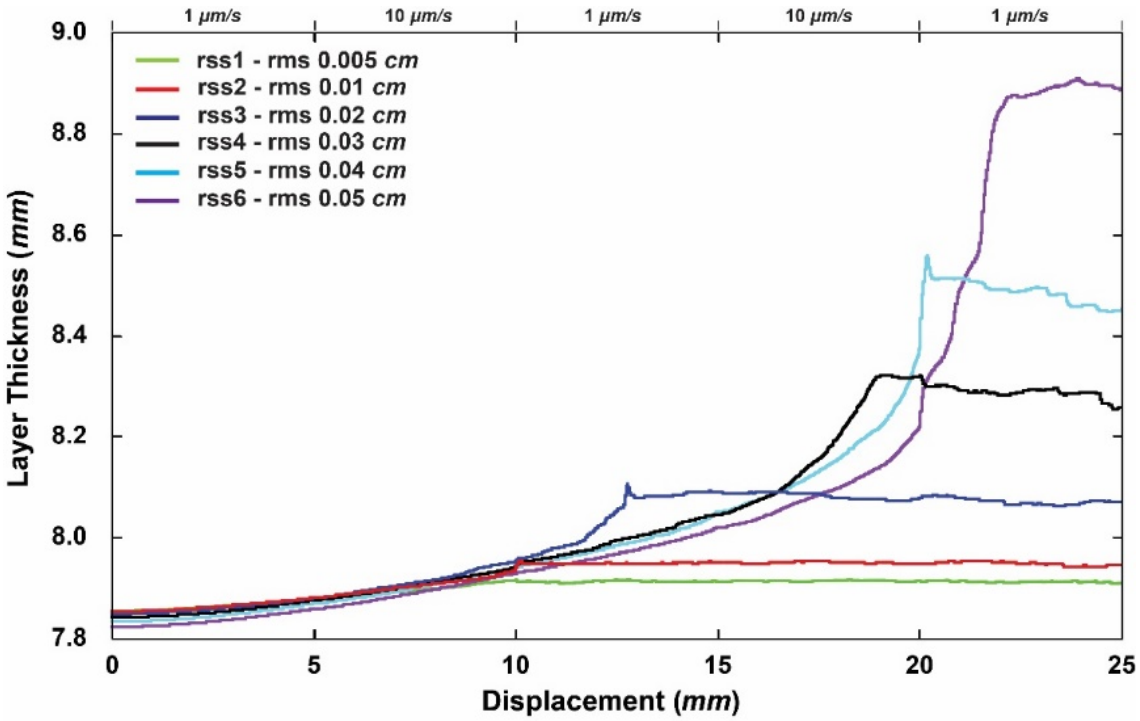

Figure 4-4. Evolution of sample thickness for specimens with RMS asperity heights ranging from 0.005cm to 0.05cm (rss1 through rss6). The specimens generally dilate until reaching a steady state or plateau where the sample thickness either ceases to increase (rss1-rss3) for small RMS or slightly compacts (rss4-rss6) for large RMS.

The evolution of fracture permeability is estimated from the local change in porosity sampled along the fracture (Ouyang and Elsworth, 1993; Samuelson et al., 2011),

$$\frac{k}{k_0} \cong (1 + \Delta\phi)^3 \tag{23}$$

in which k/k_0 is the relative change in permeability and $\Delta\phi$ is the change in porosity. Estimates of fracture permeability evolution (k/k_0) during shear for tests rss1 through rss6 are shown in **Figure 4-5**. Permeability of the fracture decreases slightly during the first ~10 mm of shear displacement except for rss1. Permeability in the less rough fractures (rss1-rss3) with smallest RMS share a common trend of increasing after a threshold shear displacement (~10 mm or more with higher RMS asperity heights) with the

permeability then reaching a plateau and stabilizing. However, for fractures with moderate RMS roughness (rss4), the fracture permeability evolves relatively unstably after the initial onset of permeability growth. Finally, for the roughest fractures (rss5 and rss6) permeability decreases following the attainment of peak permeability enhancement.

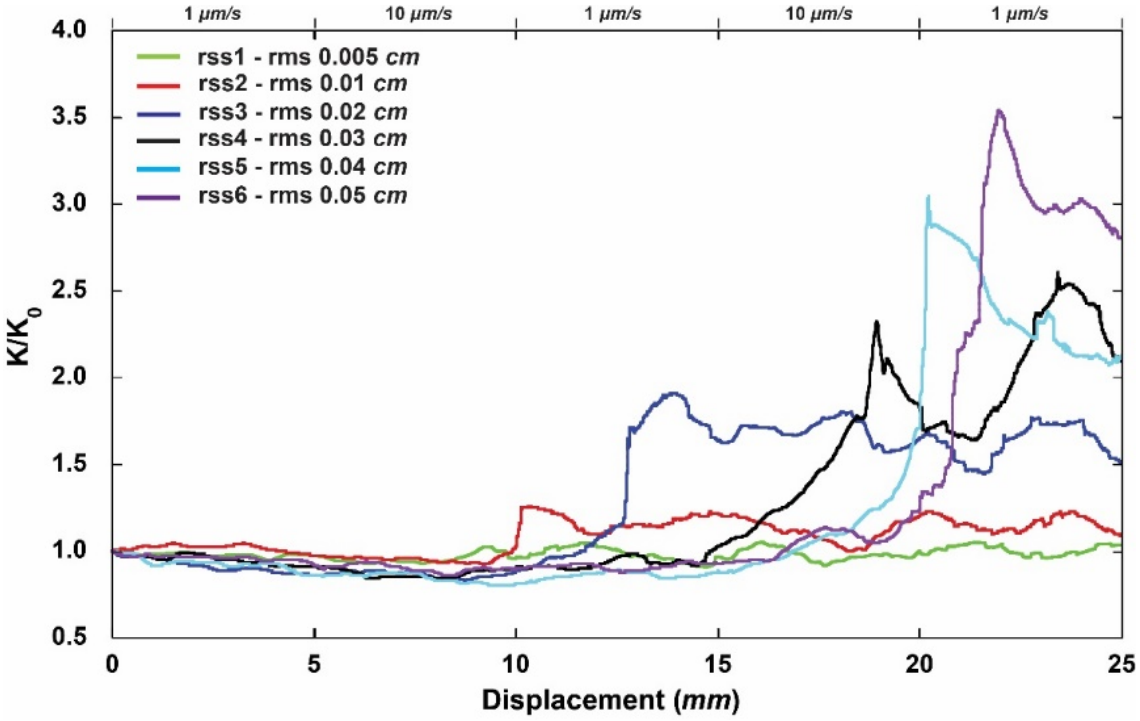

Figure 4-5. Evolution of fracture permeability (k/k_0) for tests rss1 through rss6. Fracture permeability is estimated from the evolution of local porosity measured along the fracture flow-path. Permeability decreases slightly in the first ~10 mm of shear displacement with compaction, except for rss1, and then increases rapidly until reaching a plateau (rss2-rss4). Permeability decreases post-peak permeability for the roughest fractures with highest RMS (rss5 and rss6).

3.3 Evolution of slip stability

The evolution of slip stability of the simulated rough fractures is important in understanding the characteristics of the potential for induced seismicity. Stability may be

indexed via the $(a-b)$ parameter. Positive values suggest aseismic behavior and negative values indicate potential seismic behavior. In this study, the $(a-b)$ values are extracted by fitting the rate and state friction law to the detrended friction evolution from the velocity steps. **Figure 4-6** shows the summarized $(a-b)$ values for samples rss1 through rss6 (a few extreme outliers are excluded that result from the interference of closely occurring stress drops). $(a-b)$ values generally scatter around the neutral (zero) line, showing mostly velocity neutral behavior. The $(a-b)$ values increase with RMS asperity height (from 0.005 cm to 0.05 cm).

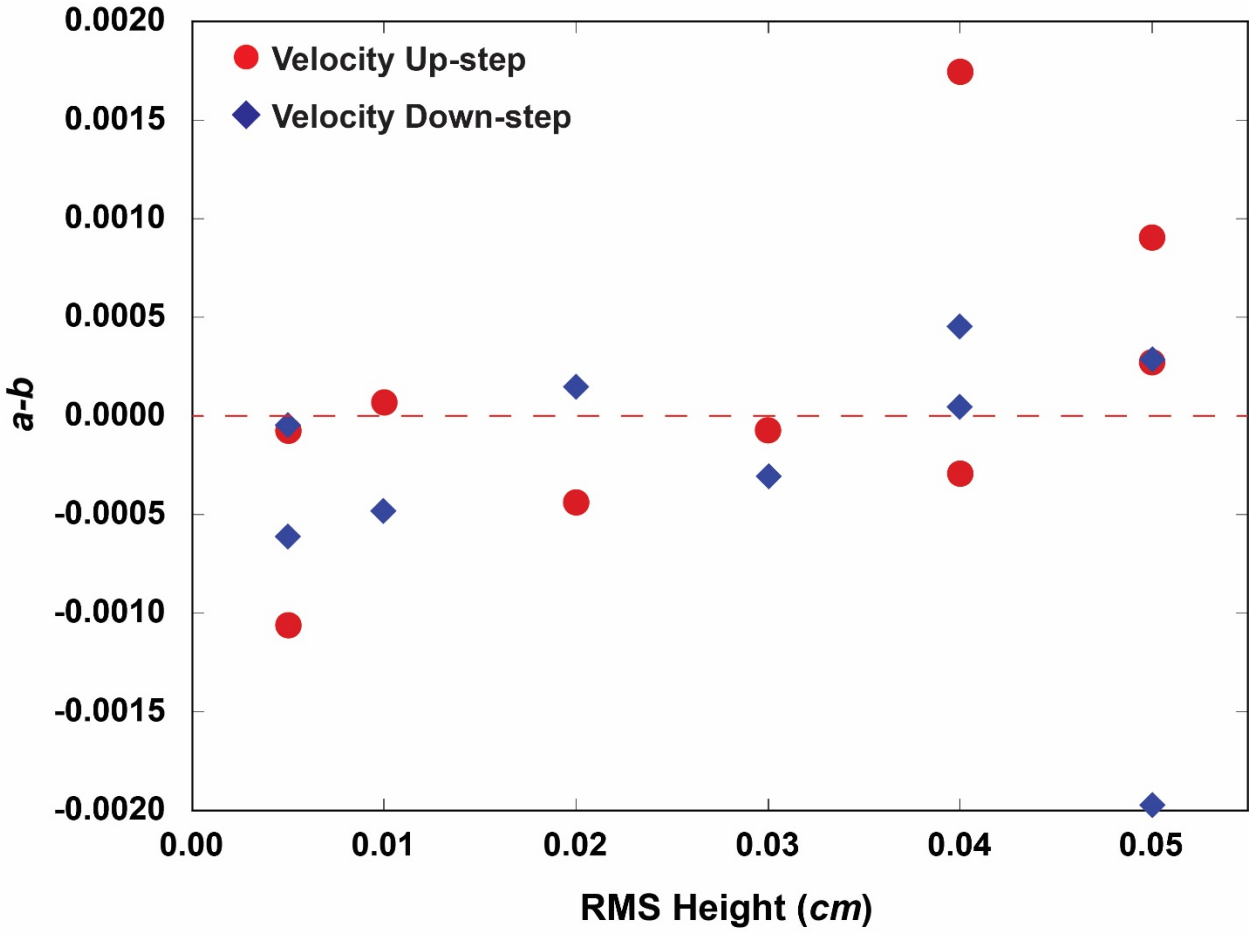

Figure 4-6. Summarized $(a-b)$ values for different RMS asperity heights (0.005cm to 0.05cm). The $(a-b)$ values generally scatter around the zero line, showing velocity neutral behavior.

$(a - b)$ values increase with RMS asperity height, implying a dominant effect of wear products generated by asperity comminution in rougher fractures.

4. Discussion

RMS asperity height is shown to play an important role in controlling the shear strength, slip stability, and permeability of the fracture. We observe that larger RMS asperity heights result in higher peak shear strengths and a larger threshold displacement for failure with a larger stress drop. A higher RMS asperity height also precipitates greater shear dilation, resulting in an increase in fracture permeability. However, extremely rough fractures exhibit net reduction in permeability post peak permeability. Natural fractures are complex systems with anisotropy in roughness and asperity strength. We provide a brief discussion of relative roles of asperity wavelength anisotropy, asperity strength, and finally a proposed mechanism for permeability evolution for rough fractures.

4.1 Influence of RMS height on peak frictional strength

We have shown that RMS asperity height is closely related to peak shear strength. **Figure 4-7** shows the relationship between peak shear strength, correlated threshold shear displacement and RMS asperity height (0.005 cm to 0.05 cm in this study) for a single wavelength. Peak shear strength increases near linearly with RMS asperity height. The threshold shear displacement for peak shear strength also increases with RMS asperity height following a similar trend except for RMS heights larger than 0.04 cm. When RMS

height reaches 0.05 cm, the threshold shear displacement only increases slightly. These observed trends suggest that the shear strength and shear displacement required to reach failure is linearly related to the RMS asperity height, up to a limiting asperity height (0.05 cm in this study). Thus the shear strength of rough fractures is not solely determined by asperity heights and wavelengths, but also by the strength of the asperities as well.

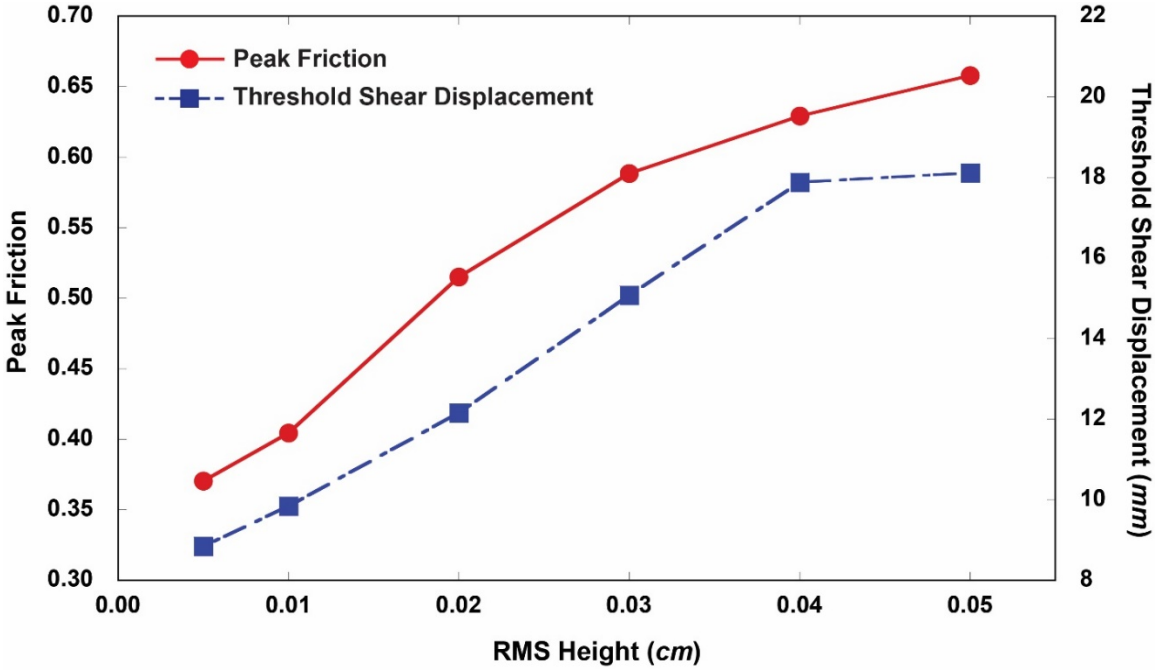

Figure 4-7. Peak shear strength and corresponding threshold shear displacement versus RMS asperity height (from 0.005 cm to 0.05 cm). These two properties are positively correlated to RMS asperity height up to a threshold RMS height (e.g. 0.04 cm).

4.2 Influence of roughness anisotropy

The anisotropy of the roughness within the plane of the fracture plays an important role in determining the mechanical and rheological properties. In this study, the anisotropy

of roughness is interpreted by varying asperity wavelength in the shear direction (x direction, rss7 through rss9), and perpendicular to the shear direction (y direction, rss10 through rss12). Fracture surfaces with various degree of roughness anisotropy (wavelength of 0.5 cm, 1 cm, 3 cm, and 5 cm in one direction) are tested. The fracture surface profiles are shown in **Figure 4-8**.

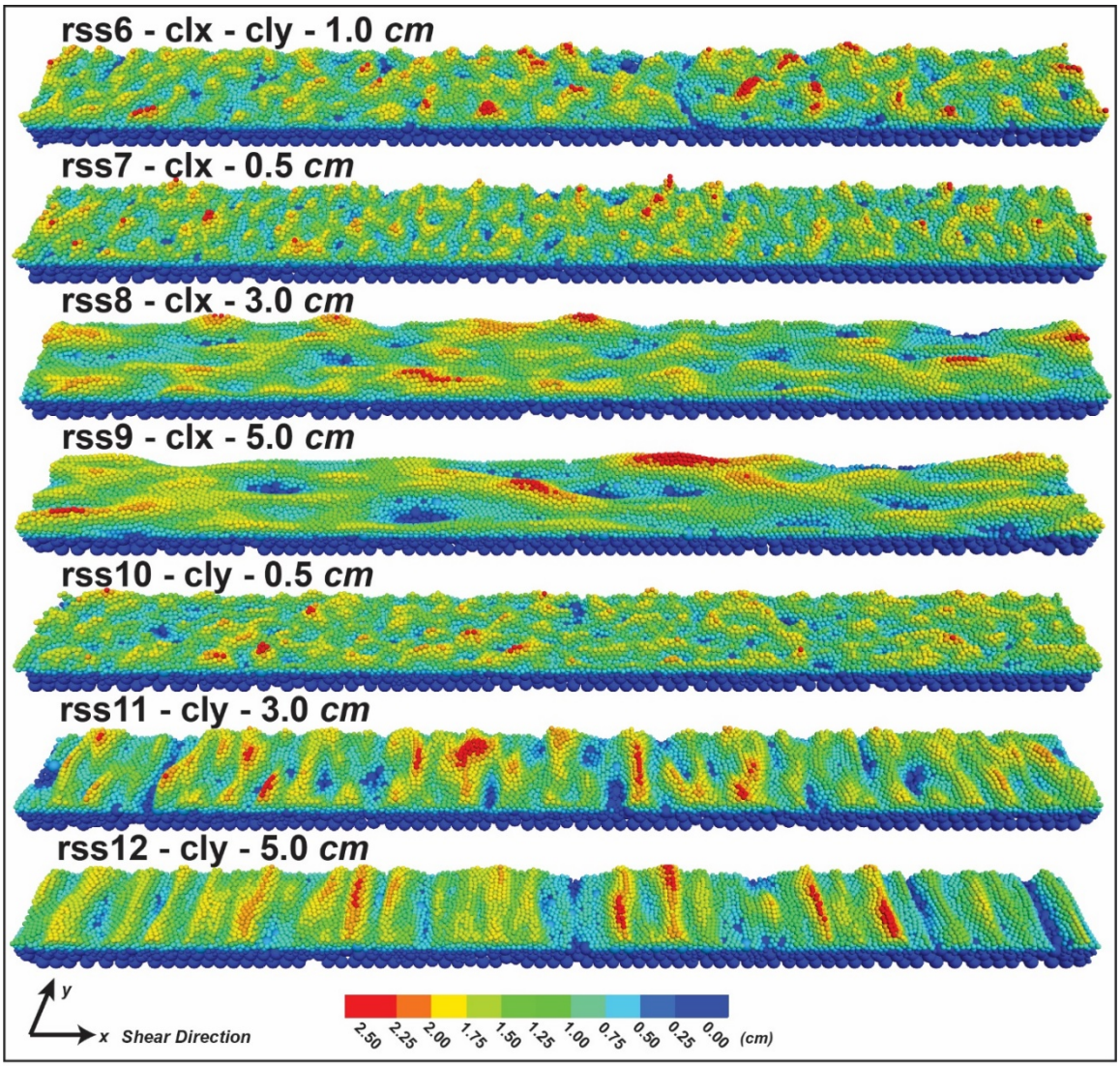

Figure 4-8. Fracture surface profiles for samples rss6 through rss12. Lower fracture surfaces before shear are shown. Specifically, rss6 features a uniform wavelength distribution in both x and y

directions; rss7, rss8, and rss9 feature increasing wavelengths in the x direction (shear direction); rss10, rss11, and rss12 feature increasing wavelength in y direction.

The evolution of shear strength, permeability, and stability parameters resulting from these profiles are shown in **Figure 4-9**. Increasing asperity wavelength in the shear direction reduces the peak strength and the amount of the stress drop at failure. Fractures with larger wavelengths in the shear direction (rss9) show permeability enhancement at a smaller threshold shear displacement. Sample rss9 also shows a stabilized permeability at near-peak levels without any tendency to decrease, while the permeability of rss6, rss7 and rss8 (fractures with smaller asperity wavelengths in the shear direction) slightly decrease after reaching peak permeability. In terms of stability parameters, **Figure 4-9**(b) shows a slight trend of increasing $(a - b)$ values with increasing wavelength in the shear direction.

Increasing asperity wavelength perpendicular to the shear direction（**Figure 4-9**(c)）reduces the peak shear strength, and the magnitude of stress drops at failure. Additionally, the stress drop evolves from a single or several abrupt drops at failure with large magnitude (rss6, rss10) to a series of smaller stress drops with a cyclic form (rss11, rss12). The residual shear strength increases with an increase in the asperity wavelength perpendicular to the shear direction. In terms of stability parameters, the values are broadly scattered with no obvious relationship between the values of $(a - b)$ and the asperity wavelength apparent.

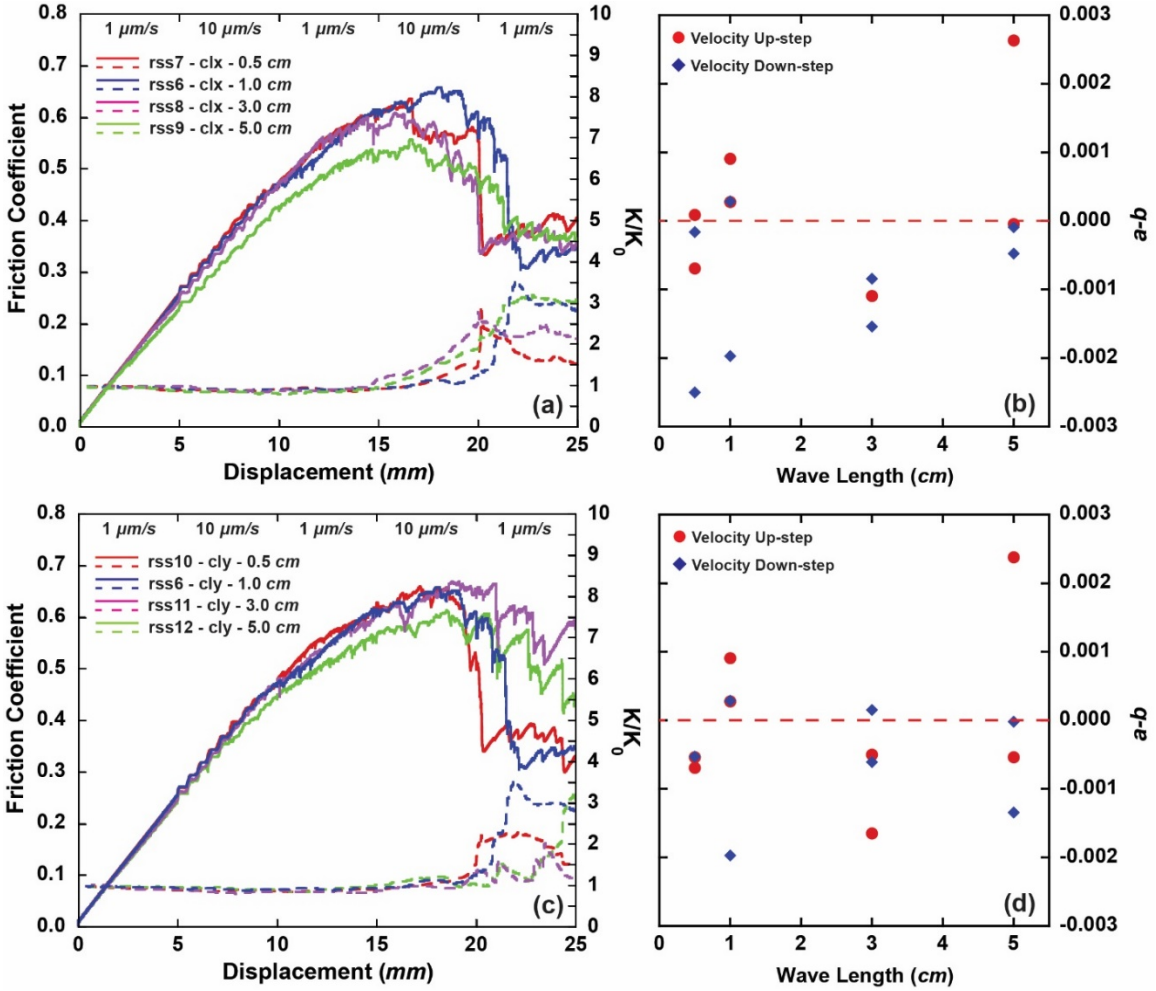

Figure 4-9. The evolution of shear strength, fracture permeability, and stability parameters related to the anisotropy of asperity wavelength, i.e. in the shear direction and perpendicular to the shear direction. (a) Shear strength and permeability evolution of fractures with asperity wavelengths of 0.5cm, 1.0cm, 3.0cm and 5.0 cm (rss6, rss7, rss8, and rss9) in the shear direction; (b) Stability parameters of samples rss6, rss7, rss8, and rss9; (c) Shear strength and permeability evolution of fractures with asperity wavelengths of 0.5cm, 1.0cm, 3.0cm and 5.0 cm (rss6, rss10, rss11, and rss12) perpendicular to the shear direction; (d) Stability parameters of samples rss6, rss10, rss11, and rss12. The left column shows the geometry of the lower fracture coupon before shear.

4.3 Influence of asperity strength

The strength of asperities plays an important role in determining the ensemble mechanical strength of fractures. In this study, we discuss the influence of asperity strength by varying the tensile strength and cohesion for the contacts while retaining all other parameters constant. **Figure 4-10** shows the evolution of shear strength, permeability, and stability of specimens featuring parallel bond strengths and cohesion of 20 MPa, 50 MPa, and 500 MPa (rss14, rss4, and rss13, respectively). The resulting evolution of shear strength (**Figure 4-10**) suggest that increasing tensile strength and cohesion results in an increase in peak shear strength. Specifically, rss13 shows ~25% higher peak shear strength than rss4 and ~50% higher than that of rss14, respectively. This trend can be explained by the rationale that lower bonding strength and cohesion results in weaker asperity strength. Therefore, specimens with lower bonding strength and cohesion are subject to increased localized failure and asperity breakage, producing more wear products during shear. This effect is shown by the amount of broken bonds inside the analog coupons as shown in **Figure 4-10** (the lower fracture coupons are shown with 95% transparent backgrounds). Noticeably, the bond breakage tends to localize on the contacting faces of the specimens where stress concentrates due to loading.

In terms of permeability evolution, increasing tensile strength and cohesion causes permeability enhancement to initiate both earlier and to a higher degree, as apparent in **Figure 4-10**(a). Interestingly, rss14 shows almost no enhancement of permeability throughout the simulation. This may be related to the localization of bond breakage on the two sides of the specimen and the deposition of comminution products between the fracture

faces. Shear-induced bond breakage produces relatively large amount of wear products, which plausibly clog the fluid passage in the fracture, reducing fracture permeability.

Additionally, as shown in **Figure 4-10**(b), the stability parameters are mostly negative and show an even broader range of variation with larger bonding strength and cohesion. However, the stability parameters do not show any significant correlation with increasing tensile strength and cohesion.

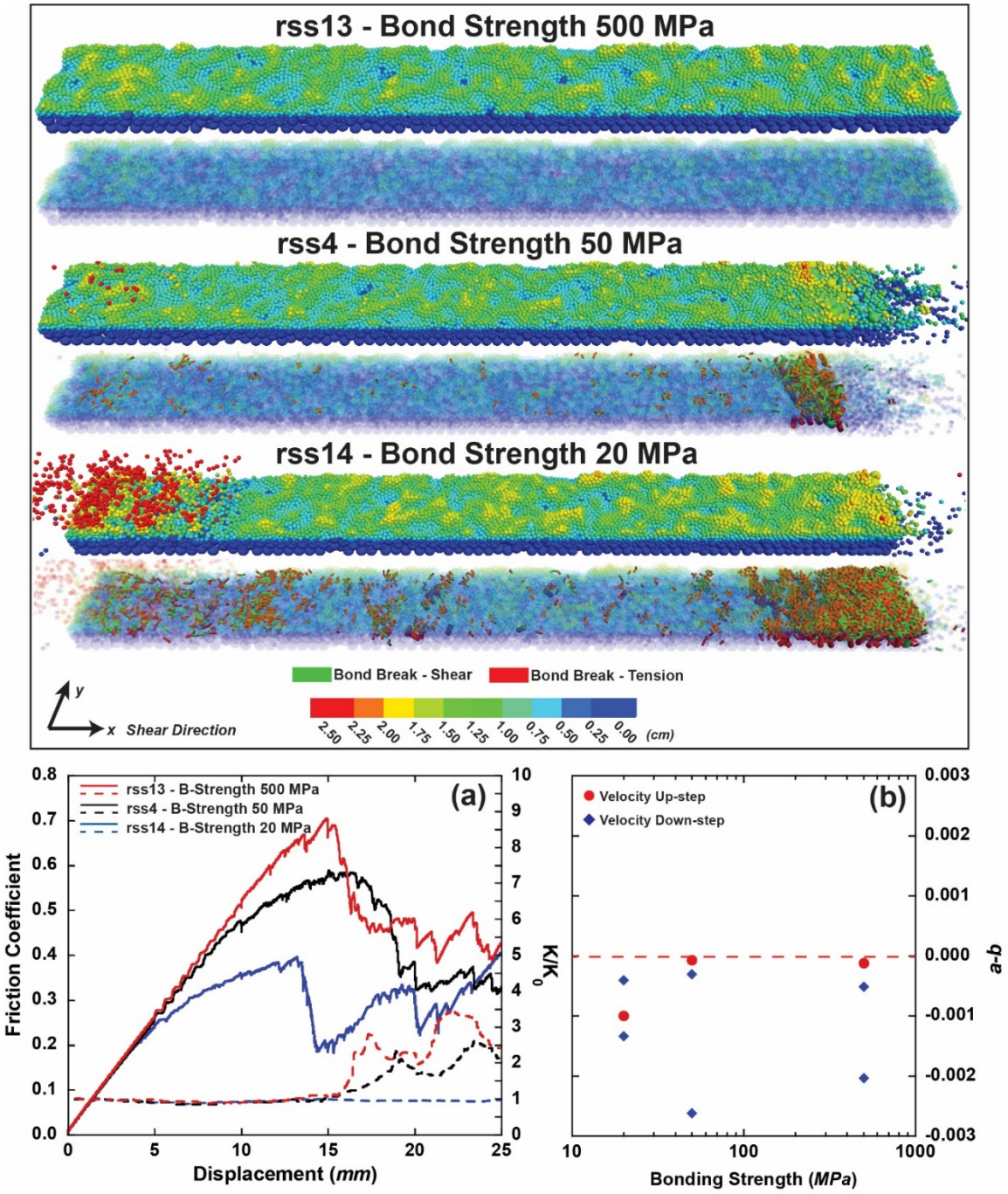

Figure 4-10. Fracture profiles, specimen geometries, and bonding breakage after 25 mm of shear displacement for samples rss4, rss13, and rss14. (a) Evolution of shear strength and permeability with bond strengths and cohesion of 20 MPa, 50 MPa, and 500 MPa, respectively; (b) Stability parameters plotted against bond strengths.

4.4 Influence of shear generated wear products

The generation of wear products during shear are commonly observed elsewhere (Faoro et al., 2009; Bakker et al., 2016; Fang et al., 2017; Fang et al., 2017) and also in this study. The generated wear products can be transported and redistributed by mechanical interaction between the two fracture surfaces, and by fluid, if present (Candela et al., 2014 & 2015). These wear products can influence the mechanical the rheological properties of the fracture through a variety of mechanisms. The wear products may both impact shear strength of the fracture by localizing shear and clog pores and major fluid pathways within the fracture, staunching permeability evolution. Over longer timescales, mechanical and fluid interactions and reaction between wear products and asperities may result in geochemical transformations that alter surface properties of the asperities and impact the evolution of rheological and transport properties. In this study, the generation of wear products for samples rss1 through rss6 are represented at red highlighted particles in **Figure 4-11**. The corresponding numbers of broken bonds are shown in the lower right plot in **Figure 4-11**.

It is typically observed that rough fractures with higher RMS asperity heights produce more wear products (rss6 vs. rss1 in **Figure 4-11**). However, samples rss1 and rss2 do not show a significant difference in the amount of generated wear products. While rss3 and rss4 show a large increase in the amount of generated wear products, this increase slows down in rss5 and rss6. Noticeably, the threshold shear displacement for bond breakage (left plot of **Figure 4-11**), where the slope of the evolution curve becomes abruptly smaller, corresponds with the major stress drop at failure (**Figure 4-3**), and the

peak in permeability evolution (**Figure 4-5**). This behavior indicates dominant influence of wear products on the evolving shear strength and permeability of the fracture, as indicated by similar residual shear strengths for samples rss1 through rss6. Large initial asperity height results in increased dilation and peak permeability, but generates more wear products, reducing permeability by clogging major fluid channels. Therefore, permeability evolution is potentially dependent on the competitive influence of asperity height (contributing to dilation) and the volume of generated wear products (contributing to clogging) - with the dominant process defining the response. When the clogging effect exceeds that of dilation, the permeability of the fracture may be reduced after reaching its peak, even though the fracture begins with higher RMS asperity heights. This mechanism is suggested by the permeability evolution of samples rss5 and rss6 (**Figure 4-5**) and the amount of generated wear products (**Figure 4-11**). It is worth noting that the wear products mainly concentrate on the principal contacting portions of the fractures, suggesting that stress concentration (in the laboratory and otherwise) may result in the clustering of wear products at kinks in fractures and fault asperities.

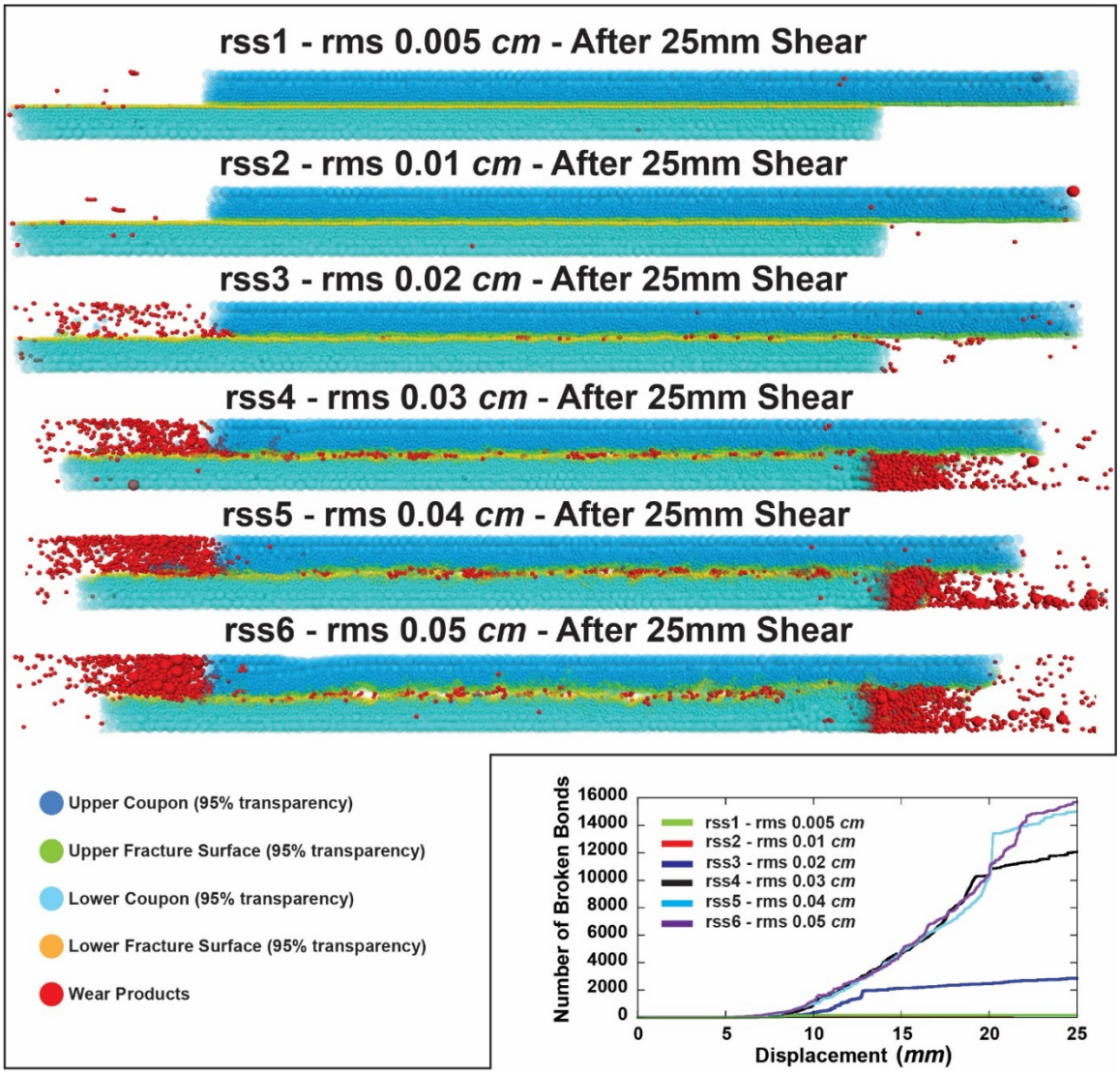

Figure 4-11. Fracture profiles and geometries of the fracture specimens (95% transparency) after 25 mm of shear displacement for samples rss1 through rss6. Shear generated wear products are highlighted by red particles. Lower right plot shows the evolution of numbers of broken bonds during shear simulation for specimens with various RMS asperity heights (rss1 through rss6).

5. Conclusions

In this study, we investigate the influence of fracture roughness on the shear strength, slip stability, and permeability evolution of fractures by discrete element method modeling. The rough fracture surfaces are generated based on RMS asperity heights and asperity wavelengths. We have discussed the influence of fracture roughness by the following aspects: RMS asperity heights, anisotropy of asperity wavelength, strength of asperities. Also, we have analyzed the stability parameters, the relationship between peak shear strength and RMS asperity heights, and proposed mechanisms for the permeability evolution for rough fractures. We summarize the conclusions of this study as following:

1. Larger RMS asperity height yields higher peak shear strength, while requiring more shear displacement to reach the peak strength. The relationship between asperity height and peak shear strength is positively correlated, but in a non-linear fashion, i.e., under given asperity strength, there is a limit for peak shear strength for rough fractures with increasing RMS asperity heights.
2. Increasing the RMS asperity height can alter slip stability of rough fractures from mostly velocity weakening to velocity strengthening. This transformation of slip stability can be related to the generation of wear products and its domination effect.
3. Anisotropy of asperity wavelength can influence the shear strength and permeability evolution of rough fractures. Larger asperity wavelength in the shear direction reduces peak shear strength of the fracture while increase the fracture permeability. Larger asperity wavelength perpendicular to the shear direction can

slight reduce peak shear strength, induce more frequent stress drops during failure, while delaying or suppress the permeability enhancement.

4. The strength of the asperities (bonding strength and cohesion) are crucial in determine the shear strength and permeability evolution of the rough fractures. Lower asperity strength results in lower shear strength and less permeability enhancement.
5. The amount, distribution, and transport of shear generated wear products can dominate the evolution of shear strength, slip stability, and permeability of rough fractures by localization and clogging effects. Fractures with more wear products exhibits lower shear strength, higher slip stability, and lower permeability during dynamic shear.

Conclusions drawn above are specifically applicable to the parameters and situations in this study with the potential of upscaling to the field. Future study may consider the deformation and crushing of individual analog particles. Nonetheless, our study provides a straightforward way to study the influence of surface roughness on the mechanical and rheological properties of fractures.

References

Abe, S., Dieterich, J. H., Mora, P., and Place, D. (2002). Simulation of the influence of rate- and state-dependent friction on the macroscopic behavior of complex fault zones with the lattice solid model. *Pure and Applied Geophysics*, *159*(9), 1967–1983. https://doi.org/10.1007/s00024-002-8718-7

Ai, J., Chen, J. F., Rotter, J. M., and Ooi, J. Y. (2011). Assessment of rolling resistance models in discrete element simulations. *Powder Technology*, *206*(3), 269–282. https://doi.org/10.1016/j.powtec.2010.09.030

Antonellini, M. A., and Pollard, D. D. (1995). Distinct element modeling of deformation bands in sandstone. *Journal of Structural Geology*, *17*(8), 1165–1182. https://doi.org/10.1016/0191-8141(95)00001-T

Asadi, M. S., Rasouli, V., and Barla, G. (2013). A laboratory shear cell used for simulation of shear strength and asperity degradation of rough rock fractures. *Rock Mechanics and Rock Engineering*, *46*(4), 683–699. https://doi.org/10.1007/s00603-012-0322-2

Bakker, E., Hangx, S. J. T., Niemeijer, A. R., and Spiers, C. J. (2016). Frictional behaviour and transport properties of simulated fault gouges derived from a natural CO2 reservoir. *International Journal of Greenhouse Gas Control*, *54*, 70–83. https://doi.org/10.1016/j.ijggc.2016.08.029

Barton, N. (1973). Review of a new shear-strength criterion for rock joints. *Engineering Geology*, *7*(4), 287–332. https://doi.org/10.1016/0013-7952(73)90013-6

Barton, N., and Choubey, V. (1977). The shear strength of rock joints in theory and practice. *Rock Mechanics*, *10*(1–2), 1–54. https://doi.org/https://doi.org/10.1007/BF01261801

Barton, N., Bandis, S., and Bakhtar, K. (1985). Strength, deformation and conductivity coupling of rock joints. *International Journal of Rock Mechanics and Mining Sciences And*, *22*(3), 121–140. https://doi.org/10.1016/0148-9062(85)93227-9

Brown, S. R. (1995). Simple mathematical model of a rough fracture. *Journal of Geophysical Research: Solid Earth*, *100*(B4), 5941–5952. https://doi.org/10.1016/B978-1-85617-497-8.50019-2

Brown, S. R., and Scholz, C. H. (1985). Broad bandwidth study of the topography of natural rock surfaces. *Journal of Geophysical Research*, *90*(B14), 12575. https://doi.org/10.1029/JB090iB14p12575

Burbidge, D. R., and Braun, J. (2002). Numerical models of the evolution of accretionary wedges and fold-and-thrust belts using the distinct-element method. *Geophysical Journal International*, *148*(3), 542–561. https://doi.org/10.1046/j.1365-246x.2002.01579.x

Cundall, P. A. (2000). Numerical experiments on rough joints in shear using a bonded particle model. In L. F.K. and U. J.L. (Eds.), *Aspects of Tectonic Faulting* (pp. 18–26). Springer, Berlin, Heidelberg. https://doi.org/https://doi.org/10.1007/978-3-642-59617-9_1

Cundall, P. A., and Strack, O. D. L. (1979a). A discrete numerical model for granular assemblies. *Géotechnique*, *29*(1), 47–65. https://doi.org/10.1680/geot.1979.29.1.47

Cundall, P. A., and Strack, O. D. L. (1979b). A discrete numerical model for granular assemblies. *Géotechnique*. https://doi.org/10.1680/geot.1979.29.1.47

Dieterich, J. H. (1978). Time-dependent friction and the mechanics of stick-slip. *Pure and Applied Geophysics PAGEOPH*, *116*(4–5), 790–806. https://doi.org/10.1007/BF00876539

Ellsworth, W. L. (2013). Injection-induced earthquakes. *Science*, *341*(6142), 1–8. https://doi.org/10.1126/science.1225942

Elsworth, D., and Goodman, R. E. (1986). Characterization of rock fissure hydraulic conductivity using idealized wall roughness profiles. *International Journal of Rock Mechanics and Mining Sciences And*, *23*(3), 233–243. https://doi.org/10.1016/0148-9062(86)90969-1

Elsworth, D., Spiers, C. J., and Niemeijer, A. R. (2016). Understanding induced seismicity. *Science*, *354*(6318), 1380–1381. https://doi.org/10.1126/science.aal2584

Fang, Y., Wang, C., Elsworth, D., and Ishibashi, T. (2016). Friction-permeability relationships for reservoir caprocks. *50th US Rock Mechanics / Geomechanics Symposium 2016*, *3*.

Fang, Y., Elsworth, D., Wang, C., Ishibashi, T., and Fitts, J. P. (2017). Frictional stability-permeability relationships for fractures in shales. *Journal of Geophysical Research: Solid Earth*, *122*(3), 1760–1776. https://doi.org/10.1002/2016JB013435

Fang, Y., Wang, C., Elsworth, D., and Ishibashi, T. (2017). Seismicity-permeability coupling in the behavior of gas shales, CO2 storage and deep geothermal energy. *Geomechanics and Geophysics for Geo-Energy and Geo-Resources*, *3*(2), 189–198. https://doi.org/10.1007/s40948-017-0051-9

Guo, Y., and Morgan, J. K. (2004). Influence of normal stress and grain shape on granular friction: Results of discrete element simulations. *Journal of Geophysical Research B: Solid Earth*, *109*(12), 1–16. https://doi.org/10.1029/2004JB003044

Iwashita, K., and Oda, M. (1998). Rolling Resistance at Contacts in Simulation of Shear Band Development by DEM. *Journal of Engineering Mechanics*, *124*(3), 285–292. https://doi.org/10.1061/(ASCE)0733-9399(1998)124:3(285)

Jiang, M., Shen, Z., and Wang, J. (2015). A novel three-dimensional contact model for granulates incorporating rolling and twisting resistances. *Computers and Geotechnics*, *65*, 147–163. https://doi.org/10.1016/j.compgeo.2014.12.011

Morgan, J. K. (1999). Numerical simulations of granular shear zones using the distinct element method: 2. Effects of particle size distribution and interparticle friction on mechanical behavior. *Journal of Geophysical Research*, *104*(B2), 2721. https://doi.org/10.1029/1998JB900055

Morgan, J. K. (2004). Particle dynamics simulations of rate- and state-dependent frictional sliding of granular fault gouge. *Pure and Applied Geophysics*, *161*(9–10), 1877–1891. https://doi.org/10.1007/s00024-004-2537-y

Morgan, J. K., and Boettcher, M. S. (1999). Numerical simulations of granular shear zones using the distinct element method: shear zone kinematics and the micromechanics of localization. *Journal of Geophysical Research*. Retrieved from http://onlinelibrary.wiley.com/doi/10.1029/1998JB900056/full

Ouyang, Z., and Elsworth, D. (1993). Evaluation of groundwater flow into mined panels. *International Journal of Rock Mechanics and Mining Sciences And*, *30*(2), 71–79. https://doi.org/10.1016/0148-9062(93)90701-E

Park, J. W., and Song, J. J. (2009). Numerical simulation of a direct shear test on a rock joint using a bonded-particle model. *International Journal of Rock Mechanics and Mining Sciences*, *46*(8), 1315–1328. https://doi.org/10.1016/j.ijrmms.2009.03.007

Potyondy, D. O. (2011). Parallel-Bond Refinements to Match Macroproperties of Hard Rock. *2nd FLAC/DEM Symposium*, (February), 14–16.

Potyondy, D. O., and Cundall, P. A. (2004). A bonded-particle model for rock. *International Journal of Rock Mechanics and Mining Sciences*, *41*(8 SPEC.ISS.), 1329–1364. https://doi.org/10.1016/j.ijrmms.2004.09.011

Ruina, A. (1983). Slip instability and state variable friction laws. *Journal of Geophysical Research: Solid Earth*. https://doi.org/10.1029/JB088iB12p10359

Samuelson, J., Elsworth, D., and Marone, C. (2011). Influence of dilatancy on the frictional constitutive behavior of a saturated fault zone under a variety of drainage conditions. *Journal of Geophysical Research: Solid Earth*, *116*(10), 1–17. https://doi.org/10.1029/2011JB008556

Segall, P., and Rice, J. R. (1995). Dilatancy, compaction, and slip instability of a fluid-infiltrated fault. *Journal of Geophysical Research: Solid Earth*, *100*(B11), 22155–22171. https://doi.org/10.1029/95JB02403

Sun, Z., Espinoza, D. N., and Balhoff, M. T. (2016). Discrete element modeling of indentation tests to investigate mechanisms of CO2-related chemomechanical rock alteration. *Journal of Geophysical Research: Solid Earth*, *121*(11), 7867–7881. https://doi.org/10.1002/2016JB013554

Walsh, F. R., and Zoback, M. D. (2015). Oklahoma's recent earthquakes and saltwater disposal. *Science Advances*, *1*(5), e1500195–e1500195. https://doi.org/10.1126/sciadv.1500195

Wang, C., Elsworth, D., and Fang, Y. (2017a). Influence of weakening minerals on ensemble strength and slip stability of faults. *Journal of Geophysical Research: Solid Earth*, *122*(9), 7090–7110. https://doi.org/10.1002/2016JB013687

Wang, C., Elsworth, D., and Fang, Y. (2017b). Influence of weakening minerals on ensemble strength and slip stability of faults. *Journal of Geophysical Research: Solid Earth*, *122*(9), 7090–7110. https://doi.org/10.1002/2016JB013687

Wang, C., Elsworth, D., Fang, Y., Liu, K., and Jia, Y. (2017). Weakening effects of microstructural tribological films in CO2-altered reservoirs and caprocks. *American Rock Mechanics Association*, 8.

Zoback, M. D., and Gorelick, S. M. (2012). Earthquake triggering and large-scale geologic storage of carbon dioxide. *Proceedings of the National Academy of Sciences*, *109*(26), 10164–10168. https://doi.org/10.1073/pnas.1202473109

Chapter 5

Conclusions

Our studies investigate the mineralogical and textural control on the shear strength, slip stability, and permeability of faults and fractures. Specifically, we develop two-dimensional (2D) and three-dimensional (3D) discrete element models (DEM) to explore the influence of frictionally weak minerals on the ensemble frictional and rheological behavior of faults. Moreover, we elaborate the influence of CO_2-transformed grain coatings on the bulk shear strength, frictional stability, and permeability of quartz rich faults using a novice mini double direct shear apparatus. Lastly, we conduct numerical shear tests on mated fractures with controlled roughness (asperity heights and wavelength) to investigate its influence on frictional and permeability responses upon reactivation events. Here we repeat, verbatim, the conclusions form our studies.

In **Chapter 1**, we established a DEM model to simulate the mechanical responses of synthetic gouge mixtures consisting of a quartz and talc analogs. Direct shear experiments with pre-defined velocity up-steps and down-steps were conducted on both uniform and textured mixtures. This is achieved by altering the weight percentage of talc in uniform mixtures and the relative thickness of the talc layer in textured (layered) mixtures, and in then analyzing experimental results. The following conclusions are drawn:

1. Talc has a significant weakening effect on the shear strength of quartz-rich fault gouges. This effect is enhanced when talc forms a through-going layer in the gouge.

2. Relatively small amounts of talc (10% to 25% talc in the uniform mixtures or 3-particles to 5-particles in the textured mixtures) can transform the stability behavior of the gouge from velocity-weakening to velocity strengthening.
3. Minerals with high elastic modulus and frictional resistance at contacts tend to dilate universally upon slip, while minerals with low elastic modulus and frictional resistance dilate during velocity up-steps but compact quickly during velocity down-steps.
4. Quartz tends to be dilation dominant and thus an increase in permeability could be expected in quartz-rich faults during slip events; while talc also dilates, but compacts much faster, therefore a decrease in permeability could be expected in talc-bearing faults.

The numerical modeling-derived conclusions suggests that DEM modeling is capable of simulating the shear strength and stability evolution of granular fault gouge using a simplified rate-state friction law. Also, it is possible to simulate gouge with complex mineralogical composition and with varying degrees and forms of heterogeneity. The analysis of coordination number and porosity evolution suggest new methods to examine the nature of permeability evolution of faults during the seismic cycle.

In **Chapter 2**, we explore the shear strength, slip stability, and permeability of analog quartz and talc mixtures *via* 3D discrete element modeling. Specifically, configurations of both uniform and layered mixtures with various talc: quartz weight proportions are examined. We perform numerical direct shear tests with velocity stepping

on the sample mixtures and capture the evolution of shear strength, slip stability, and permeability. We conclude the following based on the observed results:

1. Simulations show strong weakening effects in uniform mixtures of talc; a linear weakening effect is observed due to the limitation of particle shape - in this case restricted to spherical. A dominant weakening effect is observed for layered talc. A mixture with ~8% talc can induce an ~50% reduction in shear strength.
2. Increased talc content can enhance the stability of uniform mixtures by increasing $(a - b)$ values, however, increasing talc layer thickness in layered mixtures shows no apparent influence on the stability behavior.
3. In uniform mixtures, permeability increases in the shear localization zone with more quartz present, while decreases with more talc. Permeability evolves to a steady state, and is enhanced with velocity up-steps while suppressed with down-steps after the maturation of shear localization.
4. Dimensionality can greatly impact the resolution of the dynamic response of gouge mixtures during shear. The friction evolution during a velocity change can be clearly observed in 3D simulations which are largely obscured in 2D models.

The results fit previous laboratory observations while some slight mismatches are also noticed. These inaccuracies can be related to the idealized particle shape and size distribution, simplified to spherical in these mixtures. Future research of full implementation of realistic particle shape and deformable grains need to be achieved to better simulated the behavior of faults during shear. Nonetheless, our work shows an alternative way of exploring the rheological properties of faults during dynamic shear.

In **Chapter 3**, we report observations and analysis of the influence of hematite and goethite coatings on the shear strength, slip stability, and permeability evolution of quartz. The hematite- and goethite-coated quartz samples are synthesized in the laboratory as analog pristine and CO_2-transformed fault gouge. A novel double direct shear (DDS) apparatus has been implemented in the simple-triaxial pressure vessel to conduct shear-permeability tests on the coated samples. The response of the coated quartz samples before, during and following shear experiments suggest:

1. Both hematite- and goethite- coated quartz show higher peak shear strength than un-coated quartz; goethite-coated quartz is slightly weaker than hematite-coated quartz in peak shear strength.
2. Goethite-coated quartz show velocity-strengthening behavior while featuring a higher frictional healing rate, creep rate, and permeability. This suggests a reduced risk of seismic reactivation but greater loss of inventory in the long-term containment of CO_2.
3. Hematite coatings show weaker attachment to host quartz grains than goethite coatings and feature a high degree of mobility and self-clustering upon fluid interaction.
4. Wear products are generated during mechanical shear. The transport of these wear products can clog fluid conduits during shearing, thus significantly reducing permeability parallel to the shear direction.

This study provides insights into how hematite and goethite coatings, before and after long-term geochemical alteration by CO_2, can influence shear strength, stability, and

permeability evolution of faults during shearing. Future experiments, potentially long-term shear-permeability tests, on natural samples are necessary to strengthen these conclusions.

In **Chapter 4**, we investigate the influence of fracture roughness on the shear strength, slip stability, and permeability evolution of fractures by discrete element method modeling. The rough fracture surfaces are generated based on RMS asperity heights and asperity wavelengths. We have discussed the influence of fracture roughness by the following aspects: RMS asperity heights, anisotropy of asperity wavelength, strength of asperities. Also, we have analyzed the stability parameters, the relationship between peak shear strength and RMS asperity heights, and proposed mechanisms for the permeability evolution for rough fractures. We summarize the conclusions of this study as following:

1. Larger RMS asperity height yields higher peak shear strength, while requiring more shear displacement to reach the peak strength. The relationship between asperity height and peak shear strength is positively correlated, but in a non-linear fashion, i.e., under given asperity strength, there is a limit for peak shear strength for rough fractures with increasing RMS asperity heights.
2. Increasing the RMS asperity height can alter slip stability of rough fractures from mostly velocity weakening to velocity strengthening. This transformation of slip stability can be related to the generation of wear products and its domination effect.
3. Anisotropy of asperity wavelength can influence the shear strength and permeability evolution of rough fractures. Larger asperity wavelength in the shear direction reduces peak shear strength of the fracture while increase the fracture permeability. Larger asperity wavelength perpendicular to the shear direction can

slight reduce peak shear strength, induce more frequent stress drops during failure, while delaying or suppress the permeability enhancement.

4. The strength of the asperities (bonding strength and cohesion) are crucial in determine the shear strength and permeability evolution of the rough fractures. Lower asperity strength results in lower shear strength and less permeability enhancement.
5. The amount, distribution, and transport of shear generated wear products can dominate the evolution of shear strength, slip stability, and permeability of rough fractures by localization and clogging effects. Fractures with more wear products exhibits lower shear strength, higher slip stability, and lower permeability during dynamic shear.

Conclusions drawn above are specifically applicable to the parameters and situations in this study with the potential of upscaling to the field. Future study may consider the deformation and crushing of individual analog particles. Nonetheless, our study provides a straightforward way to study the influence of surface roughness on the mechanical and rheological properties of fractures.

VITA

Chaoyi Wang

EDUCATION

The Pennsylvania State University

- Ph.D. (Candidate) in Energy and Mineral Engineering 2015 - 2018
- M.S. in Civil and Environmental Engineering 2012 - 2015

Tongji University

- B.S. in Civil Engineering 2008 - 2012

RESEARCH EXPERIENCES

Research Assistant, The Pennsylvania State University

- Experimental Rock Mechanics 2015 - 2018
- Digital Rock Modeling

Research Assistant, The Pennsylvania State University

- Field Geotechnical Testing 2012 - 2015
- Experimental Soil Mechanics

JOURNAL PUBLICATIONS

- **Wang, C.**, Qiu, T., Xiao, M., & Wang, J. (2017). Utility Trench Backfill Compaction Using Vibratory Plate Compactor versus Excavator-Mounted Hydraulic Plate Compactor. *Journal of Pipeline Systems Engineering and Practice*, *8*(4), 04017021. https://doi.org/10.1061/(ASCE)PS.1949-1204.0000284
- **Wang, C.**, Elsworth, D., and Fang, Y. (2017). Influence of weakening minerals on ensemble strength and slip stability of faults. *Journal of Geophysical Research: Solid Earth*, 122(9), 7090–7110. https://doi.org/10.1002/2016JB013687
- **Wang, C.**, Elsworth, D., and Fang, Y. (2019). Ensemble Shear Strength, Stability, and Permeability of Mixed Mineralogy Fault Gouge Recovered from 3D Granular Models. *Journal of Geophysical Research: Solid Earth*, 124(1), 425-441. https://doi.org/10.1029/2018JB016066
- **Wang, C.**, and Elsworth, D. (2018). The Influence of CO2-transformed Iron Oxide Grain Coatings on the Rheological and Transport Behaviors of Faults. *Scientific Reports, submitted*
- **Wang, C.**, Elsworth, D., Fang, Y., and Zhang, F. (2018). Influence of Fracture Roughness on Shear Strength, Slip Stability and Permeability: A Micro Mechanistic Analysis by 3D Digital Rock Physics. *Journal of Rock Mechanics and Geotechnical Engineering, Submitted*